Numerical Simulations of Magnetic Dynamics in Nanoparticles

Jakob Garde

March 11, 2008

Preface

The writing of this thesis has been a long but rewarding process. First of all I have learned that things do take a long time. Second the process has given me valuable insight into the everyday work of scientists. Being part of the writing of scientific papers has been a privilege and lots of fun.

Many thanks to my supervisors Kim Lefmann and Per Hedegård who have aided me in their respective fields. Kims experimental insight into nanoparticle dynamics and his vision guided me through the writing. His approach, enthusiasm and optimism is a true inspiration. Per has aided the theoretical development and in particular I owe him a great thank in guiding me through the probability current calculations. Per always uses physical arguments that make sense, which I appreciate. I thank both for long discussions from which I have learned much. Thanks to Luise T. Kuhn for all the general advise and showing how to do the fits, to Per-Anker Lindgård for continuously asking questions which forced me into confronting every detail of the spinwave calculations and to Peter Willendrup for aiding me in MATLAB and Mfit related issues, which are numerous.

Thanks to my mother Maria for moral support and to my father Adam for a geologists perspective and making me stop going into more detail. Thanks to my brothers Thomas (for the coffee) and Daniel (for the company) and to Lars for inspiring me to work a lot. Thanks to Ea for being there. Thanks to my dog Dolpo for always wanting to chase cats and chicken in the garden.

It is indeed tempting to continue simulations and cover more ground. I believe the prospects of further investigations are practically endless. However, simulations take time and it has to end somewhere. Enjoy your reading!

Abstract

Recent neutron scattering studies of 8 nm hematite nanoparticles have shown an unexplained temperature dependency of the collective spin dynamics. This dynamics consists of precession modes and superparamagnetism of the classical antiferromagnetic submagnetization system, and is separated from the remaining magnetism due to size quantization of spin waves. The equation of motion describes the motion of these moments in the fields of the exchange interaction, and planar and axial crystal anisotropies. This thesis explores the collective dynamics by finding numerical solutions to the Langevin equation that emerges by coupling to a generic heat bath.

Simulation results are in quantitative agreement with scattering data. Furthermore, physically realistic histories of the submagnetization motion are visualized and used to interpret experimental results. At higher temperatures, random walk excites an angling between the submagnetizations. This leads to planar precessions due to the resulting torque of the exchange interaction.

Contents

Chapter 1

Introduction

Recent inelastic neutron scattering experiments of 8 nm hematite nanoparticles show that these behave differently from larger particles. Another sample of about 15 nm has earlier been investigated similarly, and understood. Size quantization of spin waves in both samples is strong enough to isolate the collective dynamics from the remaining magnetism. The collective dynamics is thus dominant and the most important. The combined spins of each antiferromagnetic sublattice are described by their magnetic moments, which allow for a classical description of the collective dynamics. Although all terms in the equation of motion are due to quantum effects, these can be reduced to a classical form.

The collective dynamics is investigated using a numerical implementation of Langevin dynamics, which is a statistical approach to describing interactions with a heat bath.

Without going into further detail, I will now outline the content of the chapters:

Chapter 2 concerns background information on specialized topics that the reader is not expected to be familiar with. I will explain nesseccary material about antiferromagnetism, magnetic dynamics in nanoparticles and neutron scattering. Beyond chapter 2, I will spend little time on background

information, and it is assumed that the reader has a basic understanding of solid state physics and magnetism.

In chapter 3 I will derive equations that model the uniform modes in antiferromagnetic nanoparticles with planar and axial anisotropies. Basic magnetic excitations to the Heisenberg Hamiltonian are considered. Then a classical equation of motion for the submagnetizations is derived. Finally the effect of temperature is introduced into the model using the phenomenological method of Langevin dynamics. If this section seems a bit excessive, the reader should trust that the theory is no less obscure in the literature.

Chapter 4 describes and validates the numerical method. It contains descriptions of how the theory was implemented, and compares basic simulations to simple, known cases.

In chapter 5 I will visualize and observer simulation results, and compare to experiment. Unexplained results are discussed in chapter 6, in which I give an interpretation of the higher temperature dynamics.

The summary and conclusion is found in chapter 7.

The appendices contain a proof of the formula that relates simulation to experiment, the relevant MATLAB simulation code, a theory paper on collective spinwaves in nanoparticles and addition simulation time evolution plots for the curious reader.

Chapter 2

Background

The main reference of this chapter is the book "Canted Antiferromagnetism: Hematite" by Morrish [1]. Specialized information about hematite nanoparticles is referenced explicitly. General texts on magnetism and solid state physics is found in the excellent books by Kittel [2] and Blundell [3]. See Yosida [4] for a more mathematical description.

2.1 Magnetism in Hematite

Many oxides and compounds of magnetic elements such as Ni, Fe, Co are insulating crystals that permit long-range ordering of the valence electron spins. Some are antiferromagnets, others ferro- or ferrimagnetic, and a few feature more exotic ordered ground states. Hematite, the mineral $\alpha-Fe_2O_3$, is such an magnetic iron oxide. It is used as iron ore and is very common in nature, even on the surface on Mars. Hematite with a high water content is known as rust. However, the most interesting feature is its magnetism – hematite is an antiferromagnet. Each Fe(III) ion harbours a total spin angular momentum of $s = \frac{5}{2}$ which is the aligned spins of the $3d^5$ valence electrons.

The crystal structure of $\alpha-Fe_2O_3$ is described by the hexagonal-trigonal

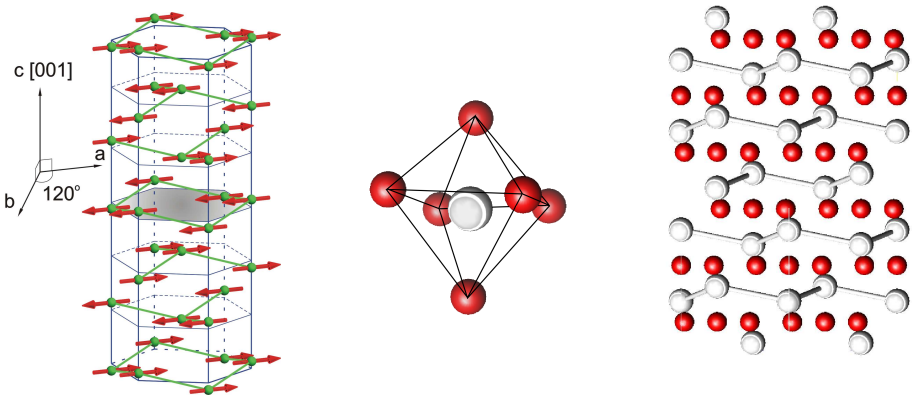

(a) *The antiferromagnetic Néel ground state. The arrows symbolize the spins of unpaired valence electrons. By Bente Lebech.*

(b) *Local near-octahedral environment of an Fe ion site in hematite.*

(c) *The Fe ions (white dots) are located in layers separated by O sites (red dots).*

Figure 2.1: *Crystal- and magnetic structure of hematite.*

lattice. Fig. 2.1c shows the crystallographic structure of hematite. This magnetic structure is shown in Fig. 2.1a which also defines the crystal axis. The Fe ions are located in layers, separated by intermediate layers of oxygen. These layers define the basal plane, which is the span of the crystal axis vectors $\hat{a}$ and $\hat{b}$.

The magnetic lattice is divided into two sublattices of aligned spins: The arrows in the figure represent spin orientations in the Néel state, which is a good approximation to the true antiferromagnetic ground state.

The magnetic structure can be determined by studying the Heisenberg Hamiltonian

$$H_{\text{ex}} = \sum_{ij} J_{ij} \mathbf{s}_i \cdot \mathbf{s}_j \tag{2.1}$$

which parameterizes the valence electron states by the spin operators. Electrical interactions between electrons on nearby sites make up the framework of the magnetic ordering. The interactions are due to exchange and su-

perexchange, and give rise to either alignment or anti-alignment among the spins of neighbouring sites. The strength of these interactions is given by the exchange constants J_{ij}. If $J_{ij} > 0$ (typical for superexchange, which is mediated by an oxygen site), the energy term $J_{ij}\mathbf{s}_i \cdot \mathbf{s}_j$ is minimized when $\mathbf{s}_i$ and $\mathbf{s}_j$ anti-aligned. If $J_{ij} < 0$ (typical for exchange), alignment is preferred. In hematite, J_{ij} is positive if i and j refer to neighbouring sites on different basal planes, and negative for neighbouring sites within the same basal plane. $J_{ij} \cong 0$ for sites that are further apart.

Due to the total effect of these interactions, spins in each basal plane tend to point in the same direction. This defines the sublattices; the aligned spins of every second basal plane. Spins of opposite sublattices are anti-aligned. This antiferromagnetic long-range ordering in hematite gradually breaks down at higher temperatures when spins more frequently enter excited states. At the Néel temperature ($T_N \cong 955K$), long-range order breaks down completely.

There are preferred directions for the collective orientation of the sublattices and these depend on the crystal anisotropies. There are two main anisotropy energy terms in hematite - a strong planar anisotropy of the (001) basal plane, and within the basal plane a weaker axial anisotropy. In nanoparticles, the effect of the strong planar anisotropy tends to confine spins to the basal plane. The axial anisotropy then defines preferred directions within the basal plane

The planar anisotropy is parameterized by the planar anisotropy constant κ_1. In bulk hematite, κ_1 changes sign as a function of temperature and this controls the magnetic Morin transition at $T_M \cong 267$K. Below this transition temperature κ_1 is positive, and the planar anisotropy causes spin to align perpendicular to the basal plane. In this phase, hematite is a *pure antiferromagnet*. As κ_1 becomes negative with increasing temperature, spins confine to the basal plane. Notice that spins in in Fig. 2.1a are aligned

within the basal plane, so the shown magnetic phase is above T_M. Hematite is *weakly ferromagnetic* in this phase due to a small sublattice canting, but I will not consider this weak effect of canting. See fig. 2.2a for the temperature dependency of the planar anisotropy in bulk and nanoparticle samples. Notice that the Morin transition is suppressed in nanoparticles (down to at least 5K [5]), and this is the reason that the planar anisotropy always confines spins to the basal plane in nanoparticles. Hematite nanoparticles are thus weakly ferromagnetic.

Within the basal plane, there are preferred directions due to the easy-axis, or axial anisotropy [6] [7]. Pointing along the axial anisotropy axis lowers the energy of spins, so this potential is attractive. It is governed by the microscopic anisotropy constant κ_2, which is positive. The axial anisotropy is in reality hexagonal [8], but I have for simplicity assumed that it is axial. I was able to fit data nicely in spite of this apparent inconsistency.

The effect of crystal anisotropies is described by the anisotropy Hamiltonian

$$H_{\text{anis}} = -\sum_i \kappa_1 (\mathbf{s}_i^x)^2 - \sum_i \kappa_2 (\mathbf{s}_i^z)^2. \tag{2.2}$$

The coordinate axis are chosen such that the y-z plane coincides with the crystallographic basal plane. The x axis thus coincides with the [001] direction and the crystal axis vector $\hat{c}$. The z direction is chosen along the axial anisotropy.

2.1.1 Hematite nanoparticles

Bulk crystals contain a very large number of sites and are usually treated using periodic boundary conditions, considering the existence of a surface irrelevant. The spinwave- and phonon spectrum in bulk is nearly continuous and microscopic physical properties such as anisotropy constants do not change from one sample to the next. Nanoparticles differ from bulk crystals on all of these points. The physical properties of nanoparticles are

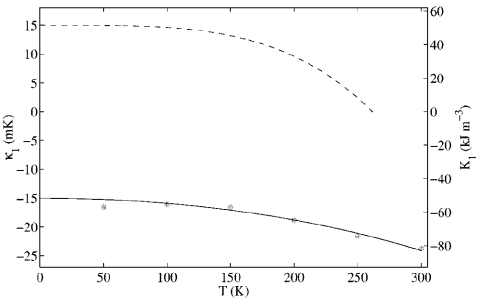

(a) *Temperature dependency of the strong planar anisotropy, in bulk hematite (dotted) and nanoparticles (solid). From Ref. [9].*

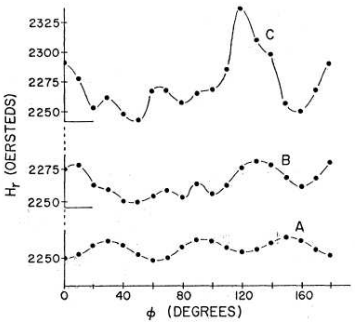

(b) *Stress dependency of the in-plane (axial) anisotropy studied using magnetic resonance. Applied stress increases from A-C. This anisotropy is hexagonal. From Ref. [8]*

Figure 2.2: *The crystal anisotropies of hematite are highly dependent on a number of microscopic parameters and highly sensitive to temperature and/or stress. A fundamental description of these dependencies is yet to be achieved.*

highly dependent on size and shape; periodic boundary conditions cannot be applied; and surface effects are important.

Hematite nanoparticles are defined as nano-sized crystallites of $\alpha-Fe_2O_3$. Fig. 2.3a shows such a transmission electron microscope (TEM) picture of a particle of about 8 nm in diameter. This particle was coated to minimize inter-particle interactions. Fig. 2.3b shows a sketch of the magnetic submagnetizations.

It is known from experiments that the anisotropy constants of hematite nanoparticles may vary by orders of magnitude, depending on size [10]. The temperature dependency in κ_1 is completely different in nanoparticles and bulk [9] (see Fig. 2.2a). It is reported that κ_2 increases with decreasing particle size [5, 11]. It is also known that the anisotropy variations are related to size- and temperature dependent lattice contraction and expansion, but the sensitivity is not directly related to a single factor such as the lat-

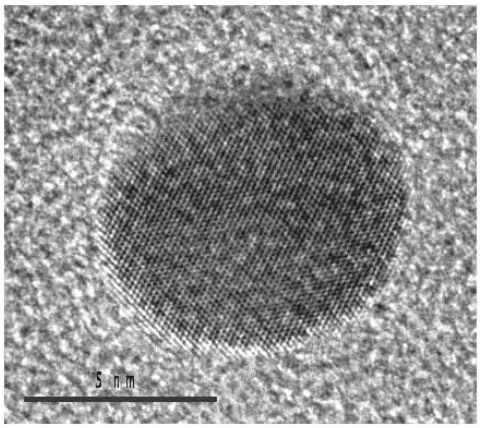

(a) *Transmission electron microscopy picture of a small hematite nanoparticle [ref], The nanoparticle is coated to prevent inter-particle interactions.*

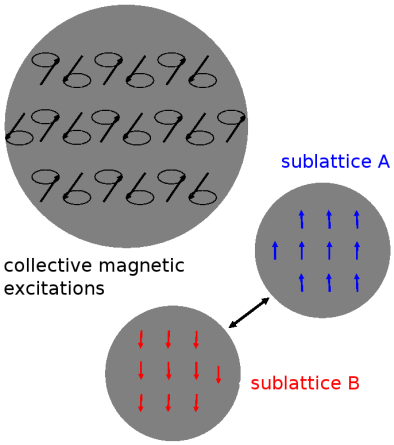

(b) *Schematic of the two sublattices in an antiferromagnetic nanoparticle and an artists impression of a collective precession.*

Figure 2.3: *Hematite nanoparticles such as the ones shown above feature complex magnetic dynamics and behave quite differently from bulk crystals.*

tice parameter [12]. The effective anisotropies may depend on competing energies with different temperature dependencies. In bulk samples the axial anisotropy is indeed very sensitive to stress [8] (see Fig. 2.2b).

Notice that the individual Fe sites in each layer of the crystal are slightly perturbed out of the basal plane. This makes the local electrostatic environment of hematite very complex. Perhaps this is the basis for the complicated crystal fields that make up the anisotropies, and other effects such as the sublattice canting. (See fig. 2.1b for a close-up on the near-octagonal environment an Fe site).

Furthermore, the subject of surface effects is complicated and controversial. The local environment at the surface is such that spins at surface sites can behave very differently from internal sites. Yet they are still coupled to internal sites by the exchange interactions, and this affects the overall dynamics. The surface effect of uncompensated moments is explored in [13].

2.1.2 Magnetic dynamics in nanoparticles

Antiferromagnetic particles of a diameter below ∼100 nm are often fine enough to become single-domain, and one can define the total magnetic moment of each sublattice as the sum of the moments due to all the spins on that sublattice. The total magnetic moment of a sublattice is called a *submagnetization*. The submagnetizations behave as regular magnetic moments, but are strongly coupled due to the interaction between spins of opposite sublattices. The sublattices, and thus the submagnetizations, are always very close to being perfectly anti-aligned.

It is the dynamics of the submagnetizations that is the subject of study in this thesis. However before this discussion can continue, a few considerations on the general magnetic excitations of a magnetic nanoparticle are required. The following is an approximate description.

Magnetic excitations – spinwaves

The magnetic excitations of a hematite nanoparticle are studied through the total Heisenberg Hamiltonian of the nanoparticle system, which is

$$H = H_{\text{ex}} + H_{\text{anis}} \tag{2.3}$$

$$= \sum_{ij} J_{ij}\mathbf{s}_i \cdot \mathbf{s}_j - \sum_i \kappa_1 (\mathbf{s}_i^x)^2 - \sum_i \kappa_2 (\mathbf{s}_i^z)^2 \tag{2.4}$$

I will refer to this as the Heisenberg Hamiltonian. Low temperature excitations to the Heisenberg Hamiltonian are called spinwaves or magnons. The name spinwave has probably been chosen because the elementary excitations are described by the spacial Fourier transform of the spin operators $\mathbf{s}_i$. They are characterized by a wavevector $\mathbf{q}$ and are thus waves.

In nanoparticles, the spinwave energy spectrum is quantized due to the non-periodic boundary conditions given by a finite crystal. (See [14] for a theoretical investigation in fcc and bcc clusters). This means that there are

only spinwaves of very specific energies, as opposed to the nearly continuous spectrum in bulk crystals. At low temperatures the thermal spinwave population is dominated by the lowest spinwave excitation, which has the wavenumber $q = 0$. In antiferromagnetic nanoparticles, these excitations are known as collective magnetic excitations (CME) because spins of each sublattice precess in phase, or collectively. This collective motion can therefore be considered from the point of view of the motion of the submagnetizations. It is the size quantization gap that separates the collective dynamics from the dynamics of higher spinwave excitations.

See Fig. 2.4c for a graph of the dispersion relation for bulk hematite by Samuelsen and Chirane [15]. I have zoomed in on small q values and added the horizontal lines that indicate the size quantized energy levels, in Fig. 2.4a. The spinwave dispersion relation reported in [15] for small values of q is:

$$\varepsilon(q) = Jaq + \varepsilon_0 = 200\frac{\text{meV}}{\text{nm}}q + \varepsilon_0. \tag{2.5}$$

The shortest non-zero standing wave in a nanoparticle has half a wavelength along the particle, i.e. $\lambda_{\max} \cong 2d$. For 8 nm hematite particles $\lambda_{\max} = 16$ nm which gives $q_{\min} = \frac{2\pi}{\lambda_{\max}} = 0.039$ nm^{-1}. This gives an energy gap of

$$\Delta\varepsilon_{q_{\min}} = Ja\frac{2\pi}{\lambda_{\max}} = Jaq_{\max} = 8 \text{ meV}. \tag{2.6}$$

In comparison, the $q = 0$ spinwave energies are $\varepsilon_0 \cong 0.26$ meV and $\cong 1.1$ meV. The occupation of $q = 0$ spinwaves is shown in Fig. 2.4b[a]. The collective dynamics is clearly dominant in these particles.

Collective magnetic excitations in nanoparticles were discovered using Mössbauer spectroscopy long before I was born [16] and may be thought of as precessions of the submagnetizations in the fictitious fields of exchange and anisotropy interactions. From this point of view the submagnetization

[a]The occupation is $p = \frac{1}{Z}p_0$ where $p_0 = \sum_{\varepsilon_0}\exp(-\beta\varepsilon_0)$ is the $q = 0$ levels and $Z = p_0 + \sum_{i=1}^{\infty}\exp\left(-\beta\frac{2\pi Ja}{d}i\right) = p_0 + \sum_{i=1}^{\infty}x^i = p_0 + \frac{1}{1-x} - 1$, for $x = \exp\left(-\beta\frac{2\pi Ja}{d}\right)$.

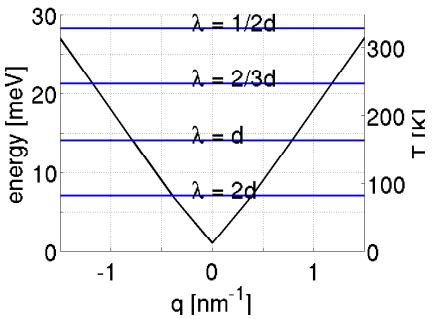

(a) The horizontal lines indicate size quantization levels.

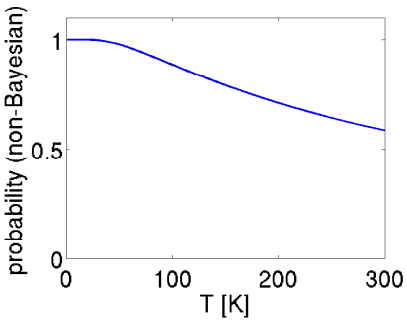

(b) Theoretical occupation of $q = 0$ states.

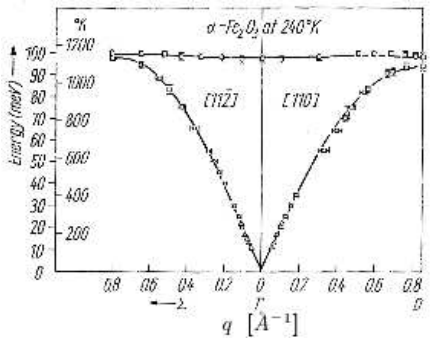

(c) Spinwave disperson relation for bulk hematite. From [15].

Figure 2.4: *Spinwave dispersion relation for hematite and spinwave quantization in nanoparticles.*

system is classical. The identification with quantum mechanical spinwaves of wavenumber $q = 0$ has since been made (see [7], [6] and [9]). It was originally detected by the use of magnetic resonance techniques that these modes are also present in bulk crystals [17]. The energy levels are shifted in nanoparticles due to various finite-size effects, among which we find the strong size dependency of anisotropies.

Superparamagnetism

The reader should now tune his/her mind into the classical viewpoint of submagnetization dynamics. Considering the submagnetization orienta-

tions precisely antiparallel, the macroscopic anisotropy energy of a hematite nanoparticle is found by taking the sum in the anisotropy Hamiltonian (2.2). The result is

$$E_{\text{anis}} = -\kappa_1 s^2 N \cos^2(\theta)\sin^2(\phi) - \kappa_2 s^2 N \cos^2(\theta) \tag{2.7}$$

where κ_1 and κ_2 are the anisotropy constants, $s^2 = s(s+1) = \frac{5}{2}(\frac{5}{2}+1)$ and N is the total number of sites. (θ, ϕ) are the spherical coordinates

$$(x, y, z) = (\cos(\theta)\sin(\phi), \sin(\theta)\sin(\phi), \cos(\phi)).$$

This function is visualized in Fig. 2.5.

The height of the anisotropy barriers is given in microscopic terms by

$$-s^2 N \kappa_i \tag{2.8}$$

for $i = 1, 2$, and in macroscopic terms by

$$-K_i V \tag{2.9}$$

where K_i is the anisotropy constant and V the particle volume. It is important to keep in mind that the anisotropy energy barrier height depends on the size of the particle, N or V.

In 1949, Néel proposed that the magnetization of a fine ferromagnetic particle might stochastically cross the axial anisotropy energy barrier due to thermal excitations [18]. This is called a superparamagnetic relaxation, and illustrated by the red arrows in Fig. 2.5. The theory was perfected by Brown in 1963 who treated the problem stochastically, and derived an expression for the mean flip time which is given by

$$\tau = \tau_0 \exp\left(\frac{KV}{k_B T}\right). \tag{2.10}$$

This is the Néel-Brown law [19]. KV is the anisotropy barrier (the equivalent of (2.9) with $i = 2$) and τ_0 depends on the system and the environment.

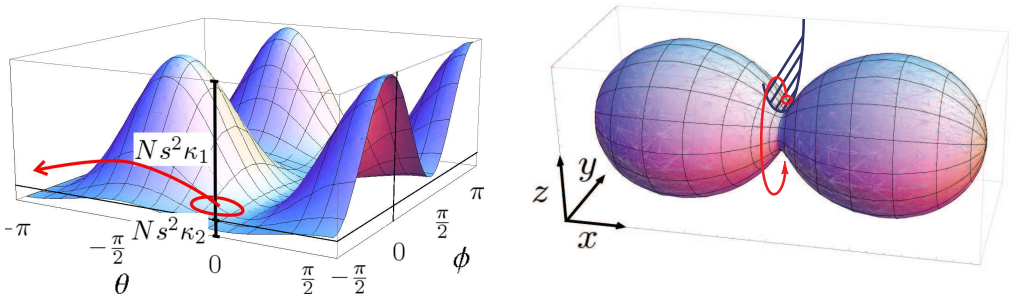

(a) *The anisotropy energy in spherical coordinates. $\theta = 0$ indicates the north pole.*

(b) *Mapped onto the sphere. The 1-D harmonic oscillator approximation is symbolized.*

Figure 2.5: *Anisotropy energy of a hematite nanoparticle. In the same coordinate systems, a superparamagnetic flip from the north pole to the south pole is indicated by the red arrows (in cartesian coordinates from (0,0,1) to (0,0,-1)).*

This phenomenon of spontaneous magnetization reversal is called superparamagnetism (SPM) and was initially investigated in the 50's by the use of magnetization measurements, since the 60's by Mössbauer spectroscopy and finally by neutron scattering since the 90's. The phenomenon was recently verified experimentally for single a particle [20]. Studies of superparamagnetism are of considerable interest to the magnetic data storage industry. This is by the way the most relevant technological application of iron oxides.

Antiferromagnetic particles also exhibit superparamagnetism. Since the submagnetizations always point in generally opposite directions, a superparamagnetic relaxation occurs when the submagnetizations relax simultaneously. Superparamagnetic behavior in antiferromagnetic particles has been observed since the 1960's, for example by Néel himself. The mean flip time follows the Néel-Brown law, see for example [7].

The existence of superparamagnetism and collective magnetic excitation modes has been verified for hematite nanoparticles [6] [10]. In 15 nm hematite nanoparticles the submagnetizations are confined to the basal plane

such that superparamagnetic dynamics is essentially one-dimensional and controlled by the axial anisotropy potential. The planar anisotropy is so large in these particles that it may be considered infinite, and the spins are completely confined to the basal plane. For small excitation amplitudes of the submagnetization motion within the basal plane, the axial anisotropy potential may be approximated by a 1-D simple harmonic oscillator, which goes as $\sim \theta^2$. The ressonance frequency of the oscillator corresponds to that of the axial collective precession mode. For larger precession amplitudes, the precession frequency is reduced due to the fact that the anisotropy potential goes as $\sim \cos^2 \theta$ and is therefore locally a bit "weaker" than the harmonic oscillator. This is called the anharmonic effect. This effect was observed in [7] for 15 nm hematite nanoparticles, where a slight decrease of the collective excitation energy was observed with increasing temperature. However, 8 nm hematite nanoparticles can not be satisfactorily understood within the 1-D model, which is why I consider the more detailed potential shown in Fig. 2.5.

The theoretical treatment of antiferromagnetic superparamagnetism is usually done in terms of correlation function calculations. An example that relates to 15 nm hematite data is found in the paper by Lee [21], where the role of the exchange interaction is inluded. However that paper is rather technical, comparison with data is not done in a transparent way and the author couples the sublattices to a specific heat bath composed of phonons, which is a specific assumption. In this thesis I will determine the correlation function numerically, in a different and more intuitive way and use a generic heat bath.

Table 2.1 shows values for the microscopic anisotropy and exchange constants in 8 nm hematite. The exchange constant is much stronger than the planar anisotropy, which is in turn stronger than the axial anisotropy. I have initially assumed that the exchange interaction in nanoparticles is the same

as in bulk. The anisotropy constants of nanoparticles are not well known and are very size dependent. The value of κ_1 is not known for 8 nm hematite so I have used the value and temperature dependency of κ_1 reported for 15 nm particles in [9] (see Fig. 2.2a). The chosen value of $\kappa_2 = \frac{1}{10}|\kappa_1|$ will give a value for the collective excitation energy that is close to the measured value. κ_2 is considered independent on temperature. This choice of values reflects the situation in which the planar anisotropy is indeed stronger than the axial anisotropy, but only by a single order of magnitude. Later on a precise set of parameters will be determined by fitting to experimental data.

symbol	quantity	bulk	$8nm$ nanoparticles
ZJ	inter-sublattice exchange	$207K$ [a]	$207K$
κ_1	planar anisotropy energy		$-15 \cdot 10^{-3}K$ [b]
κ_2	axial anisotropy energy		$\frac{\lvert\kappa_1\rvert}{10} = 1.5 \cdot 10^{-3}K$ [c]

[a] From Ref. [1]
[b] From Ref. [9]
[c] This parameter is strongly dependent on particle size [5]. For now, a value for κ_2 that is 10 times smaller than the planar anisotropy has been chosen.

Table 2.1: *Approximate values of the most important micro-magnetic constants of 8 nm hematite.*

2.2 Inelastic neutron scattering

Neutrons are spin-half particles and thus carry a magnetic moment. Neutrons have no charge so they do not probe charge densities (as X-rays do), but only nuclear (i.e. crystallographic) and magnetic structure. Neutrons of $T = 300$K have a wavelength $\lambda = 1.8$Å and an energy $E = 25$ meV, and are therefore able to probe the typical sizes and energy levels in solid state physics. This makes thermal neutrons ideal magnetic probes. The lack of charge makes neutrons technically difficult to handle, and neutron

optics consists mainly of supermirrors, neutron guides and crystals selected for Bragg scattering. The theory of thermal neutron scattering is found in [22].

Fig. 2.6a shows the neutron spectrometer RITA II which is a 3-axis spectrometer located at PSI, Switzerland [23]. The first axis is a monochromator crystal, that specifies the incoming beam energy by means of the Bragg scattering condition $q = \Delta k$ where $\Delta k = \kappa$ is the scattering vector and q a reciprocal lattice vector of the monochromator. The second axis rotates the sample, and the third is an energy analyzer. The energy distribution of the outgoing neutron beam can, among many other things, be used to determine if neutrons excite or absorb definite amounts of energy in the sample. This technique, known as inelastic neutron scattering, can probe the energy of quantum transitions in the sample, for example absorption or excitation of collective magnetic excitations in hematite nanoparticles.

2.6b shows the backscattering spectrometer BSS located in Jüllich, Germany [24]. The monochromator and analyzer crystals mechanically Doppler shift neutron wavelengths with respect to the sample. This gives the spectrometer a very high energy resolution, at the cost of momentum transfer resolution.

2.2.1 Recent experiments on 8 nm hematite nanoparticles

A hematite particle of $d = 8$ nm has about $1.06 \cdot 10^4$ Fe(III) sites[b]. Calculated from (2.8) the axial anisotropy barrier is therefore about $\frac{5}{2}(\frac{5}{2}+1) \cdot 1.06 \cdot 10^4 \kappa_2 \cong 140$ K. One might therefore imagine that above this temperature the classical picture of collective precessions and superparamagnetism could break down in these nanoparticles. After all, in deriving (2.10) Brown supposed that $KV > k_B T$. A regime of motion with no preferred direc-

[b] $N = \frac{M}{m} = \frac{V\rho}{m_{\mathrm{Fe}} + \frac{2}{3}m_{\mathrm{O}}} = 1.06 \cdot 10^4$, where V is the particle volume, ρ the density of hematite and $m = m_{\mathrm{Fe}} + \frac{2}{3}m_{\mathrm{O}}$ the weight for each Fe(III) site.

(a) *RITA-II, triple-axis spectrometer at PSI, Switzerland*

(b) *BSS of Jülich, a high resolution backscattering spectrometer. Now replaced by SPHERES at FRM2, Münich*

Figure 2.6: *Typical neutron instruments.*

tion within the basal plan could arise. Such dynamics might treat KV as a perturbation rather than a barrier. Such a phenomena could be termed isotropic relaxation. One manifestation of isotropic relaxation predicted for ferromagnetic particles in [25], is a regime where precession is replaced by increasingly random motion due to strong thermal fluctuations. The 15 nm particles did not show signs of such behavior, but their barrier is about 7 times larger than that of 8 nm particles. Therefore the difference in behavior between the samples could be enormous.

In order to investigate size dependencies in general, a powder sample of 7.5-11 nm (primarilly 8 nm) hematite nanoparticles was prepared and studied by inelastic neutron scattering. Particles were coated to suppress interparticle interactions which had earlier been significant [26]. At temperatures ranging from 10-300K, the collective spin relaxation spectrum within the basal plane was observed by RITA II. This experiment was conducted by Stine N. Ancona (previously Klausen), Christian R. H. Bahl, Cathrine Frandsen, Luise T. Kuhn and Kim Lefmann. Superparamagnetism measurements with the high-resolution instrument BSS were also done, by Christian

R. H. Bahl, Kim Lefmann, Jalthe S. Jacobsen, Luise T. Kuhn and Andreas Wischnewski. All fits to experimental data were done by Luise T. Kuhn and Kim Lefmann.

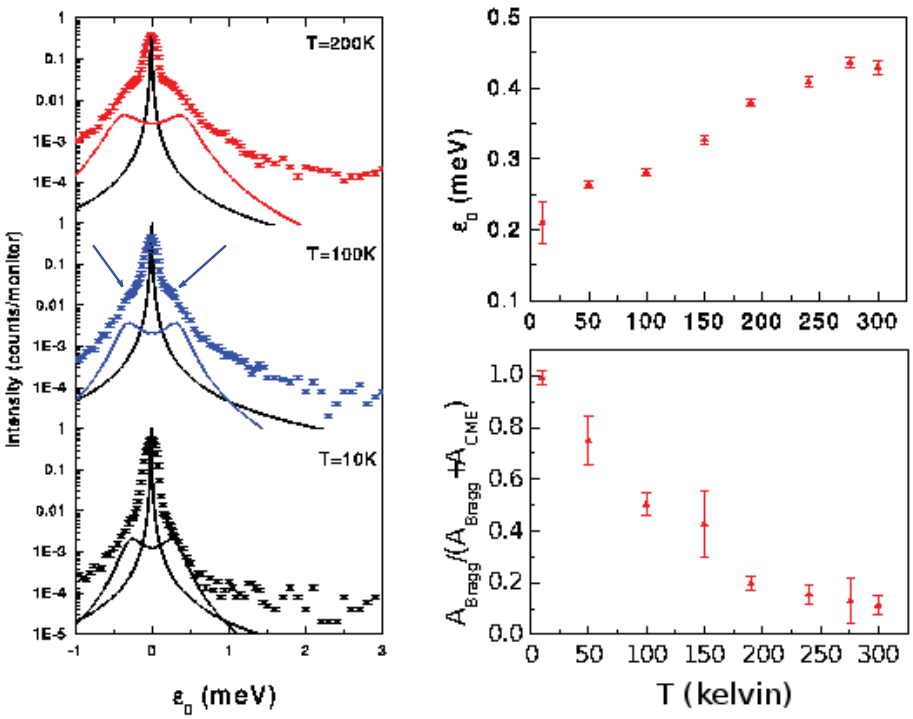

Figure 2.7: *Recent experiments exploring the regime* $k_BT > KV \sim 15\ K$.

Typical RITA II data is shown in fig. 2.7. The scattering spectra represent collective spin relaxation in the basal plane. I will return to what this means in a moment, for now it is enough to consider an interpretation of the experiment: The strong central peak is the static antiferromagnetic peak, broadened with temperature due to increased superparamagnetic activity. The shoulders indicated by arrows are sidepeaks and represent absorption and excitation of $q = 0$ spinwaves[c], or resonance of neutrons with the axial

[c]The shoulders are barely visible. This is because the central peak is the mix of the static/superparamagnetic peak, and a strong peak due to incoherent scattering of water in the sample.

collective precession mode. The position of the sidepeaks is fitted by the parameter ε_0. At low temperatures the peak position is constant, and up to ~ 150 K the experiment is understood and the results published in [10]. However from about ~ 150 K the peak position grows – as if the energy of the collective mode increased with temperature. However this is the opposite of what is expected from the anharmonic effect, and therefore both unexpected and unexplained.

In this thesis I will persue a model for the entire collective dynamics and through that hope to find an explanation for the strange behavior that is the increase of ε_0.

Relating theory to experiment

The measured quantity is the inelastic magnetic scattering cross-section $\frac{d^2\sigma}{d\Omega dE_f}$. Due to the experimental setup (see [10]), the scattering cross-section is proportional to the following function

$$\frac{d^2\sigma}{d\Omega dE_f} \quad \sim \quad \int dt\ e^{i\omega t} < S_y(0)S_y(t) > + < S_z(0)S_z(t) > \qquad (2.11)$$

The right hand side of (2.11) is the correlation function $S_{yy}(\omega) + S_{zz}(\omega)$. This function contains information about the collective spin relaxation in the basal plane of nanoparticles in the sample. The neutrons were unpolarized and therefore unable to distinguish the sublattices, so the measure quantity is the correlation function of their mutual orientation.

The correlation function can be calculated theoretically from knowledge of the sublattice trajectories. This is done using the Wiener-Khintzhine theorem, which states that

$$< P_\alpha(\omega) > \sim \int dt\ e^{i\omega t} < S_\alpha(0)S_\alpha(t) > \qquad (2.12)$$

where $< ... >$ on the left hand side of (2.12) denotes the time average. The power spectrum is the absolute square of the Fourier transform of the time

evolution of the submagnetization. The Wiener-Khintzhine formula (2.12) relates (2.11) to sum of the averaged power spectra of $S_y(t)$ and $S_z(t)$,

$$P(\omega) = P_y(\omega) + P_z(\omega) \tag{2.13}$$

such that theory and experiment can be compared by

$$\frac{d^2\sigma}{d\Omega dE_f} \sim P(\omega). \tag{2.14}$$

A proof of (2.12) is given in appendix A.

A strategy is now formed:

1) Find an equation of motion for the submagnetizations. This describes the collective motion of sublattice spins as they are affected by exchange and anisotropies.

2) Include the effect of temperature on the system using the statistical approach of Langevin dynamics.

3) Use a numerical technique to simulate trajectories and compare model to experiment using formula (2.14). Inspiration is found in [27] and [25].

Chapter 3

Theory

The submagnetizations of a hematite nanoparticle are isolated from general spin dynamics by the size quantization, and their motion can be treated classically. The goal of this chapter is to construct a model that describes the collective precession modes, and then couple this model to a generic heat bath using the technique of Langevin dynamics. If the picture of the antiferromagnetic nanoparticles described in chapter 2 is correct, all experimentally observed effects should arise from this model.

I will start by looking at the quantum mechanical description of the collective modes, and find the energy of the $q = 0$ spinwave excitations.

Then I will move on the the classical description of collective states and determine an equation that describes these spinwaves as collective resonance modes.

Finally the model is expanded to include interactions with a heat bath by means of a phenomenological picture of fluctuation and dissipation.

3.1 Spinwave description of the collective modes

The Heisenberg Hamiltonian is the starting point for many calculations in magnetism. See Blundell: "Magnetism" [3], the book by Martín [28] or

Yosida: "Theory of Magnetism" [4] for in-depth calculations. As discussed in section 2.1.2, the Heisenberg Hamiltonian of a hematite nanoparticle system captures the antiferromagnetic ordering and exchange interaction and the effects of planar and axial anisotropies. Recall that the Heisenberg Hamiltonian is

$$H = \sum_{ij} J_{ij} \mathbf{s}_i \cdot \mathbf{s}_j - \kappa_1 \sum_i (s_i^x)^2 - \kappa_2 \sum_i (s_i^z)^2 \tag{3.1}$$

where κ_1 is the microscopic planar anisotropy energy which is negative for hematite nanoparticles and κ_2 is the positive, weaker axial anisotropy constant. The y-z plane was chosen to coincide with the crystallographic basal plane (see fig. 2.1). Due to the signs of the anisotropy constants, the anisotropy energy is minimal when spins of one sublattice point in the positive z direction, and spins of the other sublattice point in the negative z direction. At low temperatures the magnetic state is close to the classical Néel state (see Fig. 2.1a).

The lowest lying excitations of the Heisenberg Hamiltonian (3.1) are the collective magnetic excitations or coherent spin waves, states in which spins of each sublattice precess collectively. I will explain how the energy of such excitations is found. The resulting expressions correspond to the classical result for magnetic resonance [17]. These are used to cross-check the numerical method and simulation results later in this thesis.

Consider the following general consideration: Let $|0\rangle$ be an antiferromagnetic groundstate. Let Q be the creation operator for a low-lying state. This operator satisfies $Q|0\rangle = |q\rangle$ where $|q\rangle$ is an eigenstate of H. We can

determine the equation of motion for Q:

$$\begin{aligned} H|q\rangle &= HQ|0\rangle \\ &= (QH + [Q,H])|0\rangle \\ &= QE_0|0\rangle + [Q,H]|0\rangle \\ &= E_0|q\rangle + [Q,H]|0\rangle. \end{aligned}$$

Since

$$H|q\rangle = E_q|q\rangle,$$

we can continue with

$$\begin{aligned} E_q|q\rangle &= E_0|q\rangle + [Q,H]|0\rangle \\ (E_q - E_0)\,Q|0\rangle &= [Q,H]|0\rangle. \end{aligned}$$

I.e Q must satisfy the equation

$$[Q,H]|0\rangle = \varepsilon_0 Q|0\rangle \tag{3.2}$$

where $\varepsilon_0 = E_q - E_0$ is the eigen-energy to be calculated. In the Heisenberg picture, the equation of motion for the time dependent operator Q is

$$i\hbar\frac{\partial Q}{\partial t} = [Q,H]. \tag{3.3}$$

Since Q is a perturbation to the ground state, it may be written as a linear combination of perturbations to the individual spins. Therefore Q must be some linear combination of the spin ladder operators:

$$Q = \sum_i a_i s_i^+ + \sum_i b_i s_i^- \tag{3.4}$$

where i runs over the entire magnetic lattice. The ladder operators are given by $s^\pm = s^x \pm i s^y$.

There are many choices of Q that satisfy these requirements. The general excitation states are the mentioned spinwaves, and the general form of Q

is known from spinwave theory (see [4]). For our purposes it is sufficient to know that collective excitations are the lowest-lying excitations, have the wavevector $q = 0$ and are realized when Q is a linear combination of the operators $S^{\pm} = \sum_i s_i^{\pm}$ and $T^{\pm} = \sum_j t_j^{\pm}$. Here, $S^{\pm}$ only operates on sublattice A and $T^{\pm}$ only on sublattice B, i is the index of sublattice A and j is the index of sublattice B. (The operators t are the same as the s operators, but rotated around the x axis by π: $t_l^x = s_l^x, \quad t_l^y = -s_l^y$ and $t_l^z = -s_l^z$. This notation is convenient in calculations).

One should now proceed by calculating the commutators $[S^{\pm}, H]$ and $[T^{\pm}, H]$. The result is (see [13] for more detail):

$$[S^{\pm}, H] = \pm 2s \sum_{ij} J_{ij}(t_j^{\mp} + s_i^{\pm}) \mp \kappa_1 s'(S^+ + S^-) \pm \kappa_2 2s' S^{\pm} \quad (3.5)$$

$$[T^{\pm}, H] = \pm 2s \sum_{ij} J_{ij}(s_i^{\mp} + t_j^{\pm}) \mp \kappa_1 s'(T^+ + T^-) \pm \kappa_2 2s' T^{\pm}. \quad (3.6)$$

where $s = \frac{5}{2}$ and $s' = \frac{5}{2} - \frac{1}{2}$ for hematite.

In working out the details, all intra-sublattice terms such as $J_{ii'}(s_{i'}^{\mp} + s_i^{\pm})$ have cancelled out. This means that in the $q = 0$ mode, spins only interact with sites on the opposite sublattice. It may seem strange that intra-sublattice bonds do not enter the dynamics of the submagnetizations, but in a way they actually do: The intra-sublattice $J_{ii'}$ terms cause an energy gap to the next spinwave modes, thus securing the classical model of two coupled, precessing submagnetizations.

3.1.1 Coherent potential approximation

There is a natural way to approximate an exchange sum

$$\sum_{ij} J_{ij}(t_j^{\mp} + s_i^{\pm}) \quad (3.7)$$

in (3.5), and the corresponding sum in (3.6), by it's weighted average value. In bulk calculations one would apply periodic boundary conditions to such

sums, but since the local environment of a site depends on position in the nanoparticle, another approximation method is required: Surface sites have a smaller number of neighbours than internal sites, and are therefore affected by different interactions. See Fig. 3.1a for an intuitive sketch of situation at the surface of a magnetic nanoparticle. The coherent potential approximation (CPA) finds an average value for the the potential acting on a site. Thanks to Per-Anker Lindgård in pointing this out, and referring to [29] for a review.

With respect to the $q = 0$ modes, the coherent potential is determined intirely by the opposite sublattice. Consider the sum $\sum_{ij} J_{ij}$ and split it into the sum of internal sites and surface sites. This can be done in two ways. First with respect to sublattice A of index i:

$$\sum_{ij} J_{ij} \quad = \quad \left(\sum_{\mathrm{int},i} + \sum_{\mathrm{surf},i} \right) \sum_{j} J_{ij} \tag{3.8}$$

Then, taking the sum over j, an internal site on sublattice A is assumed to have Z^A_{int} neighbours each supplying an exchange interaction potential of size J. A surface site is assumed to have Z^A_{surf} neighbours on average. As J is the *unit* interaction strength, Z^A_{int} and Z^A_{surf} need not be integers. The product $Z^A_{\mathrm{int}}J$ (or $Z^A_{\mathrm{surf}}J$) is simply the inter-sublattice exchange potential felt by individual internal (or surface) sites of sublattice A. After summing over i we get

$$\sum_{ij} J_{ij} \quad = \quad \sum_{\mathrm{int},i} J Z^A_{\mathrm{int}} + \sum_{\mathrm{surf},i} J Z^A_{\mathrm{surf}} \tag{3.9}$$

Considering all internal sites, and all surface sites, exposed to equivalent interactions we can take the sum over i and arrive at

$$\sum_{ij} J_{ij} \quad = \quad J \left(Z^A_{\mathrm{int}} N^A_{\mathrm{int}} + Z^A_{\mathrm{surf}} N^A_{\mathrm{surf}} \right) \tag{3.10}$$

The term in the brackets of (3.10) is denoted K and is equal to the total number of inter-sublattice bonds in the particle. Every bond connects

two sites – one on each sublattice. This is the same as saying that J_{ij} is symmetrical, and the reason why K could also be calculated by summing over i before j:

$$K = Z^A_{\rm int} N^A_{\rm int} + Z^A_{\rm surf} N^A_{\rm surf} \tag{3.11}$$

$$= Z^B_{\rm int} N^B_{\rm int} + Z^B_{\rm surf} N^B_{\rm surf} \tag{3.12}$$

The coherent potential acting on each site on sublattice I is defined as the weighted average of the potential on internal and surface sites

$$J(0)^I_{\rm av} = \frac{JK}{N^I}. \tag{3.13}$$

In the CPA the problematic sum (3.7) becomes

$$\sum_{ij} J_{ij}(t^{\mp}_j + s^{\pm}_i) \cong \frac{JK}{N^B}\left(S^{\mp} + \frac{N^B}{N^A}T^{\pm}\right). \tag{3.14}$$

I will use the CPA to approximate similar sums later on.

Uncompensated moments

The excess number of spins on one sublattice compared to the other leads to the existence of uncompensated moments. The excess amount was proposed by Néel to be in the order of $\sqrt{N}$, due to the random placement of the surface. The uncompensated moment is parametrized by

$$\xi = \frac{N^A}{N^B} \tag{3.15}$$

and this parameter enters the dynamical equations and modifies the coherent potential, for example through 3.14. However, I will not dwell on this effect or use it in any of the numerical calculations. Recently a paper by C. R. H. Bahl, J. Garde, K Lefmann, T.B.S. Jensen, P-A Lindgård, D. E. Madsen and S. Mørup was accepted by the Europhysics Journal [13]. This paper discusses this surface effect and its influence on the collective mode energies and can be found in appendix D. The dynamical effect of uncompensated

moments is small in the strongly planar case $|\kappa_1| \gg |\kappa_2|$ that is treated in this thesis[a]. The difference between the sublattices is nevertheless included in most expressions.

Bulk value for J(0)

Now that the dynamical effect of uncompensated moments is small, I have used the nearest-neighbour approximation to get the value $ZJ = J(0)^I_{\rm av}$ for bulk hematite,

$$J(0)^A_{\rm av} = J(0)^B_{\rm av} \equiv ZJ = 3J_3 + 6J_4 = 207 \text{ K}. \tag{3.16}$$

The value was found in the hematite book by Morrish [1] and has a large uncertainty. This is just a starting point – the exchange interactions may very well differ in nanoparticles from bulk values, just as the anisotropies do. See Fig. 3.1b for a drawing of the super-exchange paths giving rise to J_3 and J_4. There are three inter-sublattice neighbours of exchange type 3 and 6 neighbours of exchange type 4, and these are the most important.

3.1.2 Collective excitation energies

Returning to the eigenvalue problem (3.2). After going through the calculations presented in [13], one arrives at the $q = 0$ spinwave excitation energies:

$$\varepsilon_x = \pm 2\sqrt{(-\kappa_1 + \kappa_2)s'(J(0)s + \kappa_2 s')} \tag{3.17}$$

$$\varepsilon_y = \pm 2\sqrt{\kappa_2 s'(J(0)s + (-\kappa_1 + \kappa_2)s')} \tag{3.18}$$

The existence of these eigenenergies proves that there are quantum states in which the time evolution of individual spins are identical. Otherwise an equation that is linear in $S^\pm$ and $T^\pm$ (3.5 and 3.6 after adding 3.14) would not have solutions. In a semiclassical interpretation, spins in these states

[a] This is in spite of the remarks in [13] that $|\kappa_1| \sim |\kappa_2|$ in 8 nm hematite.

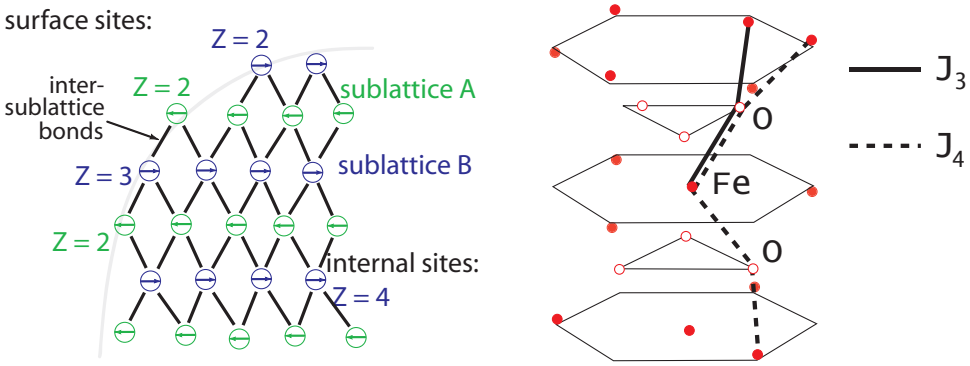

(a) *Intuitive sketch of sites near the surface of a nanoparticle. All internal sites have the same number of neighbouts (here $Z = 4$), while sites on the surface have fewer neighbours and therefore feel a weaker exchange potential.*

(b) *The most important super-exchange paths in bulk hematite. The hexagons represent basal planes. Compare to Fig. 2.1a. From Ref. [1] p. 60.*

Figure 3.1: *Exchange in hematite and the situation near the surface of a nanoparticle.*

precess collectively. As seen in [9] each spinwave energy corresponds to a precession of the submagnetizations in fictitious magnetic fields that correspond to the effect of anisotropies and exchange. By Bohr's correspondence principle, the energy of such semiclassical modes is given by $\varepsilon = \hbar\omega$ where ω is the precession frequency, but it is much simpler to think of ω as a resonance frequency of a classical system. The presence of $\hbar$ then refers to the probing neutrons, which are quantized. In chapter 4 it will be illustrated how the submagnetizations precess in strongly elliptical modes, each depending on one anisotropy. The suffices of (3.17) and (3.18) – y and x – are chosen strategically according to the axis orientation. The energy ε_y corresponds to precessions in the y direction within the basal plane of frequency ω_y, and ε_x corresponds to precessions out of the basal plane in the planar anisotropy, of frequency ω_x.

Define the fictitious anisotropy- and exchange fields as

$$B_X^I = \frac{|J(0)^I_{\rm av}|s}{g\mu_B} \tag{3.19}$$

and

$$B_{\kappa_i} = \frac{|\kappa_i|s'}{g\mu_B}. \tag{3.20}$$

where g is the g-factor and $\mu_{\rm B}$ is the Bohr magneton. Under the approximation $B_X \gg B_1 \gg B_2$ the energies (3.17) and (3.18) reduce to the known expressions for antiferromagnetic resonance [17]:

$$\hbar\omega_x = 2g\mu_B\sqrt{B_1 B_X} \tag{3.21}$$

$$\hbar\omega_y = 2g\mu_B\sqrt{B_2 B_X}. \tag{3.22}$$

I will now turn to the problem of determining the classical equation of motion for the superspins of each sublattice, but from a semiclassical point of view. This equation should describe precession modes with the frequencies

$$\hbar\omega_x = \pm 2g\mu_B\sqrt{(-B_1+B_2)(B_X+B_2)} \tag{3.23}$$

$$\hbar\omega_y = \pm 2g\mu_B\sqrt{B_2(B_X+(-B_1+B_2))}. \tag{3.24}$$

3.2 Semiclassical model

The collective motion of spins of each sublattice can be described by the superspins:

$$\mathbf{S}^A = \sum_l \mathbf{s}_l \tag{3.25}$$

$$\mathbf{S}^B = \sum_i \mathbf{s}_i. \tag{3.26}$$

The equation of motion for the superspins is

$$i\hbar\frac{\partial \mathbf{S}^I}{\partial t} = [\mathbf{S}^I, H] \tag{3.27}$$

$$= [\mathbf{S}^I, \sum_{ij} J_{ij}\mathbf{s}_i\cdot\mathbf{s}_j + \sum_i(-\kappa_1(s_i^x)^2 - \kappa_2(s_i^z)^2)] \tag{3.28}$$

where $I = A$ or B is the sublattice index. By evaluating (3.27) and taking the expectation value, an equation of motion for the submagnetizations is determined. The expectation value of a superspin is

$$\mathcal{S}^A = \langle \mathbf{S}^A \rangle. \tag{3.29}$$

By identifying the coordinates of the expectation values of individual spins on each sublattice, i.e. taking

$$\langle \mathbf{s}_i \rangle = \langle \mathbf{s}_{i'} \rangle \equiv \mathbf{s}^I, \tag{3.30}$$

one finds that

$$\mathcal{S}^I = N^I \mathbf{s}^I. \tag{3.31}$$

This is the semiclassical approach.

Some computations

I will now compute the terms $[\mathbf{s}_l, \mathbf{s}_i \cdot \mathbf{s}_j]$ and $[\mathbf{s}, \kappa_1 (s^x)^2 + \kappa_2 (s^z)^2]$ of (3.27). The former gives

$$\begin{aligned}
[\mathbf{s}_l, \mathbf{s}_i \cdot \mathbf{s}_j] &= [s_l^\alpha, s_i^\beta s_j^\beta] && (3.32)\\
&= [s_l^\alpha, s_i^\beta] s_j^\beta + s_i^\beta [s_l^\alpha, s_j^\beta] && (3.33)\\
&= i\delta^{li} \varepsilon^{\alpha\beta\gamma} s_i^\gamma s_j^\beta + s_i^\beta i\delta^{lj} \varepsilon^{\alpha\beta\gamma} s_j^\gamma && (3.34)\\
&= -i\delta^{li} \varepsilon^{\alpha\gamma\beta} s_i^\gamma s_j^\beta + i\delta^{lj} \varepsilon^{\alpha\beta\gamma} s_i^\beta s_j^\gamma && (3.35)\\
&= -i\delta^{li} \mathbf{s}_i \times \mathbf{s}_j + i\delta^{lj} \mathbf{s}_i \times \mathbf{s}_j && (3.36)\\
[\mathbf{s}_l, \mathbf{s}_i \cdot \mathbf{s}_j] &= i(-\delta^{li} + \delta^{lj})\ \mathbf{s}_i \times \mathbf{s}_j. && (3.37)
\end{aligned}$$

Using the Einstein summation convention, products of repeated indices are summed. For example, $s_i^\beta s_j^\beta = \sum_\beta s_i^\beta s_j^\beta$. The totally antisymmetric symbol (the Levi-Civata tensor) ε^{kij} is a fancy but practical way of writing the cross product. For example, $\varepsilon^{\alpha\beta\gamma} s_i^\beta s_j^\gamma = \mathbf{s}_i \times \mathbf{s}_j$.

Notice that upon taking the expectation value and identifying coordinates of spins of each sublattice, the intra-sublattice terms of (3.37) are zero: Suppose i and $j = i'$ are contained in the same sublattice, then

$$\langle \mathbf{s}_i \times \mathbf{s}_{i'} \rangle \quad = \quad \mathbf{s}^I \times \mathbf{s}^I = 0. \tag{3.38}$$

Defining $\mathbf{a}$ by

$$a^\alpha = \delta^{\alpha\mu}\kappa_\mu s^\alpha, \quad \alpha \in \{x, y, z\} \text{ and } \mu \in \{1, 2\}, \tag{3.39}$$

the anisotropy term then gives

$$\begin{aligned}
[\mathbf{s}, -\kappa_1(s^x)^2 - \kappa_2(s^z)^2] &= -[s^\alpha, a^\beta s^\beta] && (3.40)\\
&= -\delta^{\beta\mu}\kappa^\mu[s^\alpha, s^\beta s^\beta] && (3.41)\\
&= -\delta^{\beta\mu}\kappa^\mu([s^\alpha, s^\beta]s^\beta + s^\beta[s^\alpha, s^\beta]) && (3.42)\\
&= -i\delta^{\beta\mu}\kappa^\mu(\varepsilon^{\alpha\beta\gamma}s^\gamma s^\beta + s^\beta\varepsilon^{\alpha\beta\gamma}s^\gamma) && (3.43)\\
&= i(\varepsilon^{\alpha\gamma\beta}s^\gamma a^\beta - \varepsilon^{\alpha\beta\gamma}a^\beta s^\gamma) && (3.44)\\
[\mathbf{s}, -\kappa_1(s^x)^2 - \kappa_2(s^z)^2] &= i(\mathbf{s} \times \mathbf{a} - \mathbf{a} \times \mathbf{s}). && (3.45)
\end{aligned}$$

where the identity $[A, BC] = [A, B]C + B[A, C]$ has been used. Taking the expectation value, (3.45) is:

$$[\mathbf{s}^I, -\kappa_1(s_I^x)^2 - \kappa_2(s_I^z)^2] \quad = \quad 2i\ \mathbf{s} \times \mathbf{a} \tag{3.46}$$

3.2.1 Equation of motion for the collective modes

Using (3.37) and (3.45), the equation of motion (3.27) can be evaluated. From (3.38) it can be seen that intra-sublattice terms are zero. This is consistent with the result in section 3.1 in which intra-sublattice terms also did not contribute to dynamics. It is therefore enough to let $l, i \in I^I$ be the

index of one sublattice and $j \in I^J$ the index of the other.

$$\hbar\frac{\partial \mathbf{S}^I}{\partial t} = \frac{1}{i}[\mathbf{S}^I, H] \tag{3.47}$$

$$= \frac{1}{i}[\sum_l \mathbf{s}_l, H] \tag{3.48}$$

$$= \frac{1}{i}[\sum_l \mathbf{s}_l, \sum_{ij} J_{ij}\mathbf{s}_i \cdot \mathbf{s}_j] + \frac{1}{i}[\sum_l \mathbf{s}_l, \sum_i (-\kappa_1 (s_i^x)^2 - \kappa_2 (s_i^z)^2)] \tag{3.49}$$

$$= -\sum_{lij} (\delta_{il} J_{ij}\mathbf{s}_i \times \mathbf{s}_j) + 2\sum_l \mathbf{s}_l \times \mathbf{a}(\mathbf{s}_l) \tag{3.50}$$

$$= -\sum_{ij} J_{ij}\mathbf{s}_i \times \mathbf{s}_j + 2N^I \mathbf{s}^I \times \mathbf{a}^I \tag{3.51}$$

$$= -N^I J(0)^I_{\mathrm{av}} \mathbf{s}^I \times \mathbf{s}^J + 2\mathcal{S}^I \times \mathbf{a}^I \tag{3.52}$$

$$\hbar\frac{\partial \mathcal{S}^I}{\partial t} = -J(0)^I_{\mathrm{av}} \mathcal{S}^I \times \mathbf{s}^J + 2\mathcal{S}^I \times \mathbf{a}^I \tag{3.53}$$

where the CPA 3.13 was used in writing

$$\sum_{ij} J_{ij}\mathbf{s}_i \times \mathbf{s}_j = N^I J(0)^I_{\mathrm{av}} \mathbf{s}^I \times \mathbf{s}^J. \tag{3.54}$$

Equation (3.53) can be rewritten in macroscopic units. We know from magnetism [3], that the connection between the spin of an electron and it's magnetic moment is $|m| = |g\mu_B S|$ where S is the semiclassical size of the spins, $S = \sqrt{\frac{5}{2}(\frac{5}{2}+1)}$. Thus the unit submagnetizations $\mathbf{m}^I$ are connected to the macrospins by the equation

$$\mathbf{S}^I = N^I \mathbf{s}^I = -\frac{N^I S}{g\mu_B}\mathbf{m}^I. \tag{3.55}$$

The unit of $\mathbf{m}^I$ is then $g\mu_B$. The fictitious interaction fields (3.19) and (3.20) are redefined as

$$B_X^I = \frac{|J(0)^I_{\mathrm{av}}|S}{g\mu_B} \tag{3.56}$$

and

$$B_{\kappa_i} = \frac{|\kappa_i|S}{g\mu_B}. \tag{3.57}$$

In comparing to the spinwave energies to ressonance frequencies, this altered definition must be kept in mind.

Inserting (3.55), (3.56) and (3.57) into (3.53) one finds

$$\left(\frac{-SN^I}{g\mu_B}\right)\hbar\frac{\partial \mathbf{m}^I}{\partial t} = -\left(\frac{-SN^I}{g\mu_B}\right)\left(\frac{-\mathcal{J}(0)^I_{\rm av}S}{g\mu_B}\right)\mathbf{m}^I\times\mathbf{m}^J + 2\left(\frac{-SN^I}{g\mu_B}\right)\mathbf{m}^I\times\begin{pmatrix}\frac{-\kappa_1 S}{g\mu_B}\,m_x^I\\ 0\\ \frac{-\kappa_2 S}{g\mu_B}\,m_z^I\end{pmatrix}. \quad (3.58)$$

This is rewritten as

$$\frac{\partial \mathbf{m}^I}{\partial t} = -\frac{g\mu_B}{\hbar}\left(-\frac{1}{g\mu_B}B_X^I\mathbf{m}^I\times\mathbf{m}^J+\frac{2}{g\mu_B}\mathbf{m}^I\times\begin{pmatrix}B_{\kappa_1}m_x^I\\ 0\\ B_{\kappa_2}m_z^I\end{pmatrix}\right). \quad (3.59)$$

and the effective equation of motion is

$$\frac{\partial \mathbf{m}^I}{\partial t} = \gamma\mathbf{m}^I\times\mathbf{B}^I_{\rm eff} \quad (3.60)$$

where

$$\gamma = -\frac{g\mu_B}{\hbar} \quad (3.61)$$

is the gyromagnetic ratio of the electron.

The effective field $\mathbf{B}^I_{\rm eff}$ is given by (3.59) and depends on the submagnetizations:

$$\mathbf{B}^I_{\rm eff} = -\frac{1}{g\mu_B}B_X^I\mathbf{m}^J+\frac{2}{g\mu_B}\begin{pmatrix}B_{\kappa_1}m_x^I\\ 0\\ B_{\kappa_2}m_z^I\end{pmatrix}. \quad (3.62)$$

The equation of motion (3.60) has the well-known form that describes precession of a magnetic moment in a field. Such equations are used in many applications of magnetism, for example in NMR, ESR, μSR, etc. It describes simple Larmor precession. Notice that the resulting equation of motion is strictly classical. All quantum mechanical effects are contained in the constants B_X, B_1, B_2, and in the form of the effective field $\mathbf{B}^I_{\rm eff}$. The

equation of motion is quadratic in the magnetic moment $\mathbf{m}^I$, so the effect of anisotropies and exchange are described by two coupled, nonlinear first order differential equations. This also means that the system is non-inertial.

Notice that the equation of motion does not depend on particle size. This is because each site is equivalently coupled with a few neighbours on the other sublattice (in the CPA). Simple Larmor precession has the same feature: the Larmor frequency ($f_L = \gamma B$) does not depend on the size of the moment. In order to get a physically realistic model, extensive parameters such as N, T or the magnetic energy E must be brought into play. The first step is to calculate the magnetic energy.

3.2.2 Magnetic energy

The task at hand is to rewrite the Hamiltonian into a function of the sub-magnetizations.

We need only consider that part of the Hamiltonian in which i belongs to sublattice A and j to sublattice B. The intra-sublattice term in the exchange sum reduces to a constant when the semiclassical coordinates of all spins on the same sublattice are identified, because:

$$J_{ii'}\mathbf{s}_i \cdot \mathbf{s}_j \rightarrow J_{ii'}\mathbf{s}^I \cdot \mathbf{s}^I = \text{constant}. \tag{3.63}$$

These terms can therefore be disregarded, as above.

The anisotropy terms are easy to convert to macroscopic units. These are

$$\begin{aligned} H_{\text{anis}} &= -\kappa_1 \sum_{ij} \left((s_i^x)^2 + (s_j^x)^2 \right) - \kappa_2 \sum_{ij} \left((s_i^z)^2 + (s_j^z)^2 \right) \\ &= N^A \mathbf{s}^A \cdot \begin{pmatrix} \kappa_1 s_x^A \\ 0 \\ \kappa_2 s_z^A \end{pmatrix} + N^B \mathbf{s}^B \cdot \begin{pmatrix} \kappa_1 s_x^B \\ 0 \\ \kappa_2 s_z^B \end{pmatrix}. \end{aligned} \tag{3.64}$$

The expression for the exchange energy term is

$$H_{\text{ex}} = \sum_{ij} J_{ij}\mathbf{s}_i \cdot \mathbf{s}_j. \tag{3.65}$$

This sum is more difficult to handle because the local environment of a site depends on position in the particle, but this was taken care of by the CPA. Approximating, the sum can be written in terms of sublattice A or B as

$$\sum_{ij} J_{ij}\mathbf{s}_i \cdot \mathbf{s}_j = N^A J(0)^A_{\text{av}}\ \mathbf{s}^A \cdot \mathbf{s}^B \tag{3.66}$$

$$= N^B J(0)^B_{\text{av}}\ \mathbf{s}^A \cdot \mathbf{s}^B \tag{3.67}$$

This is because the total energy is the sum of the energy of all inter-sublattice bonds, and not affected by the coherent potential approximation, i.e. $N^I J(0)^I_{\text{av}} = JK$ which is a constant. However, the dynamical properties of the Hamiltonian *do* depend on the coherent potential $J(0)^I_{\text{av}}$, since it is included in the equation of motion (3.60).

The total energy is

$$E = N^I J(0)^I_{\text{av}}\ \mathbf{s}^A \cdot \mathbf{s}^B - N^A \mathbf{s}^A \cdot \begin{pmatrix} \kappa_1 s_x^A \\ 0 \\ \kappa_2 s_z^A \end{pmatrix} - N^B \mathbf{s}^B \cdot \begin{pmatrix} \kappa_1 s_x^B \\ 0 \\ \kappa_2 s_z^B \end{pmatrix} \tag{3.68}$$

$$= \left(\frac{s}{g\mu_B}\right)\left(\left(\frac{J(0)^I_{\text{av}} s}{g\mu_B}\right)\ N^I \mathbf{m}^A \cdot \mathbf{m}^B \right.$$
$$\left. -N^A \mathbf{m}^A \cdot \begin{pmatrix} \left(\frac{\kappa_1 s}{g\mu_B}\right) m_x^A \\ 0 \\ \left(\frac{\kappa_2 s}{g\mu_B}\right) m_z^A \end{pmatrix} - N^B \mathbf{m}^B \cdot \begin{pmatrix} \left(\frac{\kappa_1 s}{g\mu_B}\right) m_x^B \\ 0 \\ \left(\frac{\kappa_2 s}{g\mu_B}\right) m_z^B \end{pmatrix}\right) \tag{3.69}$$

$$E = \left(\frac{s}{g\mu_B}\right)\left(B_X^I\ N^I \mathbf{m}^A \cdot \mathbf{m}^B - N^A \mathbf{m}^A \cdot \begin{pmatrix} B_{\kappa_1} m_x^A \\ 0 \\ B_{\kappa_2} m_z^A \end{pmatrix} - N^B \mathbf{m}^B \cdot \begin{pmatrix} B_{\kappa_1} m_x^B \\ 0 \\ B_{\kappa_2} m_z^B \end{pmatrix}\right). \tag{3.70}$$

Temperature is related to changes in internal energy, so this expression

for the total magnetic energy is required in the next section when the system is coupled to a generic heat bath.

3.3 Thermal distribution of collective states

In order to model physically realistic state distributions at a given temperature, the system is coupled to a heat bath. This is done using Langevin dynamics.

The statistical model for microscopic interactions

Thermal interactions have microscopic origins which are realized by phonons and higher spinwave modes in the nanoparticle, and magnetic fields from the surrounding environment. However a highly complicated precise microscopic model is hardly manageable. Instead it is possible to write down a very simple phenomenological equation for fluctuation and dissipation. This is called a Langevin equation. Although the microscopic interactions are in principle deterministic on a very short time scale, they are also unknown, and essentially random. Therefore the fluctuation (or excitation) term of the Langevin equation is a randomly fluctuating force. Dissipation is modelled by a deterministic frictional term.

Statistical mechanics is used to make sure that the effects of the random variable and the frictional term balance out in equilibrium with a physical heat bath of temperature T. The exact connection between temperature, fluctuations and dissipation will be derived.

This approach is called Langevin dynamics, and is related to Brownian motion and random walks. The reader is referred to the book "Brownian motion – Fluctuation, Dynamics and Applications" by Mazo [30] and especially to the superparamagnetic theory paper by Brown [19]. The papers by Garcia-Palacios [27] and Würger [25] were used for inspiration.

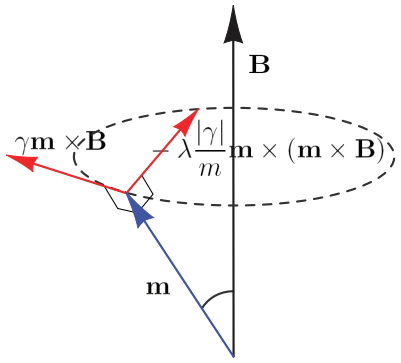

Figure 3.2: *Illustration of the deterministic parts of the Langevin equation.*

3.3.1 The Langevin equation

Consider the physical system of a magnetic moment in a constant field $\mathbf{B}$. The isolated system is described by an equation of the same form as the equation of motion (3.60):

$$\frac{\partial \mathbf{m}}{\partial t} = \gamma \mathbf{m} \times \mathbf{B}. \tag{3.71}$$

Submerging the system in a heat bath, energy can flow to and from the system in small quantities.

The flow of energy away from the system is dissipation and can be thought of as the magnetic parallel to friction. Energy is expected to deplete at a rate proportional to the "velocity" times a frictional constant λ, and towards the minimum energy configuration. Thus the size of the frictional terms should be $\lambda|\frac{\partial \mathbf{m}}{\partial t}|$. At the minimum energy configuration, $\mathbf{m}$ and $\mathbf{B}$ are parallel. Thus the direction of the frictional term is $\pm\mathbf{m}\times\frac{\partial \mathbf{m}}{\partial t}$ where the sign depends on the direction of $\frac{\partial \mathbf{m}}{\partial t}$. See fig. 3.2 for a sketch of this. λ should be independent on temperature: Each small amount of energy that dissipates away from the system, is absorped by an energy level of the physical heat bath. These receiving levels should be independent on temperature.

The flow of energy into the system causes small perturbations to the trajectory of $\mathbf{m}$. For a perturbation at time t, let $\mathbf{b}(t)$ denote the corre-

sponding fictitious field. The effect of excitations is then treated as a highly time-dependent field $\mathbf{b}$.

The particular Langevin equation is

$$\frac{\partial \mathbf{m}}{\partial t} = \gamma \mathbf{m} \times (\mathbf{B} + \mathbf{b}) \pm \lambda \frac{1}{m} \mathbf{m} \times \frac{\partial \mathbf{m}}{\partial t}. \tag{3.72}$$

where $\pm$ refers to the sign of γ. For consistency of units the frictional term is divided by the size m of the moment. Expanding in one iteration of $\frac{\partial \mathbf{m}}{\partial t}$

$$\frac{\partial \mathbf{m}}{\partial t} = \gamma \mathbf{m} \times (\mathbf{B} + \mathbf{b}) \pm \lambda \frac{1}{m} \mathbf{m} \times \left(\gamma \mathbf{m} \times (\mathbf{B} + \mathbf{b}) \pm \lambda \frac{1}{m} \mathbf{m} \times \frac{\partial \mathbf{m}}{\partial t} \right) \tag{3.73}$$

and removing second order terms in λ, this becomes the stochastic Landau-Lifschitz equation:

$$\frac{\partial \mathbf{m}}{\partial t} \cong \gamma \mathbf{m} \times (\mathbf{B} + \mathbf{b}) - \lambda \frac{|\gamma|}{m} \mathbf{m} \times (\mathbf{m} \times \mathbf{B}). \tag{3.74}$$

This supposes that $\lambda \ll 1$, i.e. that the system is weakly damped. This equation was also used in [19]. In component notation (3.74) is

$$\frac{\partial m_i}{\partial t} = \gamma \left(\varepsilon^{kij} (B_k + b_k) - \lambda \frac{|\gamma|}{m} \varepsilon^{kij} \varepsilon^{kmn} m_m \, B_n \right) m_j. \tag{3.75}$$

The statistical properties of the fluctuating field $\mathbf{b}$ must correspond to those of a physical heat bath. The fluctuations are expected to be uncorrelated in time, isotropic, and follow a Gaussian distribution. The fluctuations are deviations from the average field $\mathbf{B}$ so they have zero mean:

$$< b_i(t) > = 0 \tag{3.76}$$

Furthermore, the thermal "amplitude" of the field should be related to the frictional constant and the temperature. These requirements are satisfied by the correlation function

$$< b_i(t) b_j(t') > = A \delta_{ij} \delta(t - t') \tag{3.77}$$

where the diffusion constant is given by the Einstein relation

$$A = 2\frac{\lambda}{|\gamma|m}k_B T. \tag{3.78}$$

The notation $< ... >$ denotes an average of all microscopic realizations of $\mathbf{b}$, or thermal average. The form of the correlation function (3.78) implies that the fluctuation amplitude increases with temperature and decreases with m, which can be thought of as the "weight" of the magnetic moment. The temperature is given by the fraction of the average fluctuation amplitude and the frictional constant:

$$T \sim \frac{< b^2 >}{\lambda}. \tag{3.79}$$

This means that λ can be thought of as the strenght of the thermal coupling: If dissipation increases, then so do the fluctuations such that T stays the same.

An equation such as (3.78) was first derived by Einstein [31] for a fine particle submerged in a liquid. Hence the name "Einstein relation". See the book "Brownian Motion – Fluctuation, Dynamics and Applications" by Mazo [30] for a thorough description of the statistical models and their relevance in many areas of physics.

Generalization to the nanoparticle submagnetization system

The Langevin equation of the nanoparticle system is very similar to (3.74). Instead of one equation describing the motion of a single magnetic moment, there are two equations – one for each submagnetization. Instead of the constant magnetic field, the effective field (3.62) is used. The Langevin equation for each submagnetization then reads

$$\frac{\partial \mathbf{m}^I}{\partial t} = \gamma \mathbf{m}^I \times \left(\mathbf{B}^I_{\text{eff}} + \mathbf{b}^I\right) - \lambda \frac{|\gamma|}{m}\mathbf{m}^I \times \mathbf{m}^I \times \mathbf{B}^I_{\text{eff}} \tag{3.80}$$

where

$$\mathbf{B}^I_{\text{eff}} = -\frac{1}{g\mu_B}B^I_X\mathbf{m}^J + \frac{2}{g\mu_B}\begin{pmatrix} B_{\kappa_1}m^I_x \\ 0 \\ B_{\kappa_2}m^I_z \end{pmatrix}. \tag{3.81}$$

Recall that for convenience the submagnetization moments have unit length such that $m = g\mu_B$.

The statistical properties of $\mathbf{b}^I$ are as above with the exception that the diffusion constant A^I depends on the size of sublattice I. The next section is a proof that

$$A^I = 2\frac{\lambda}{|\gamma|g\mu_B sN^I}k_BT \tag{3.82}$$

$$= 2\frac{\lambda}{|\gamma|M^I}k_BT. \tag{3.83}$$

where M^I is the size of sublattice I.

3.3.2 Probability current

In the probabilistic world of fluctuation and dissipation, time evolution of physical systems is not deterministic and most be described by probability distributions. The probability distribution of a system depends on time and space coordinates, and is described by a differential equation known as the Fokker-Planck equation. The Fokker-Planck equation for magnetic systems is usually found from general expressions. See for example [19] where Brown finds a solution to the ferromagnetic Fokker-Planck equation and reaches the Nëel-Brown law 2.10 in the low-temperature limit. The corresponding Fokker-Planck equation for an antiferromagnet has never been solved.

However I will not go the Fokker-Planck way around proving 3.141, but do it in a more straightforward and more intuitive way. The result is a general expression for the probability current of a physical system described by a generalized Langevin equation. This equation of motion is written as

$$\frac{\partial x_i}{\partial t} = H_i(x) + f_i(x) \tag{3.84}$$

where H_i is a deterministic and f_i is a random term. Many examples of systems governed by such an equation are found in [30].

Let $p(x_t) = p$ be the probability distribution of a physical system having the configuration x at time t. In this formulation x and t are considered independent parameters of p. Yet $p(x_t)$ is linked to $p(y_{t-\Delta t})$ since the equation of motion dictates that only a few choices of y's will indeed evolve into x from $t - \Delta t$ to t. The probability current is defined as

$$J_i = p < v_i > \tag{3.85}$$

where v is the first time derivative of x, but considered an independent parameter as in the Hamiltonian formulation of classical mechanics [32]. Integrate over the entire phase space of v at time t to determine the thermal average value $< v >$:

$$< v_i > = \int dv\ v_i p(v_t) \tag{3.86}$$

$$= \int dv\ v_i p(v_t|x_t) \tag{3.87}$$

where the conditional probability $p(v_t|x_t)$ depends on x at time $t - \Delta t$, and at time $t + \Delta t$. However, this time evolution is probabilistic and should be expressed in terms of conditional probabilities. Now assume that it is OK to write the velocity as a difference quotient, and then take the limit $\Delta t \to 0$ *after* integrating[b]. Continue with

$$< v_i >= \int dv\ v_i \int dy \int dz\ \delta\left(v_i - \frac{(z_{t+\Delta t} - y_{t-\Delta t})_i}{2\Delta t}\right) p(z_{t+\Delta t}|x_t) p(y_{t-\Delta t}|x_t). \tag{3.88}$$

This can be rewritten using Baye's rule for conditional probabilities $p(ab) =$

[b]The physical standpoint that x is "nice" applies.

$p(a|b)p(b) = p(b|a)p(a)$:

$$< v_i >= \int dy \int dz \; \frac{(z_{t+\Delta t} - y_{t-\Delta t})_i}{2\Delta t} p(z_{t+\Delta t}|x_t) \frac{p(x_t|y_{t-\Delta t})p(y_{t-\Delta t})}{p(x_t)} \quad (3.89)$$

Multiplying this by $p(x)$, the probability current density

$$J_i = p(x) < v_i > \quad (3.90)$$

appears on the left hand side. Omitting the t-subscripts,

$$J_i = \int dy \int dz \; \frac{(z-x)_i + (x-y)_i}{2\Delta t} p(z|x)p(x|y)p(y). \quad (3.91)$$

Rewriting:

$$J_i = \left(\int dy \int dz \; \frac{(z-x)_i}{2\Delta t} p(z|x)p(x|y) + \int dy \int dz \; \frac{(x-y)_i}{2\Delta t} p(z|x)p(x|y) \right) p(y) \quad (3.92)$$

$$= \int dz \; \frac{(z-x)_i}{2\Delta t} p(z|x) \int dy \; p(x|y)p(y) + \int dy \; \frac{(x-y)_i}{2\Delta t} p(x|y)p(y) \int dz \; p(z|x) \quad (3.93)$$

$$= \int dz \; \frac{(z-x)_i}{2\Delta t} p(z|x)p(x) + \int dy \; \frac{(x-y)_i}{2\Delta t} p(x|y)p(y) \quad (3.94)$$

Expanding $p(y) = p(x + (y-x))$ to first order in $(y-x)$;

$$p(x + (y-x)) \cong p(x) + (y-x)_j \frac{\partial p}{\partial x_j} \quad (3.95)$$

the current density becomes

$$J_i = \left(\int dz \; \frac{(z-x)_i}{2\Delta t} p(z|x) \right) p(x) + \left(\int dy \; \frac{(x-y)_i}{2\Delta t} p(x|y) \right) \left(p(x) + (y-x)_j \frac{\partial p}{\partial x_j} \right). \quad (3.96)$$

Rearranging factors according to pre-factors to p and $\frac{\partial p}{\partial x_j}$:

$$J_i = \left(\int dz \; \frac{(z-x)_i}{2\Delta t} p(z|x) + \int dy \; \frac{(x-y)_i}{2\Delta t} p(x|y) \right) p(x) - \left(\int dy \; \frac{(x-y)_i (x-y)_j}{2\Delta t} p(x|y) \right) \frac{\partial p}{\partial x_j}. \quad (3.97)$$

The conditional probabilities in equation (3.97) can be evaluated. Given x at time t, and given a history or "realization" of the fluctuating force, the equation of motion (3.84) is deterministic and dictates that the system evolves into $x + \Delta x$ at time $t + \Delta t$. Then $p(x|y)$ in (3.97) is a δ-function centered around $x+\Delta x$. However, since the history of the random term is in fact probabilistic, $p(x|y)$ and $p(z|x)$ are thermal averages of δ-functions centered around the outcomes $x+\Delta x$ of the various histories of the fluctuating force:

$$\int dz\ \frac{(z-x)_i}{\Delta t} p(z|x) = \int dz\ \frac{(z-x)_i}{\Delta t} < \delta(z-(x+\Delta x)) > \quad (3.98)$$

$$= \frac{<\Delta x_i>}{\Delta t} \quad (3.99)$$

$$\int dy\ \frac{(x-y)_i}{\Delta t} p(x|y) = \int dy\ \frac{(x-y)_i}{\Delta t} < \delta(x-(y+\Delta y)) > \quad (3.100)$$

$$= \int dy\ \frac{(x-y)_i}{\Delta t} < \delta(x-U(\Delta t)y) > \quad (3.101)$$

$$= \frac{1}{|\frac{\partial U}{\partial y}|} \int d\left(U(\Delta t)y\right)\ \frac{(x-y)_i}{\Delta t} < \delta(x-U(\Delta t)y) > \quad (3.102)$$

$$= < \frac{1}{|\frac{\partial U}{\partial y}|} \frac{\Delta x_i}{\Delta t} > \quad (3.103)$$

$$= \frac{<\Delta x_i>}{\Delta t} \quad (3.104)$$

since $\frac{1}{|\frac{\partial U}{\partial y}|} \sim 1 + \mathcal{O}(\Delta t)$. $U(\Delta t)y = (y + \Delta y)$ denotes time evolution. Terms or order $(\Delta t)^2$ and higher are disregarded, since J_i only depends on first order terms. Those of zero thermal average are also discarded.

The pre-factor of the diffusion term becomes

$$\int dy\ \frac{(x-y)_i(x-y)_j}{\Delta t} p(x|y) = \int dy\ \frac{(x-y)_i(x-y)_j}{\Delta t} < \delta(x-U(\Delta t)y) >$$

$$= ...$$

$$= \frac{<\Delta x_i \Delta x_j>}{\Delta t}, \quad (3.105)$$

where I have again discarded irrelevant terms. Finally a simple yet general

expression is reached:

$$J_i = \frac{<\Delta x_i>}{\Delta t}p(x) - \frac{1}{2}\frac{<\Delta x_i \Delta x_j>}{\Delta t}\frac{\partial p}{\partial x_j} \quad \text{for} \quad \Delta t \to 0. \quad (3.106)$$

This expression for the current illustrates the roles of the deterministic and fluctuation forces:

Current is in general due to drift and diffusion. Drift is due to the deterministic part of the equation of motion (3.84) and as time evolves, drift should not change the shape of p. Therefore the pre-factor $\frac{<\Delta x_i>}{\Delta t}$ of p in (3.106) is the drift term.

Diffusion (or probability diffusion) is due to the random forces. As time goes on, diffusion tends to expand the probability density. Therefore the pre-factor $-\frac{1}{2}\frac{<\Delta x_i \Delta x_j>}{\Delta t}$ of the gradient $\frac{\partial p}{\partial x_j}$ is the diffusion term. Notice that if the fluctuating force in (3.84) is zero ($f_i = 0$), then $< \Delta x_i \Delta x_j >$ is in the order of Δt^2 and the diffusion term vanishes.

The factors $< \Delta x_i >$ and $< \Delta x_i \Delta x_j >$ can be determined from the specifics of the system.

Inserting the equation of motion

Integrate the general Langevin Equation (3.84) over a short time interval $[t, t + \Delta t]$:

$$\Delta x_i = \int_t^{t+\Delta t} dt' \frac{\partial x_i}{\partial t'} \quad (3.107)$$

$$= \int_t^{t+\Delta t} dt' H_i + \int_t^{t+\Delta t} dt' f_i \quad (3.108)$$

$$= H_i(x(t))\Delta t + \int_t^{t+\Delta t} dt' f_i \quad (3.109)$$

from which follows,

$$\Delta x_i \Delta x_j = \int_t^{t+\Delta t} dt' \int_t^{t+\Delta t} dt'' f_i(t') f_j(t'') \quad (3.110)$$

where I have only included the term of order f^2 as this is the only non-vanishing term, as above. Taking the thermal average,

$$< \Delta x_i > = H_i(x(t))\Delta t \tag{3.111}$$

$$= H_i \Delta t \tag{3.112}$$

and

$$< \Delta x_i \Delta x_j > = \int_t^{t+\Delta t} dt' \int_t^{t+\Delta t} dt'' < f_i(t') f_j(t'') > . \tag{3.113}$$

An advantage of this general approach is that it is now clear that the non-linearity of the effective field (3.81) does not affect the expression (3.106) for the current density.

Probability current of magnetic systems

Returning to the system of a single magnetic moment (3.74), the explicit expressions are

$$< \Delta m_i \Delta m_j > = \int_t^{t+\Delta t} dt' \int_t^{t+\Delta t} dt'' < f_i(t') f_j(t'') > \tag{3.114}$$

$$= \int dt' \int dt'' \varepsilon^{kil} \varepsilon^{k'jl'} \gamma^2 < b_k b_{k'} > m_l m_{l'} \tag{3.115}$$

$$= \int dt' \int dt'' \varepsilon^{kil} \varepsilon^{k'jl'} \gamma^2 A \delta^{kk'} \delta(t'-t'') m_l m_{l'} \tag{3.116}$$

$$= \gamma^2 A \Delta t \ \delta^{kk'} \ \varepsilon^{kil} \varepsilon^{k'jl'} \ m_l m_{l'} \tag{3.117}$$

$$= \gamma^2 A \Delta t \ (\delta^{ij} \delta^{ll'} - \delta^{il'} \delta^{lj}) m_l m_{l'} \tag{3.118}$$

$$= \gamma^2 A \Delta t \ (\delta^{ij} m_k m_k - m_i m_j) \tag{3.119}$$

and

$$< \Delta m_i > = H_i \Delta t \tag{3.120}$$

$$= \gamma \left(\varepsilon^{kij} B_k - \lambda \frac{|\gamma|}{m} \varepsilon^{kij} \varepsilon^{kmn} m_m \ B_n \right) m_j. \tag{3.121}$$

The expression for the current density becomes

$$J_i = H_i \ p - \frac{1}{2} \gamma^2 A \left(\delta^{ij} m_k m_k - m_i m_j \right) \frac{\partial p}{\partial m_j} \tag{3.122}$$

$$= H_i \ p - \frac{1}{2} \gamma^2 A \left(\frac{\partial p}{\partial m_i} m^2 - m_i m_j \frac{\partial p}{\partial m_j} \right). \tag{3.123}$$

Working on the diffusion term in vector notation,

$$\mathbf{J} = \mathbf{H}\, p - \frac{1}{2}\gamma^2 A \left(\frac{\partial p}{\partial \mathbf{m}} m^2 - (\mathbf{m} \cdot \frac{\partial p}{\partial \mathbf{m}})\mathbf{m} \right) p \tag{3.124}$$

$$= \mathbf{H}\, p + \frac{1}{2}\gamma^2 A \left(\mathbf{m} \times \mathbf{m} \times \frac{\partial p}{\partial \mathbf{m}} \right) \tag{3.125}$$

by the rule $a \times b \times c = b(a \cdot c) - c(a \cdot b)$. The final expression for the probability current is

$$\mathbf{J} = \left(\gamma \mathbf{m} \times \mathbf{B} - \lambda \frac{|\gamma|}{m} \mathbf{m} \times \mathbf{m} \times \mathbf{B} \right) p + \frac{1}{2}\gamma^2 A\, \mathbf{m} \times \mathbf{m} \times \frac{\partial p}{\partial \mathbf{m}}. \tag{3.126}$$

The probability current for the nanoparticle system (3.80) is reached by simply entering sublattice indices on $\mathbf{J}$, $\mathbf{M}$ and $\mathbf{B}$ in (3.126):

$$\mathbf{J}^I = \left(\gamma \mathbf{m}^I \times \mathbf{B}^I_{\text{eff}} - \lambda \frac{|\gamma|}{m} \mathbf{m}^I \times \mathbf{m}^I \times \mathbf{B}^I_{\text{eff}} \right) p + \frac{1}{2}\gamma^2 A\, \mathbf{m}^I \times \mathbf{m}^I \times \frac{\partial p}{\partial \mathbf{m}^I}. \tag{3.127}$$

3.3.3 Thermal equilibrium expressions

Consider the expression for the probability current, (3.126) or (3.127). The term proportional to λ is the frictional or dissipative term, as explained above. It depletes energy from the system. The term proportional to A is the diffusion term, due to energy flow into the system. When the energy flows into and out of a system are equal, on average, the system is said to be in thermal equilibrium. Then the current reduces to

$$\mathbf{J} = \gamma \mathbf{m} \times \mathbf{B}. \tag{3.128}$$

In thermal equilibrium it is known from statistical mechanics that p must be the Gibbs distribution:

$$p = \frac{1}{Z} \exp(-\beta E) \tag{3.129}$$

p is therefore independent on time. Thus, the continuity equation expressing conservation of probability density

$$\frac{\partial p}{\partial t} + \nabla \cdot \mathbf{J} = 0 \tag{3.130}$$

simply becomes

$$\nabla \cdot \mathbf{J} = 0. \tag{3.131}$$

When the dissipative and diffusive terms become equal in thermal equilibrium, the divergence of the current (3.128) indeed vanishes:

$$\nabla \cdot \mathbf{J} = \gamma \ \nabla \cdot (\mathbf{m} \times \mathbf{B}) = \gamma \ \frac{\partial}{\partial m_i}(\varepsilon^{kij} B_k m_j) = 0. \tag{3.132}$$

I will now determine the condition for thermal equilibrium. Equating the frictional and diffusion terms one finds that

$$\lambda \frac{|\gamma|}{m} \mathbf{B} \ p \ = \ \frac{1}{2}\gamma^2 A \frac{\partial p}{\partial \mathbf{m}}. \tag{3.133}$$

From (3.129) it follows that

$$\frac{\partial p}{\partial \mathbf{m}} = -\beta \frac{\partial E}{\partial \mathbf{m}} \ p \tag{3.134}$$

which leads to the following thermal equilibrium condition in terms of the energy:

$$\frac{\lambda}{m}\mathbf{B} \ = \ -\frac{1}{2}\beta|\gamma| A \frac{\partial E}{\partial \mathbf{m}}. \tag{3.135}$$

This relation is independent on representation, since the quantity $m\frac{\partial E}{\partial \mathbf{m}}$ is independent on the size of m.

A single magnetic moment

The energy of a single magnetic moment in a field is $E = -\mathbf{m} \cdot \mathbf{B}$, such that $\frac{\partial E}{\partial \mathbf{m}} = -\mathbf{B}$. (3.135) becomes the magnetic Einstein relation,

$$\frac{\lambda}{m} \ = \ \frac{1}{2}\beta|\gamma| A \tag{3.136}$$

$$A \ = \ 2\frac{\lambda}{|\gamma| m} k_B T. \tag{3.137}$$

Nanoparticle system

The energy of the coupled system was determined in section 3.2.2. It follows that

$$\frac{\partial E}{\partial \mathbf{m}^I} = sN^I \left(\frac{1}{g\mu_B} B_X^I \mathbf{m}^J - \frac{2}{g\mu_B} \begin{pmatrix} B_1 m_x^I \\ 0 \\ B_2 m_z^I \end{pmatrix} \right) \tag{3.138}$$

$$= -sN^I \, \mathbf{B}_{\text{eff}}^I. \tag{3.139}$$

The thermal equilibrium condition (3.135) for the coupled system becomes

$$\lambda \frac{|\gamma|}{g\mu_B} \mathbf{B}_{\text{eff}}^I = \frac{1}{2} \beta \gamma^2 A s N^I \, \mathbf{B}_{\text{eff}}^I$$

and thus the Einstein relation reads

$$A^I = 2 \frac{\lambda}{|\gamma| g\mu_B s N^I} k_B T \tag{3.140}$$

$$= 2 \frac{\lambda}{|\gamma| M^I} k_B T. \tag{3.141}$$

It is essential that particle size enters the Einstein relation (3.141). In chapter 2 I explained that the collective dynamics should depend drastically on particle size, as experiments indeed showed. In the probabilistic model, the fluctuating field amplitude increases with temperature and decreases with particle size, since $< \mathbf{b}^2 > \sim \frac{T}{N^I}$. Although the equation of motion (3.60) at first sight appears to be independent of the size of the submagnetizations (and these were therefore normalized to $m = g\mu_B$), larger particles experience precisely the same excitations as smaller particles, but at higher temperatures.

This means that the difference between collective dynamics in nanoparticles of different sizes primarily lies in the temperature scale. This is how the model accounts for the scaling of anisotropy barriers with particle size. Additionally the size dependencies of the anisotropy constants, and possibly exchange constants, is still present and any surface effects become more

important with decreasing particle size.

This concludes the theory chapter. Equation (3.80) describes thermal interactions with the classical antiferromagnetic nanoparticle system of two submagnetizations influenced by exchange and anisotropies. The next chapter concerns the numerical method that will be used to simulate submagnetization trajectories.

Chapter 4

Simulation

A numerical method for integrating the the Langevin equation of chapter 3 is developed in this chapter. The method is validated by comparing to known simple cases. All numerical integration and analysis was done using MATLAB v. 2007b. The most relevant code is found appendix B.

4.1 Implementation

I will now show how (3.80) is transformed into a form that can be readilly solved by a numerical integration algorithm.

The submagnetization vectors are for convenience normalized to length 1. The normalized submagnetizations are:

$$\hat{\mathbf{m}}^I = \frac{\mathbf{m}^I}{g\mu_B} \tag{4.1}$$

where $\mathbf{m}^I$ are the unit submagnetizations from chapter 3. In these units, the equation of motion is

$$\frac{\partial \hat{\mathbf{m}}^I}{\partial t} = \gamma \hat{\mathbf{m}}^I \times \left(\mathbf{B}^I_{\text{sim}} + \mathbf{b}^I\right) - \lambda|\gamma| \hat{\mathbf{m}}^I \times \hat{\mathbf{m}}^I \times \mathbf{B}^I_{\text{sim}} \tag{4.2}$$

and the effective field becomes

$$\mathbf{B}^I_{\text{sim}} \;=\; -\,B^I_X\hat{\mathbf{m}}^J + \,2\begin{pmatrix} B_{\kappa_1}\hat{m}^I_x \\ 0 \\ B_{\kappa_2}\hat{m}^I_z \end{pmatrix}. \tag{4.3}$$

The fluctuating field $\mathbf{b}^I$ satisfies

$$< b^I_i(t)b^I_j(t') > \;=\; 2\frac{\lambda}{|\gamma|g\mu_B s N^I}k_BT\delta_{ij}\delta(t-t'). \tag{4.4}$$

As this identity is independent on representation (see (3.135)), normalizing the submagnetizations did not change it.

Suppressing the fancy "hat" notation and the sublattice index (setting $\mathbf{m} = \hat{\mathbf{m}}^I$) the equation of motion will be written in shorthand notation as

$$\frac{\partial \mathbf{m}}{\partial t} \;=\; H(\mathbf{m}) + f(\mathbf{m}). \tag{4.5}$$

I approximate the continuous time parameter t by a sequence of equally spaced discrete points $\{t_i\}_{i=0}^{\infty}$. A discrete solution to (4.5) can be written formally as the integral from t_0 to t_N:

$$\mathbf{m}(t_N) - \mathbf{m}(t_0) = \int_{t_0}^{t_N} dt' \frac{\partial \mathbf{m}}{\partial t'} = \sum_{i=0}^{N-1}\int_{t_i}^{t_{i+1}} dt' \frac{\partial \mathbf{m}}{\partial t'} \tag{4.6}$$

Given initial conditions $\mathbf{m}(t_0)$, the first term in the sum on the right hand side of (4.6) can be approximated by $\Delta\mathbf{m}_0 \cong \int_{t_0}^{t_1} dt' \frac{\partial \mathbf{m}}{\partial t'}$. Then we can give the initial condition $\mathbf{m}(t_1) = \mathbf{m}(t_0) + \Delta\mathbf{m}_0$ for the second term in the sum, $\Delta\mathbf{m}_1 \cong \int_{t_1}^{t_2} dt' \frac{\partial \mathbf{m}}{\partial t'}$. This way an approximate solution can be determined by iteration of a discrete approximation algorithm. The problem at hand is to give a good approximation to the individual terms $\Delta\mathbf{m}_i$, in the limit where Δt is small, but not infinitesimal.

Short time integration

Integrating (4.5) from t_i to $t_{i+1} = t_i + \Delta t$:

$$\Delta\mathbf{m}_i = \int_{t_i}^{t_i+\Delta t} dt' H(\mathbf{m}) + \int_{t_i}^{t_i+\Delta t} dt' f(\mathbf{m}) \tag{4.7}$$

Since H is considered almost constant during Δt, it can be approximated by the average value $\mathbf{a}_i = \mathbf{a}_i(H)$ of H during Δt. Then the short time integral is given by a linear function in Δt,

$$\int_{t_i}^{t_i+\Delta t} dt' H(\mathbf{m}) \cong \Delta t \ \mathbf{a}_i. \tag{4.8}$$

The random term $\Delta\mathbf{f} = \int_{t_i}^{t_i+\Delta t} dt' f(\mathbf{m})$ is tricky to approximate since $\mathbf{b}$ is far from constant in the time scale of a numerical integration step. The random term is

$$\begin{aligned}
\Delta\mathbf{f} &= \int_{t_i}^{t_i+\Delta t} dt' \ \gamma\mathbf{m} \times \mathbf{b}(t') && (4.9)\\
&\cong \gamma\mathbf{m} \times \left(\int_{t_i}^{t_i+\Delta t} dt' \ \mathbf{b}(t') \right) && (4.10)\\
&= \gamma\mathbf{m} \times \Delta\mathbf{b}, && (4.11)
\end{aligned}$$

where $\Delta\mathbf{b} = \int_{t_i}^{t_i+\Delta t} dt' \mathbf{b}(t)$. Since $\mathbf{m}$ is almost constant in the interval it has been taken outside of the integral. Being the integral of $\mathbf{b}$, $\Delta\mathbf{b}$ is in principle the sum of a lot of random numbers of Gaussian distribution, and should be treated by the theory for random walk. Einstein showed in 1905 that the mean radius of a random walk in the absence of a potential scales as $\sqrt{t}$. This translates naively into the variance of the probability distribution being proportional to t, thus the numbers $\Delta\mathbf{b}$ should be Gaussian random numbers with variance equal to Δt. The reader is referred to the literature for a proof that $\Delta\mathbf{b}$ follows a Gaussian distribution [30]. The variance can be calculated from the correlation function:

$$\begin{aligned}
< \Delta b_i \Delta b_j > &= < \int_{t_i}^{t_i+\Delta t} dt' \ b_i(t') \int_{t_i}^{t_i+\Delta t} dt'' \ b_j(t'') > && (4.12)\\
&= \int_{t_i}^{t_i+\Delta t} \int_{t_i}^{t_i+\Delta t} dt' dt'' \ < b_i(t') b_j(t'') > && (4.13)\\
&= A\delta_{ij} \int_{t_i}^{t_i+\Delta t} \int_{t_i}^{t_i+\Delta t} dt' dt'' \ \delta(t'-t'') && (4.14)\\
&= \delta_{ij} A \int_{t_i}^{t_i+\Delta t} dt' && (4.15)\\
< \Delta b_i \Delta b_j > &= \Delta t \ A\delta_{ij}. && (4.16)
\end{aligned}$$

The resulting approximation to (4.7) is

$$\Delta \mathbf{m}_i = \Delta t \ \mathbf{a}_i + \gamma \mathbf{m}_i \times \Delta \mathbf{b}. \tag{4.17}$$

where an approximate value for $\mathbf{a}_i$ is determined below.

4.1.1 Numerical method

There are standard techniques to determining approximate solutions to deterministic differential equations. An example result of such an algorithm is shown in Fig. 4.1a. I will make use of a second order Runge-Kutta method to determine good approximations to the deterministic part of (4.17), i.e. the vectors $\mathbf{a}_i$. Each step is computed iteratively from the former. The result is a discrete set of points that approximate values of the exact solution. The stepwise linear function obtained by connecting the dots is an approximate solution to (4.2).

The formula for step $i+1$ given step i is $\mathbf{m}_{i+1} = \mathbf{m}_i + \Delta \mathbf{m}_i$ where

$$\Delta \mathbf{m}_i \quad = \quad \left(\frac{1}{2} \frac{\partial \mathbf{m}_i}{\partial t} + \frac{1}{2} \frac{\partial \mathbf{m}'_{i+1}}{\partial t} \right) \Delta t + \Delta \mathbf{f}. \tag{4.18}$$

The term in the paranthesis is $\mathbf{a}_i$. $\mathbf{m}'_{i+1}$ is notation for the Euler step,

$$\mathbf{m}'_{i+1} \quad = \quad \mathbf{m}_i + \Delta t \frac{\partial \mathbf{m}_i}{\partial t}. \tag{4.19}$$

Fig. (4.1.1) explains why this is more precise than a first order algorithm (which would be the Euler step alone): The start- and endpoint derivatives $\frac{\partial \mathbf{m}}{\partial t}(t_i)$ and $\frac{\partial \mathbf{m}}{\partial t}(t_{i+1})$ are both approximations to the average slope of $\mathbf{m}$ during Δt. Assuming that the second derivative of $\mathbf{m}$ does not change sign during Δt, the error made by these two choices have opposite signs. Therefore, some of the error will cancel out if we instead use an *average* of these two extremes as an approximation for the average slope of $\mathbf{m}$. However, since we have no way of knowing the true endpoint derivative $\frac{\partial \mathbf{m}}{\partial t}(t_{i+1})$, the derivative of the first-order endpoint is used as an approximation. This derivative is noted with a prime: $\frac{\partial \mathbf{m}'_{i+1}}{\partial t}$.

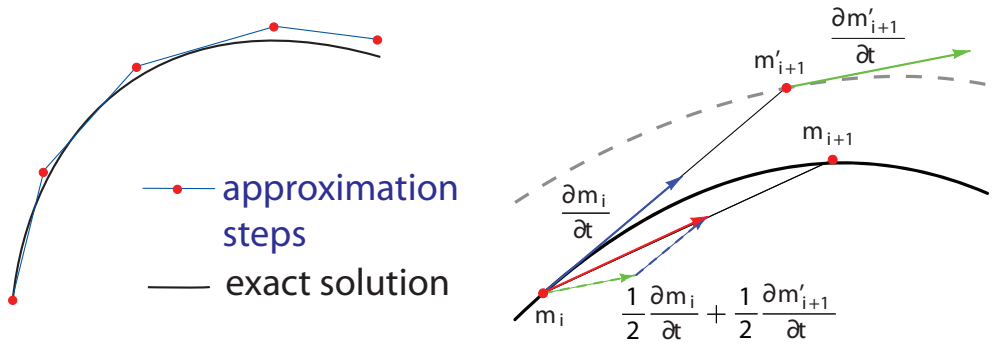

(a) *An exact solution compared to the result of a discrete approximation algorithm.*

(b) *Determination of the second order step. The red arrow is the deterministic slope* $\mathbf{a}_i$.

Figure 4.1: *A solution to a deterministic differential equation can be approximated by a stepwise linear function. The slope of each line segment is the average of the start-point derivative, and the approximate end-point derivative.*

Unless otherwise noted, the random term $\Delta\mathbf{f}$ was only evaluated at every 100'th deterministic step. This was done to speed up calculations – random number generation was time consuming. After applying the effect of the random term, the vectors $\mathbf{m}$ were renormalized to $|\mathbf{m}| = 1$. Although this integration error was quite small in each iteration, it could in some cases lead to significant errors over time.

4.1.2 Presentation

Visualization of discrete approximation solutions to (4.2) is a good way of acquiring an understanding of the dynamics of the simulated system. In the rest of the text I will use different sorts of visualizations:

1) The graph of $\mathbf{m}^A$ and $\mathbf{m}^B$ for $t \in [a, b]$: Two paths on the unit sphere. I will refer to this as the trajectory.

2) Time evolution of the cartesian coordinates of $\mathbf{m}^A$ along with the

"deviation angle" as a function of t. This angle is $\theta = |\pi - \frac{\mathbf{m}^A \cdot \mathbf{m}^B}{|\mathbf{m}^A||\mathbf{m}^B|}|$[a].

3) The power spectra of the x, y and z coordinates. These produce quantitative data. The power spectrum is a measure of intensity of signals as a function of frequency, and is given by

$$P_i(\omega) = |\text{fft}(m_i(t))|^2 \tag{4.20}$$

where "fft" denotes the result of a fast Fourier transform algorithm. This is an implementation of the Fourier transform, i.e.

$$\text{fft}(m_i(t)) \sim \hat{m}_i(\omega_n) = \frac{1}{\sqrt{t_N}} \int_0^{t_N} e^{i\omega_n t} m_i(t) \tag{4.21}$$

The MATLAB fft function is not defined exactly in this way, but it does obey the conventional properties of a Fourier transform. The difference is an overall multimplicative factor (which is unimportant) and artificially induced noise which was smoothed away by convolution with a sharply peaked Gaussian. All visualized power spectra are symmetric around $\omega = 0$. This choice was made to ease the comparison with scattering spectra. It is also a very convenient way of visualizing the peak centered around $\omega = 0$. Plots are usually in log scale and in units of energy, $\hbar\omega$.

4) Finally the simulated scattering spectrum

$$P = P_y + P_z \tag{4.22}$$

has a central role, as discussed in chapter 2. For long simulation times it should be considered an averaged quantity that is comparable to neutron scattering data. I will return to the point of defining "long" simulation times in a few sections.

4.2 Validation

I will now go through the elementary simulation results and show that these are explained by known simple cases. The fact that simulations behave as

[a] Usually θ is less than 0.5^o in simulations up to 300 K.

expected serves as validation.

4.2.1 Pure exchange precessions

Consider the effect of the exchange term only. Given an initial angle ϕ between the submagnetizations they will enter a precession, and I will now find the frequency. Consider the simple equation of motion

$$\frac{\partial \mathbf{m}^I}{\partial t} = -\gamma B_X^I \mathbf{m}^I \times \mathbf{m}^J. \tag{4.23}$$

This leads to

$$\frac{\partial \mathbf{m}^B}{\partial t} = -\frac{\partial \mathbf{m}^A}{\partial t}. \tag{4.24}$$

Since $\frac{\partial \mathbf{m}^I}{\partial t}$ is perpendicular to the plane spanned by $(\mathbf{m}^A, \mathbf{m}^B)$, the trajectories of $\mathbf{m}^A$ and $\mathbf{m}^B$ must be circles around a rotation axis ω, where ω is a vector of a length $|\omega|$ equal to the precession frequency. This rotation axis must be contained in the plane spanned by $\mathbf{m}^A$ and $\mathbf{m}^B$, and pass through the origin $\mathcal{O}$: Due to symmetry, both moments must precess on the same circle, and ω must be proportional to $\mathbf{m}^A + \mathbf{m}^B$. Indeed, $\mathbf{m}^A + \mathbf{m}^B$ is a constant of motion, since $\frac{\partial(\mathbf{m}^A + \mathbf{m}^B)}{\partial t} = 0$. See Fig. 4.2a for a graphical explanation.

Then the radius of the circle of precession is

$$r = \sin\left(\frac{\phi}{2}\right), \tag{4.25}$$

and the precession frequency is given by

$$\begin{aligned}
|\omega| &= \frac{\frac{\partial \mathbf{m}^I}{\partial t}}{r} && (4.26)\\
&= \frac{|\gamma B_X \mathbf{m}^A \times \mathbf{m}^B|}{\sin(\frac{\phi}{2})} && (4.27)\\
&= |\gamma| B_X \frac{\sin(\phi)}{\sin(\frac{\phi}{2})} && (4.28)\\
&= 2|\gamma| B_X \cos(\frac{\phi}{2}) && (4.29)\\
&= 2|\gamma| B_X \sin(\frac{\theta}{2}). && (4.30)
\end{aligned}$$

where $\theta = |\pi - \phi|$ is the deviation angle. The simulated precession frequency is plotted along with formula (4.29) in Fig. 4.2b.

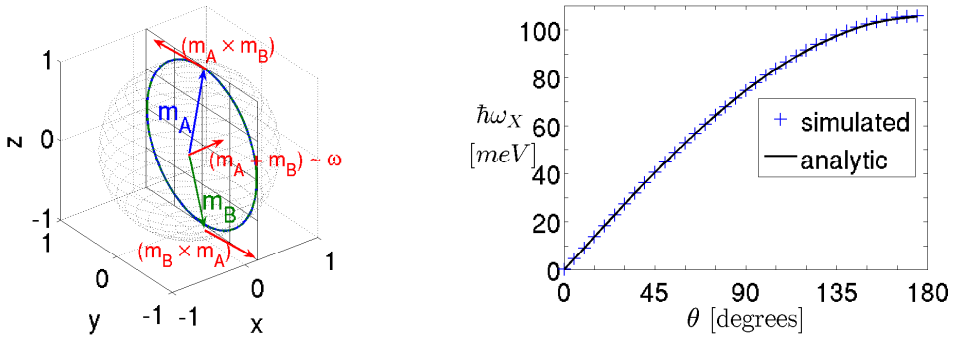

(a) *The submagnetization trajectories describe the circle of radius* $r = \sin(\frac{\theta}{2})$.

(b) *Exchange precession frequency* $\hbar|\omega|$ *as a function of an initial submagnetization angle* $\theta = |\pi - \phi|$.

Figure 4.2: *Torque from the exchange field due to a deviation angle* θ *gives rise to precessions.*

4.2.2 Collective precession modes

Time evolution of the system uncoupled from the heat bath is described by the equation

$$\frac{\partial \mathbf{m}^I}{\partial t} = \gamma \mathbf{m}^I \times \mathbf{B}_{\text{sim}}. \tag{4.31}$$

The solution trajectories are uniquely defined by initial conditions. There are two distinct precession modes – one for each anisotropy. These are the previously discussed modes due to collective magnetic excitations, or $q = 0$ spinwaves. Choosing the non-trivial initial conditions of rotating both moments an angle around the x-axis, i.e. exciting into the y-axis, the low-frequency axial anisotropy mode is excited. Rotation around the y-axis, into the x direction, yields a high-frequency precession in the strong planar anisotropy. Most other choices of initial conditions excite both modes and gives a mixed precession. Example trajectories are shown in fig. 4.3. The

motion shown in Figs. 4.3a and 4.3b are ellipses, although so narrow that they appear as straight lines to the plain eye.

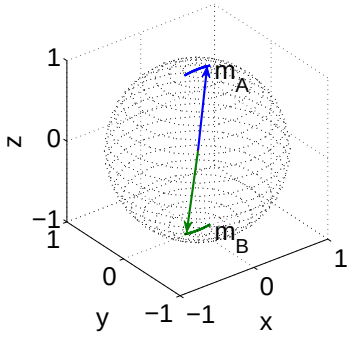

(a) *Planar anisotropy precession.*

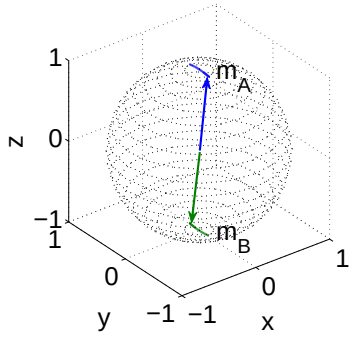

(b) *Axial anisotropy precession.*

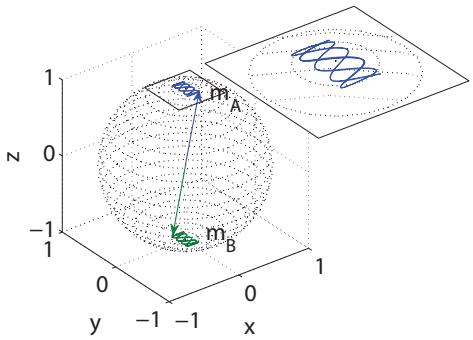

(c) *A mixed mode.*

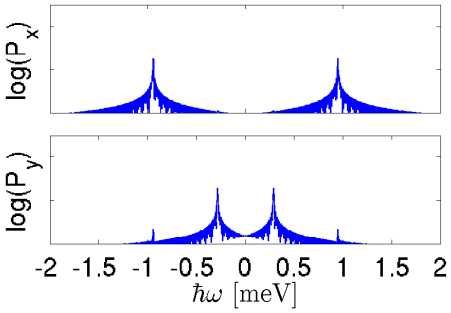

(d) *Power-spectrum of the mixed mode.*

Figure 4.3: *Example trajectories visualized on the unit sphere. The collective precession modes are strongly elliptical.*

It is only in the small amplitude limit that the precession frequency $\hbar\omega$ corresponds to that of single, low temperature $q = 0$ spinwave excitations (with energies (3.17) and (3.18)). Fig. 4.4 shows the peak position of the simulated collective modes compared to the analytic expressions

$$\hbar\omega_x = \pm 2g\mu_B\sqrt{(-B_1 + B_2)(B_X + B_2)} \tag{4.32}$$

$$\hbar\omega_y = \pm 2g\mu_B\sqrt{B_2(B_X - B_1 + B_2)} \tag{4.33}$$

from chapter 3.1. I have used the redefined anisotropy and exchange fields (3.56) and (3.57).

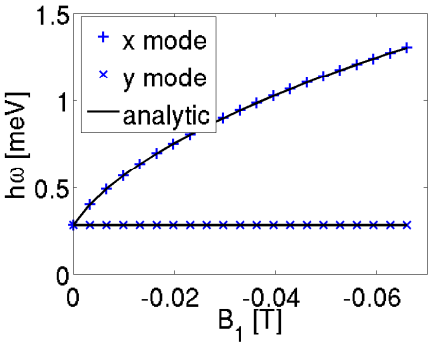

(a) *CME frequency vs. axial anisotropy field* $\mathbf{B}_1$.

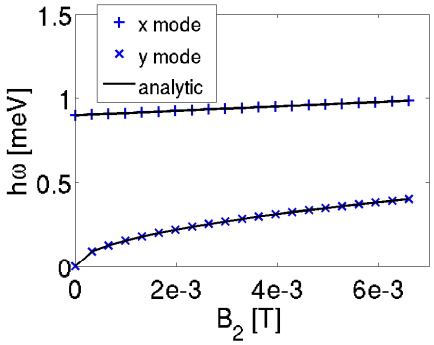

(b) *CME frequency vs planar anisotropy field* $\mathbf{B}_2$.

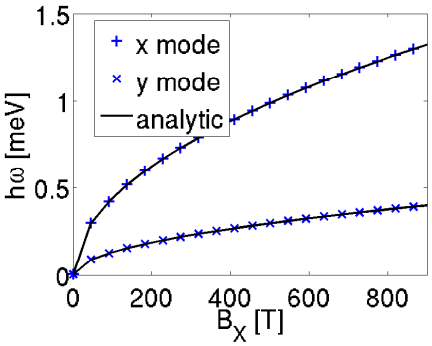

(c) *CME frequency vs. exchange field* $\mathbf{B}_X$.

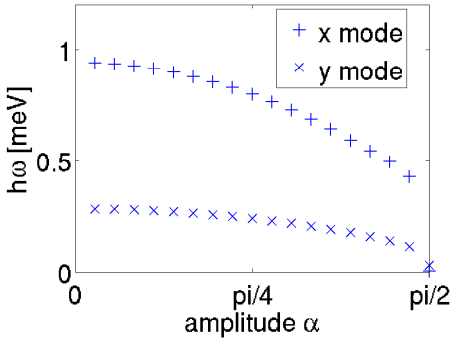

(d) *The anharmonic effect – frequencies decrease with precession amplitude* α.

Figure 4.4: *Simulated precession mode frequencies and analytic CME energies plotted vs. the anisotropy and exchange fields. I have used the typical values of* $B_1 = -30 \cdot 10^{-3}\,T$, $B_2 = 3 \cdot 10^{-3}\,T$ *and* $B_X = 455\,T$.

In the small amplitude limit the axial anisotropy field is constant since $(0, 0, B_2 m_z^I) \cong (0, 0, B_2)$ and the 1-D harmonic oscillator is a good approximation for axial precessions in the y-z plane (see Fig. 2.5). When the local anisotropy field deviates from a simple harmonic oscillator the precession frequency is reduced. This is the anharmonic effect discussed in chapter 2, from the classical viewpoint. From the quantum mechanical viewpoint, the application of excitations to the ground state (something close to the Néel state) changes the state, and this changes the conditions on which the

spinwave energies were calculated. The anharmonic effect was observed in [7] and will also be observed in the temperature dependent simulations later on. An analytic expression was not found.

Notice that the planar precession frequency depends notable on B_2. The axial anisotropy has cylindrical symmetry and thus the total anisotropy field of a rotation into the x direction is $(-B_1 m_x^I, 0, B_2 m_z^I)$, i.e. the moments are not influenced by B_1 alone.

4.2.3 The effect of damping

Consider the addition of a damping term to the zero-temperature equation of motion:

$$\frac{\partial \hat{\mathbf{m}}^I}{\partial t} = \gamma \hat{\mathbf{m}}^I \times \mathbf{B}^I_{\text{sim}} - \lambda|\gamma| \hat{\mathbf{m}}^I \times \hat{\mathbf{m}}^I \times \mathbf{B}^I_{\text{sim}}. \tag{4.34}$$

As will be confirmed in the next section, damping is a measure of how strongly the system is connected to the heat bath.

Fig. 4.5 shows an example of a time evolution according to (4.34) and the corresponding power spectra $P_x = |\text{fft}(m_x(t))|^2$ and $P_y = |\text{fft}(m_y(t))|^2$. I have chosen an initial excitation of both modes and observed the decay. The positions of peak maxima in Fig. 4.5b are unchanged, but the peaks now have a finite width compared to the corresponding undamped spectra in Fig. 4.3d.

Fig. 4.6 shows the HWHM (half width at half max) of the simulated peaks as a function of λ. Notice that surprisingly, both peaks broaden identically. This means that the decay half-time of each mode is not simply related to the damping parameter times the frequency, as in the case of a single magnetic moment in a constant field where $\tau = \lambda\omega$, but appears to depend on a common parameter. This is possibly due to the coupling of the two modes through the damping parameter λ. At $\lambda \cong 0.004$ the y-mode becomes overdamped (see Fig. 4.6a and 4.6b). An overdamped oscillator

does not hold information about a precession frequency. Furthermore, experimental data was fit by a weakly damped harmonic oscillator (see chapter 5). The nanoparticle system is thus exected to be weakly damped.

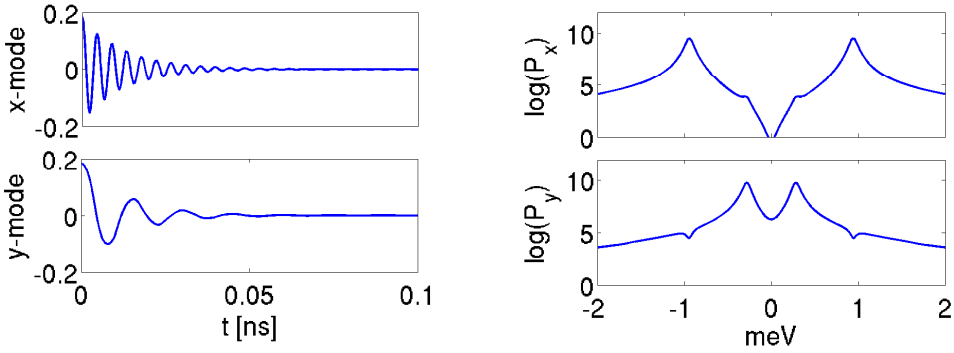

(a) *Time evolution of a weakly damped precession with* $\lambda = 10 \cdot 10^{-4}$.

(b) *Corresponding power spectra.*

Figure 4.5: *Example time evolution of a damped precession and the corresponding power spectra of the* x *and* y *modes. Notice that both modes decay simultaneously.*

4.2.4 Paramagnetic temperature test

In order to show that the temperature implementation (the implementation of (3.141)) functions correctly, I have determined the temperature dependent magnetization of a magnetic moment in a constant external field pointing in the z direction. This is a textbook problem in basic magnetism [3]. The Langevin equation is

$$\frac{\partial \mathbf{m}}{\partial t} = \gamma \mathbf{m} \times (\mathbf{B} + \mathbf{b}) - \lambda |\gamma| \mathbf{m} \times \mathbf{m} \times \mathbf{B} \tag{4.35}$$

where $\mathbf{B} = (0, 0, B_{\text{ext}})$ is a constant external field.

At zero temperature, the moment is aligned with the external field. As the temperature rises the moment enters a sort of damped Larmor precession disturbed by fluctuations, and the average amplitude increases with temper-

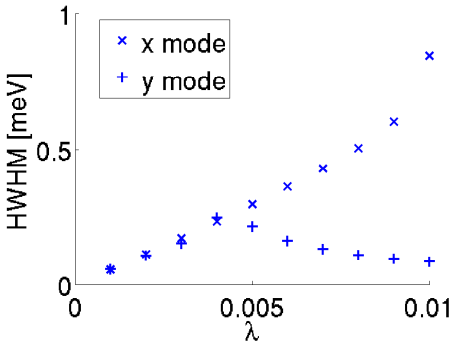

(a) HWHM of the power spectrum peaks. The y -mode becomes over-damped at $\lambda \cong 4 \cdot 10^{-3}$.

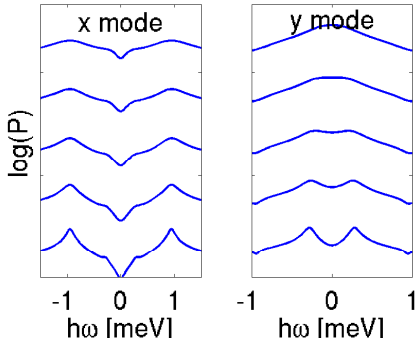

(b) $\lambda = 10 \cdot 10^{-4}$ *(bottom) to* $\lambda = 50 \cdot 10^{-4}$ *(top).*

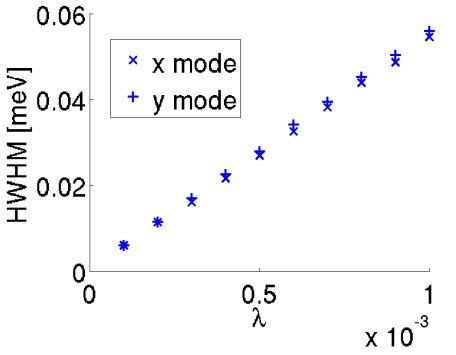

(c) For $\lambda < 4 \cdot 10^{-3}$ the modes decay simultaneously and the HWHM is a linear function of λ.

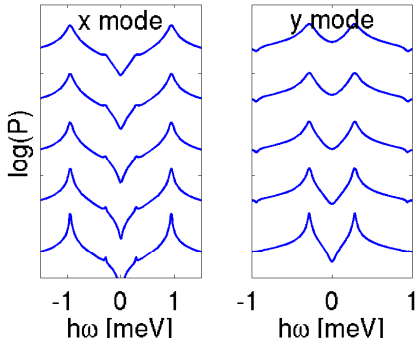

(d) $\lambda = 2 \cdot 10^{-4}$ *(bottom) to* $\lambda = 10 \cdot 10^{-4}$ *(top).*

Figure 4.6: *Peak broadening scans and power spectrum examples of the x and y mode as a function of damping strength λ. The HWHM was calculated from half maximum at both sides of the peak when possible, otherwise from the outside.*

ature. The theoretical temperature dependency of the average moment in the z direction is given by

$$\frac{< m_z >}{M} = L \tag{4.36}$$

where $M = g\mu_B S$ is the size of the magnetic moment. The size M only enters the equation of motion through the amplitude of the excitations, and the motion is described by the unit vector $\mathbf{m}$. L is the Langevin function

given by

$$L = \coth\left(\frac{MB}{k_B T}\right) - \frac{1}{\frac{MB}{k_B T}}. \tag{4.37}$$

The susceptibility χ is thus given by the equation

$$M < m_z >= \chi \frac{B_z}{\mu_0}. \tag{4.38}$$

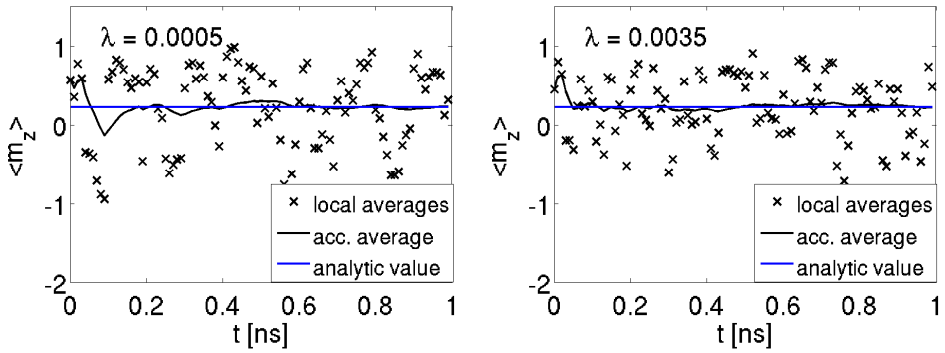

Figure 4.7: $< m_z >$ *is the average magnetization of the moment* $M = g\mu_B s$ *in* $B = 90\,T$ *at* $T = 500K$. $L = 0.23$ *is indicated by the horizontal lines. The full line is the accumulated average of the crosses.*

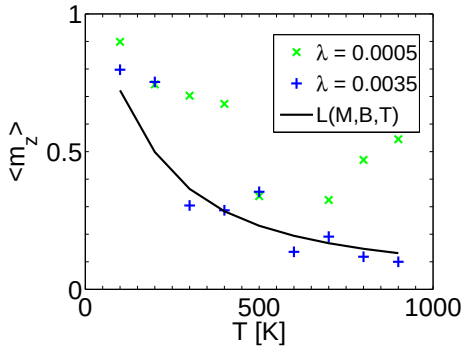

Figure 4.8: *Simulated values of* $< m_z >$ *after only 2 ns.* $< m_z >$ *converges much faster for* $\lambda = 35 \cdot 10^{-6}$ *than for* $\lambda = 5 \cdot 10^{-6}$.

The approach to equilibrium as a function of time is shown in Fig. 4.7, for the example values $\lambda = 5$ and $35 \cdot 10^{-4}$, at $B_z = 90$T and $T = 500$K.

Local average values of m_z are indicated by the crosses, and the accumulated average of these values is plotted vs. time by the solid black line. It is clear from Fig. 4.7 and 4.8 that $< m_z >$ converges to the analytic values. The decay time shortens with increasing λ, which confirms that λ can be considered the thermal coupling strength.

This section confirms the implementation of the Einstein relation.

4.2.5 Temperature calibration

It is useful to determine an upper bound on the timestep Δt below which the corresponding random step $\Delta \mathbf{f} = \gamma\ \mathbf{m} \times \Delta \mathbf{b}$ did not lead to systematic errors in the paramagnetic simulation in section 4.2.4. It is reasonable to assume that the same bound on the random step leads to the correct temperature for the full nanoparticle simulations. For some larger values of Δt the simulations did not converge to the correct temperature, so it is important that the time step is small enough.

Consider the formula (4.16) for the variance of the random field $\Delta \mathbf{b}$:

$$< (\Delta b_i^I)^2 > = 2\frac{\lambda}{|\gamma| M^I} k_B T \Delta t_{\text{eff}} \tag{4.39}$$

$$= \left(\frac{2\lambda k_B T}{|\gamma| M^I} \right) \times \Delta t_{\text{eff}} \tag{4.40}$$

Since the random term was only inserted every 100'th deterministic iteration, the effective time step is 100 times larger; $\Delta t_{\text{eff}} = 100 \Delta t$.

In the paramagnetic test simulations the temperature was $T = 500$ K, $\lambda = 35 \cdot 10^{-4}$ and $M = g \mu_B s$. According to (4.40) the variance of the random field was

$$< (\Delta b_i^I)^2 >= 4.9977 \cdot 10^{-26}. \tag{4.41}$$

The standard deviation is thus

$$\sigma_{\text{para}} = 2.2356 \cdot 10^{-13}. \tag{4.42}$$

The standard deviation of $\Delta\mathbf{f}$ is therefore

$$\sigma_{\Delta\mathbf{f}} = |\gamma| \times 1 \times \sigma_{\text{para}} = 3.9358 \cdot 10^{-2} \cong 0.04. \tag{4.43}$$

This is the typical size of a random step. Compared to the size of the normalized moment ($|\mathbf{m}| = 1$) the stepsize is about 4%. This is a rather large distance, but not unreasonable and it yields the correct temperature.

Consider now the stepsize in the full simulation. An 8 nm hematite nanoparticle holds about $1.05 \cdot 10^4$ ionic sites, so $M^I = \frac{1.05 \cdot 10^4}{2} g\mu_B$. Simulations at temperatures above 500 K are not required, and there is an upper bound on λ of about $6 \cdot 10^{-3}$ (this is slightly above the value of λ for which the y-mode becomes overdamped - see Fig. 4.6a). The resulting upper bound $\Delta t_{\text{eff,max}}$ on the effective time step Δt_{eff} is

$$\left(\frac{2\lambda k_B T}{|\gamma| M^I}\right)_{\max} \times \Delta t_{\text{eff,max}} = 8.1595 \cdot 10^{-16} \Delta t_{\text{eff,max}} = 4.9977 \cdot 10^{-26}$$

which gives the upper bound on the effective timestep is given by

$$< (\Delta b_i^I)^2 >= \Delta t_{\text{eff,max}} = 6 \cdot 10^{-11}\text{s}. \tag{4.44}$$

This translates into the timestep bound $\Delta t_{\max} = 6 \cdot 10^{-13}$s. This bound makes sure that the random step does not cause detectable systematic errors. For simplicity, all simulations use the value $\Delta t = 1 \cdot 10^{-14}$s, including all validations in this chapter not involving a random term. It turned out that this value for did not lead to any deterministic integration errors[b].

4.2.6 Convergence of power spectra

This section illustrates how to take the the average $< P >$ of a power spectrum P. This is the average in the left hand side of (2.12). The average I have used is time-average: over time, solution trajectories visit the total set

[b] In retrospect, the choices for the timesteps were safe, but not optimal. An increase of Δt and a decrease of Δt_{eff}, both by a factor of 5 or 10, would lead to a shorter computation time with little to no loss of precision. However, the final results are unchanged.

of possible paths in a representative way. The power spectrum of a statistically representative sample of trajectories is thus an averaged quantity.

The practical way of taking the power spectrum of a long time evolution is based on the linearity of integration limits: The power spectrum of one 10 ns trajectory from t_0 to t_{10}, is equal to the sum of the 10 power spectra of the 1 ns sub-trajectories from t_i to t_{i+1}. In symbols,

$$P\Big|_{t_0}^{t_N} = \sum_{i=1}^{N-1} P\Big|_{t_i}^{t_{i+1}}. \tag{4.45}$$

This allows one to simulate a couple of trajectories (as much as the computer can handle), take the norm square of the Fourier transforms (the power spectra), and add these. The resulting power spectrum is a better average than any of it's constituents.

I have determined the required simulation time from a simple observation: Convergence. When the shape of the power spectrum in a log scale ceases to evolve, it has converged, and the containing trajectories are taken to be statistically representative. Note that total multiplicative factors do not change the shape of a graph in log scale and that such factors are unimportant – it is never nesseccary to compare absolute intensities. Fig. 4.9 and 4.10 shows the convergence of such a series of power spectra.

All spectra in the next chapter were simulated for at least 60 ns, to be safe. After all, lower temperatures and different values of λ may increase the required simulation time before convergence is reached.

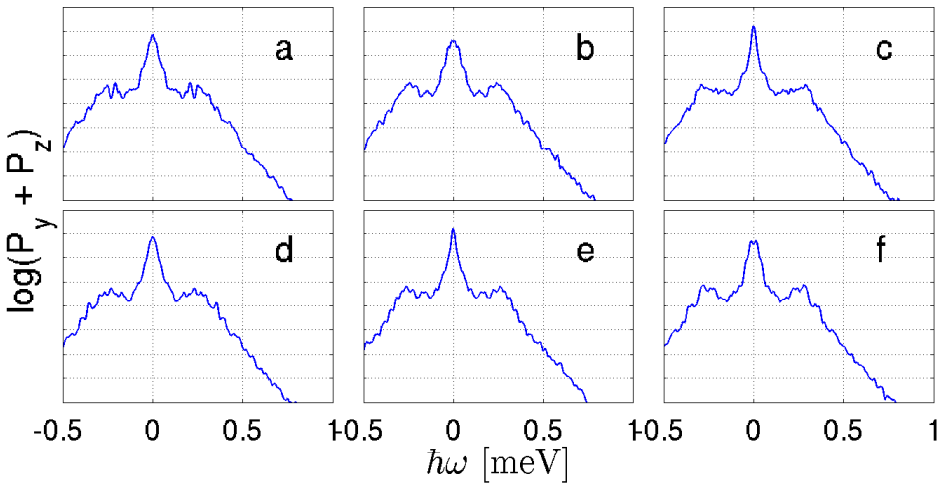

Figure 4.9: *Close-up of example power spectra of 1 ns simulations at 100 K. Each one is a little different and therefore cannot be representative for statistical properties.*

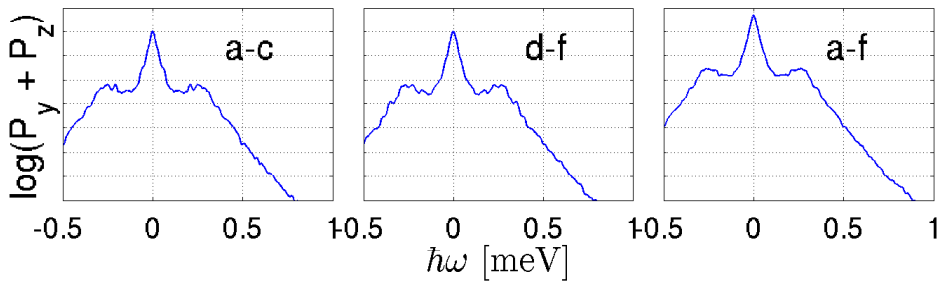

Figure 4.10: *Sums of the spectra in Fig. 4.9. The sums (a to c) and (d to f) are almost the same. The final sum of all spectra (a to f) is converged.*

Chapter 5

Results

The nanoparticle system was simulated at temperatures ranging from 0 to 300 K. The results are presented in this chapter.

Insight into the simulated dynamics is found by direct observation. Quantitative comparison to experiment is then performed.

5.1 Observations

The following is an illustrative description of how the simulated nanoparticle system behaves as a function of temperature, at a fixed set of parameter values. The chosen values of the parameters B_1, B_2, B_X N and λ, are the ones that in the end yield the best fit to experiment.

The term "states" refers to configuration space states.

5.1.1 Low temperature observations

Simulation results at temperatures up to ∼60 K have common features.

Fig. 5.1 is a 3-D visualization of the density of states at 40 K. An evenly dispersed subset of trajectories accumulated over 10 ns are shown as points on the unit sphere. The figure shows how the submagnetizations are confined to the basal plane (the y-z plane) and primarily orient in the easy direction

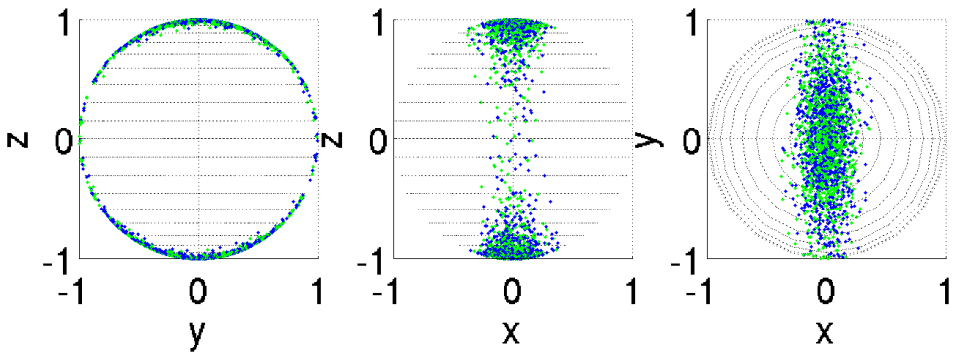

Figure 5.1: *Density of states visualization at 40 K. Submagnetizations orient primarily in the z direction and are confined to the basal plane (the y-z plane).*

(the z direction). The few states perpendicular to the easy direction are added by occasional superparamagnetic flips.

Examples of time evolutions are shown in Fig. 5.2 and many more are found in appendix C. The deviation angle $\theta = |\pi - \frac{\mathbf{m}^A \cdot \mathbf{m}^B}{|\mathbf{m}^A||\mathbf{m}^B|}|$ measures how close the submagnetizations are to anti-alignment. Notice that it is always less than half a degree at low temperatures. Consider the time evolution graphs of the x and y coordinates. The visible oscillations are the collective modes. The amplitudes of these modes change randomly according to fluctuation and dissipation. The graphs are influenced by small ripples. Some of these ripples are simply due to the fact that the motion takes place on a sphere and the coordinates are therefore correlated. Others are due to random walk. The few y precessions of very large amplitude (close to 1) appear to have a slightly longer precession time than small amplitude precessions – perhaps an early hint of anharmonic effect. The signal is mixed with thermal noise which increases with temperature.

Consider the z component in Fig. 5.2. At 20 K the z component is almost constant. No superparamagnetic barrier crossings were observed at this

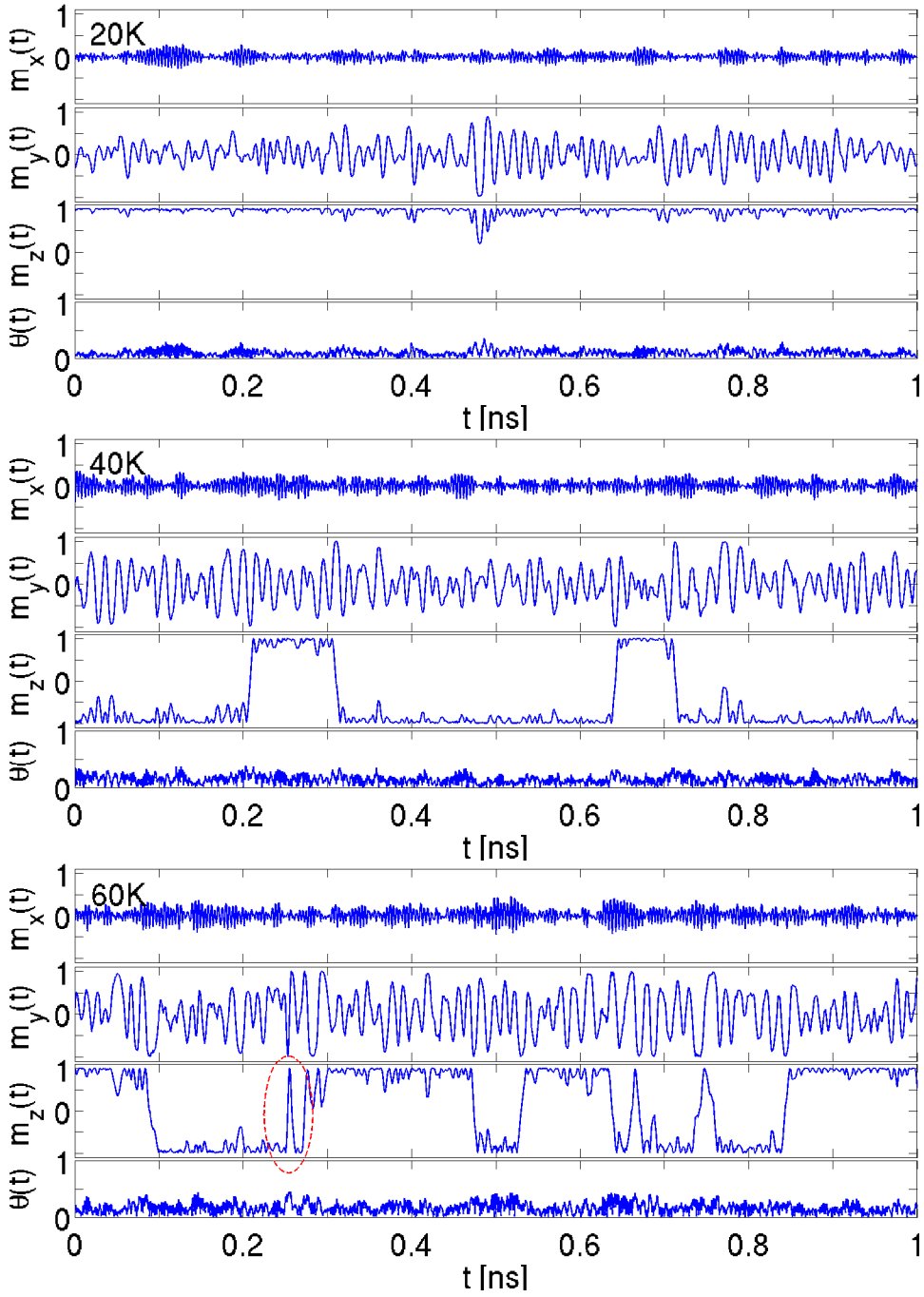

Figure 5.2: *Time evolution snapshots of submagnetization A at $T = 20$, 40 and 60 K. The dashed red line incircles a double-flip example.*

temperature. At higher temperatures the system shows superparamagnetic behavior as the z component crosses the axial anisotropy barrier and changes sign. The superparamagnetic flip expectation time decreases visibly from 40 K and up.

These observations show that the classical picture of collective precession modes and superparamagnetism holds for the simulated system at low temperatures.

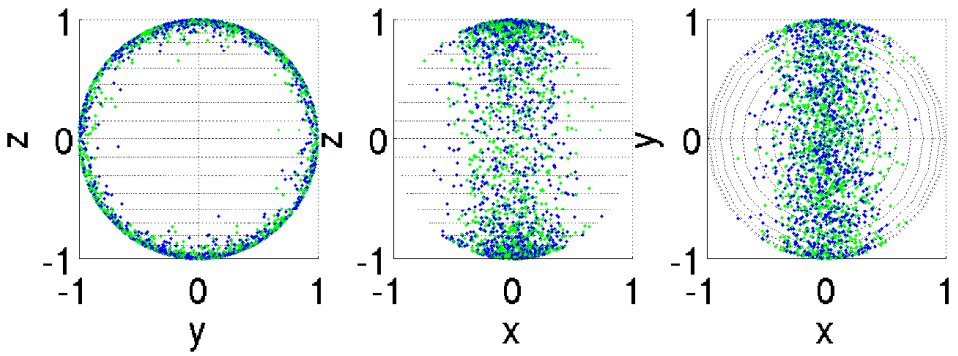

Figure 5.3: *Density of states visualization at 150 K. States are more evenly distributed within the basal plane and amplitudes in the x direction are stronger.*

5.1.2 Mid-range temperature observations

The dynamics change as temperature rises above 80-100 K. Fig. 5.3 shows the sampled density of states at 150 K. The submagnetizations enter states out of the basal plane with much higher probability. The state distribution within the basal plane is much more even than in the low temperature case (see Fig. 5.1). This indicates that the superparamagnetic activity is drastically increasing.

Consider the example time evolutions from 80 to 150 K in Fig. 5.4. The superparamagnetic flip expectation time has visibly decreased, the motion becomes more disturbed by fluctuations, and precession amplitudes are larger. The deviation angling θ momentarily fluctuates beyond half a degree. Rather than single crossings, some of the flips are sharp spikes forth and *back* across the barrier. A few examples are indicated by the dashed circles 60 K and 100 K. These back-flips happen immediately and quite often, and are a deviation from ferromagnetic superparamagnetism in which flips are uncorrelated.

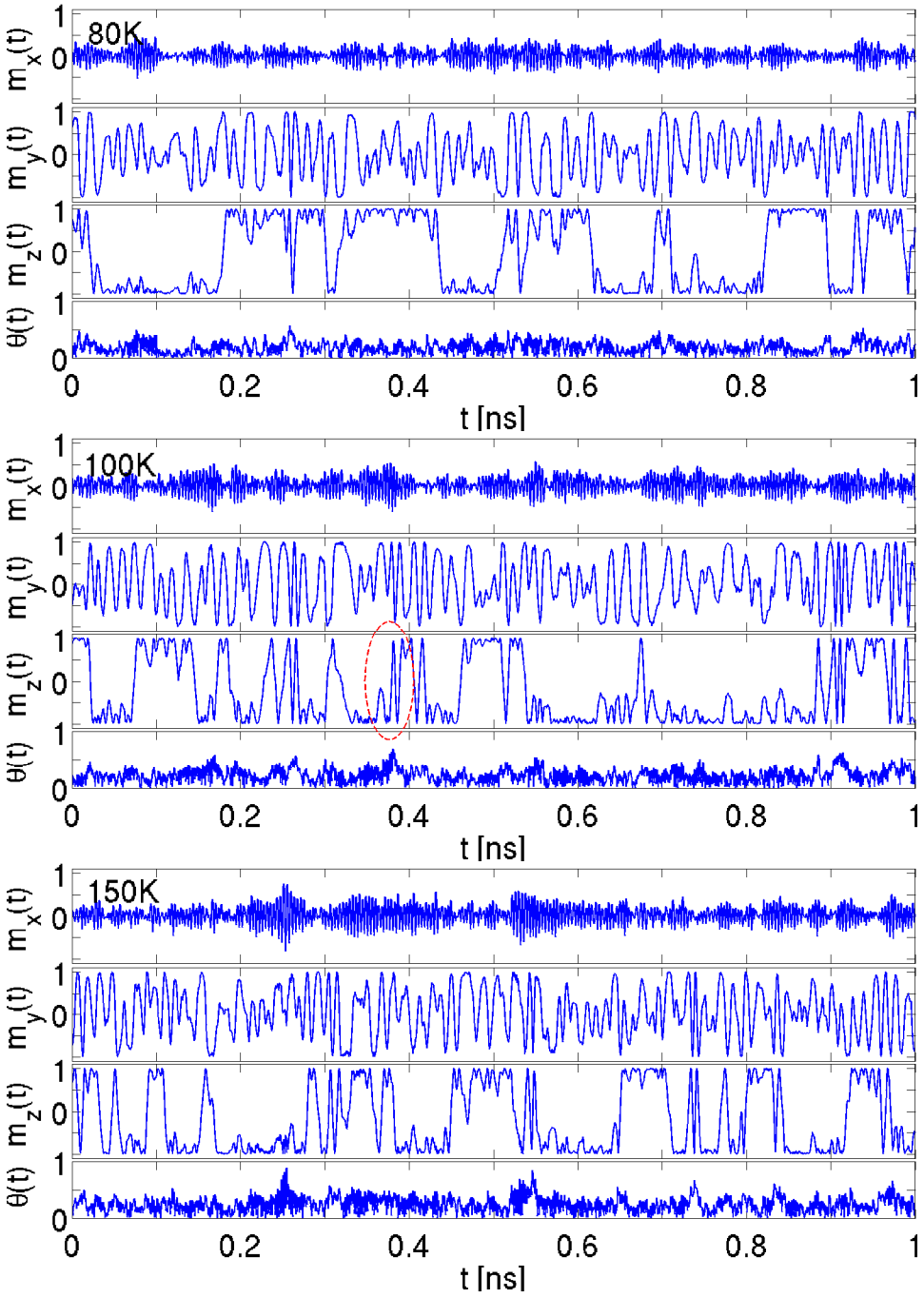

Figure 5.4: *Time evolution snapshots of submagnetization A at* $T = 80$*, 100 and 150 K. The dashed red circle is a double-flip example.*

Although the picture of collective precessions and superparamagnetism still holds, the simple classical picture of is slowly breaking down.

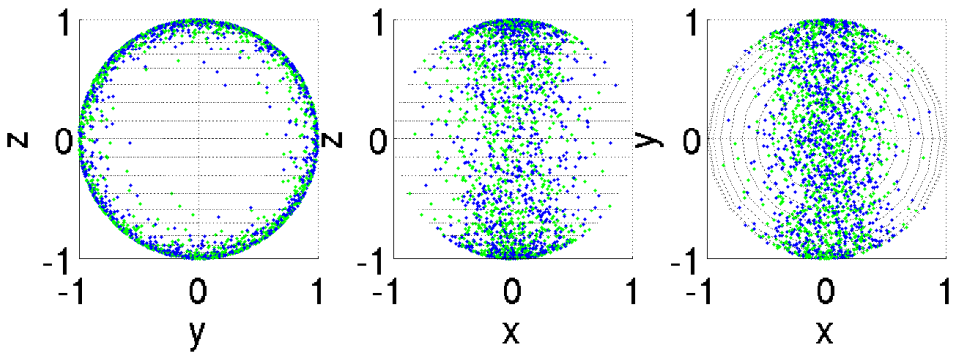

Figure 5.5: *Density of states at $T = 300K$. The easy direction is barely recognizable and the submagnetizations are no longer confined to the basal plane though never excited into the x direction.*

5.1.3 Higher temperature observations

The density of states visualization at 300 K in Fig. 5.5 shows almost as frequent an occupation of states in the y direction as in the "easy" z direction, and very large amplitudes out of the basal plane. The moments are no longer confined to the basal plane, but orientations within the basal plane are still preferred.

Time evolution examples at 200-300 K are found in Fig. 5.6. The previous superparamagnetic flips is now an almost constant crossing of the axial anisotropy barrier. At times this frequent crossing appears to be regular or periodic. This is in sharp contrast to the random timing of superparamagnetic flips in the classic ferromagnetic picture. A few examples of this periodic motion are indicated by the solid red circles in Fig. 5.6. This motion is in all cases characterized by a y-z precession. Moreover, there appears to be a correlation with θ which often excites beyond half a degree in these cases.

In conclusion, these observations show that the simulated system devi-

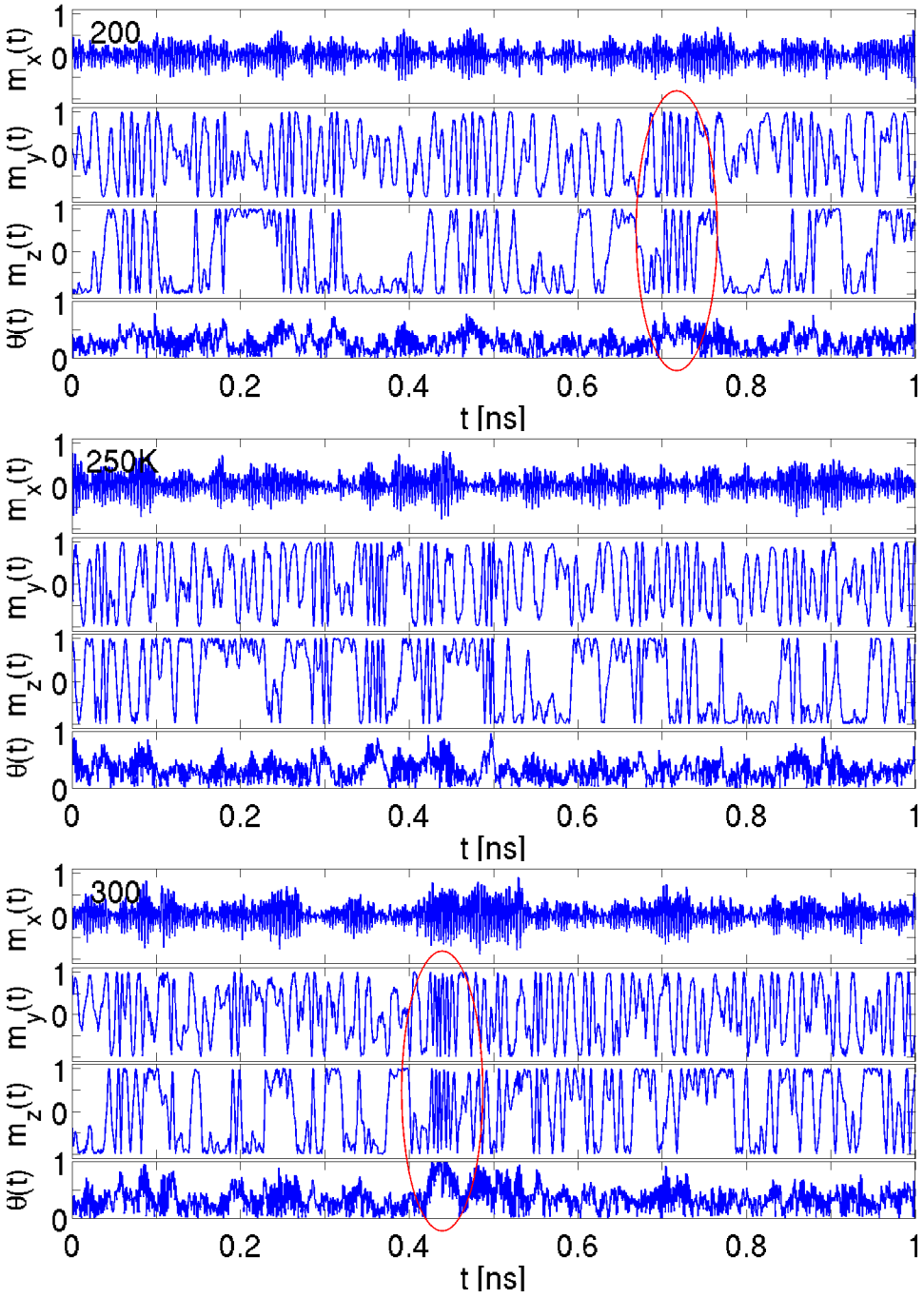

Figure 5.6: *Time evolution snapshots of* $\mathbf{m}^A$ *at 200, 250 and 300 K. The red circles indicate periodic y-z precessions.*

ates from the classical picture of collective precessions and (uncorrelated) superparamagnetic flips from temperatures of 150-200 K and up.

5.1.4 Power spectra and the simulated scattering spectrum

The power spectrum is the frequency intensity spectrum of the typical motion. If precessions of a certain frequency arise often, the intensity is high at that point (relative to other frequencies). All displayed power spectra are averaged, i.e. their shapes in a log plot have converged, as described in section 4.2.6. The power spectrum of the cartesian coordinates of $\mathbf{m}^A$ is displayed in Fig. 5.7. The power spectra of the x and y coordinates show distinct peaks at the collective mode frequencies, and these peaks are broadened as the temperature increases. The power spectrum of the z component shows a strong central peak with flat shoulders. As the temperature increases, the spectra smear out and flatten.

The sum of the power spectra of the y and z components, $P_y + P_z$, is also displayed in Fig. 5.7. As mentioned throughout this thesis and described in chapter 2 this can be compared directly to neutron scattering data. Therefore $P_y + P_z$ was called the simulated scattering spectrum. At 40 K the central peak of the simulated scattering spectrum is intense and sharp, and the sidepeak easily distinguishable. As the temperature increases the central peak looses intensity compared to the sidepeaks, that grow stronger and smear out over a wider frequency range. Experimentally, the central peak is due the static component m_z and broadens because of superparamagnetism and random motion. The simulated center peak indeed seems to broaden with temperature.

Simulated scattering spectra from 20 K to 300 K are compared in Fig. 5.8. As the temperature increases, a continuum of frequencies above $\sim$0.3 meV becomes more intense. The sidepeak position decreases slightly, then increases with temperature. The central peak broadens and looses intensity.

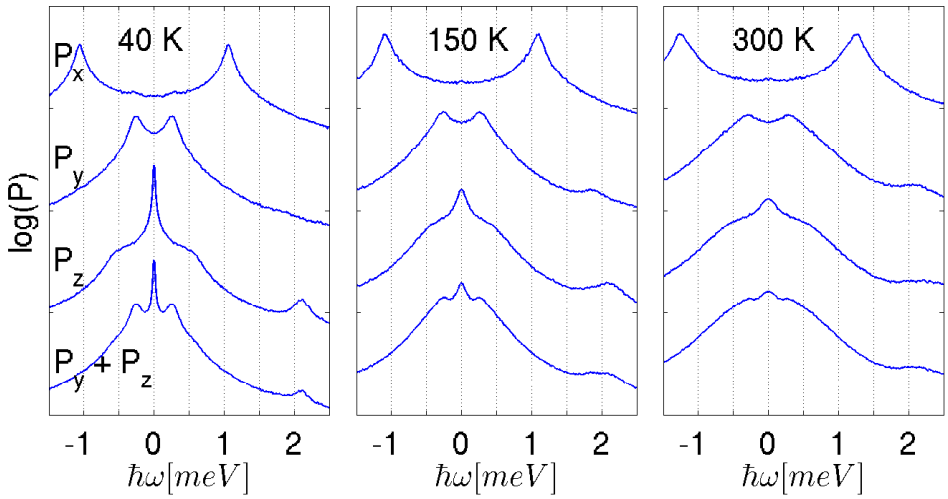

Figure 5.7: *Power spectra and the simulated scattering spectrum of* $\mathbf{m}^A$. *The collective mode sidepeaks are clearly distinguishable. All features are broadened or flattened with temperature.*

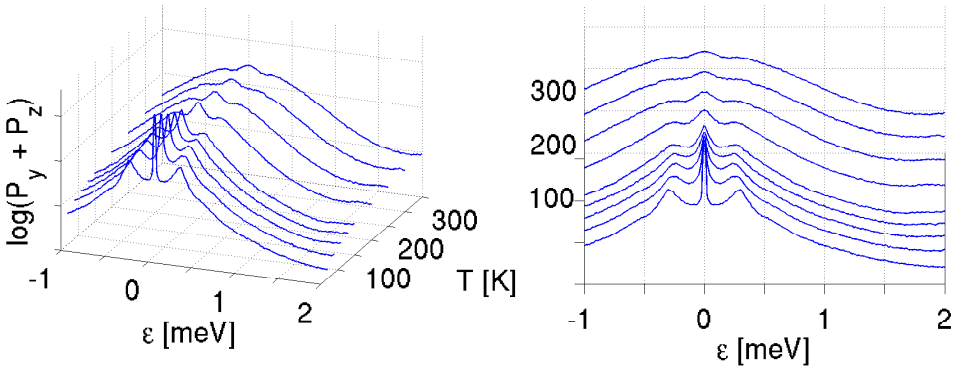

Figure 5.8: *Temperature scan of the simulated scattering spectra. The central peak diminishes with temperature. The sidepeak position decreases, and increase at higher temperatures.*

5.2 Comparison to experiment

The experimental and simulated scattering spectra are not compared directly. A number of physical and instrumental effects are blended with the experimental signal. I will not consider any of these effects and take all fits

to experimental data for granted. The experimental fits were done by Luise T. Kuhn.

In order to get a quantitative means of comparison to experiment, the same underlying signal function is applied to the simulated scattering spectra. It turned out that this function is able to very closely fit simulated scattering spectra.

All fits were done using Mfit which is an custom fitting tool for MATLAB originally developed at ILL.

5.2.1 Fitting method

The experimental fitting method used to fit the RITA II data is described in [10] and I will merely state the fitting functions without going into too much detail.

The *signal function* that was used to fit experimental scattering data is

$$I(\varepsilon) = \frac{A_{\text{Bragg}}}{\pi}\frac{\Gamma}{\Gamma^2+\varepsilon^2} + \frac{A_{\text{CME}}}{\pi}\frac{2\gamma\varepsilon_0^2}{(\varepsilon^2-\varepsilon_0^2)^2+4\gamma^2\varepsilon_0^2}. \tag{5.1}$$

This is the sum of a "quasielastic" Lorentzian

$$\text{L}(\varepsilon) = \frac{A_{\text{Bragg}}}{\pi}\frac{\Gamma}{\Gamma^2+\varepsilon^2}, \tag{5.2}$$

and a damped harmonic oscillator (DHO),

$$\text{DHO}(\varepsilon) = \frac{A_{\text{CME}}}{\pi}\frac{2\gamma\varepsilon_0^2}{(\varepsilon^2-\varepsilon_0^2)^2+4\gamma^2\varepsilon_0^2}. \tag{5.3}$$

Here Γ is the width of the Lorenzian and γ is the DHO width (FWHM of each sidepeak) and $\pm\varepsilon_0$ is the DHO center (sidepeak) position. These functions are normalized such that $A_{\text{Bragg}} = \int_{-\infty}^{\infty} d\varepsilon L(\varepsilon)$ and $A_{\text{CME}} = \int_{-\infty}^{\infty} d\varepsilon DHO(\varepsilon)$ are the area parameters. The terms "quasielastic" and "damped harmonic oscillator" are chosen for strategic reasons, but it should be clear by now that the 1-D damped harmonic oscillator model discussed in chapter 2 indeed fails at higher temperatures. For now the signal function should merely be

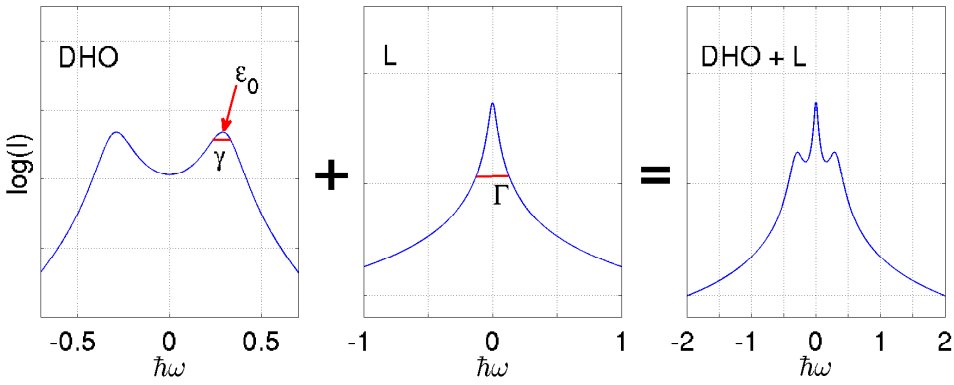

Figure 5.9: *The signal function (5.1) is the sum of a damped harmonic oscillator and a "quasielastic" Lorentzian. This is the underlying function used to fit data in Fig. 5.10.*

regarded a quantitative measure and a means of comparing simulation to experiment.

The high resolution backscattering data was fit by a single Lorenzian. The measured energy interval was up to 15μeV.

Due to the nature of the numerical algorithm, artifact oscillations are superimposed onto the simulated scattering spectrum. I have convoluted all spectra with a Gaussian to smooth them prior to fitting and observation. The Gaussian used for the observed power spectra has a standard deviation of $\sigma = 0.006$ meV, and the Gaussian for the fitted power spectra corresponds to the instrument resolution function, which has $\sigma = 0.051$ meV. The fitting function is the convolution of (5.1) with the instrument resolution Gaussian. This choise of Gaussian was made to even the conditions for simulated and experimental fits as much as possible. See Fig. 5.9 for a graph of the signal function, and Fig. 5.10 for the corresponding fitting functions used to fit simulated and experimental scattering spectra.

The resulting fitting parameters of simulated and experimental data can be directly compared. This is done in the next section.

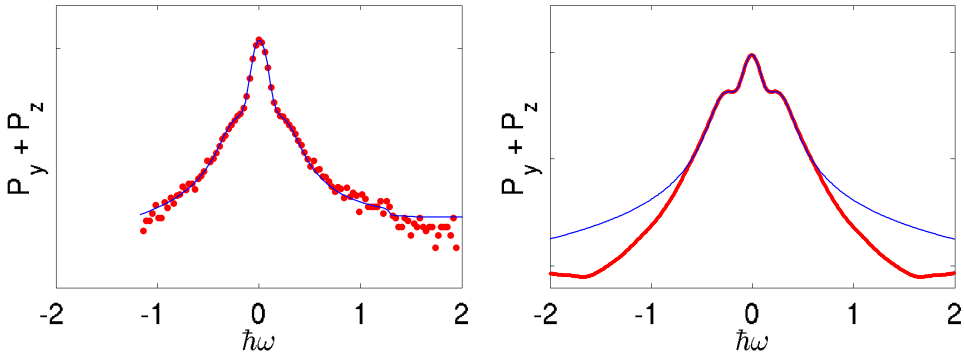

Figure 5.10: *Example fits to the experimental (left) and simulated (right) scattering spectra at 100 K. The applied fitting functions are different, but the underlying form of the signal is the same (see Fig. 5.9). Data is in red and fits in blue.*

5.2.2 Relation between fitting and simulation parameters

The four fitting parameters listed in table 5.1 are suitable for direct comparison between experiment and simulation. Of these, ε_0 is the most significant. This parameter characterizes the shoulders of the scattering spectra, and a profound experimental result is that ε_0 increases with temperature.

symbol	name
ε_0	DHO center
γ	DHO width
Γ	quasielastic width
$A = \frac{A_{\text{Bragg}}+A_{\text{CME}}}{A_{\text{CME}}}$	area fraction

Table 5.1: *Table of fitting parameters.*

To start off, a simulation scan over temperature was made using the values for B_1, B_2, B_X and N from table 2.1. The value $\lambda = 6 \cdot 10^{-4}$ should be considered arbitrary. The result is shown in Fig. 5.11. Experimental fits are indicated with red crosses, and the simulated ones are blue plusses. The

overall fitting parameter tendencies appear to be correct, but the values are only approximately right. Continued analysis will arrive at the best fit.

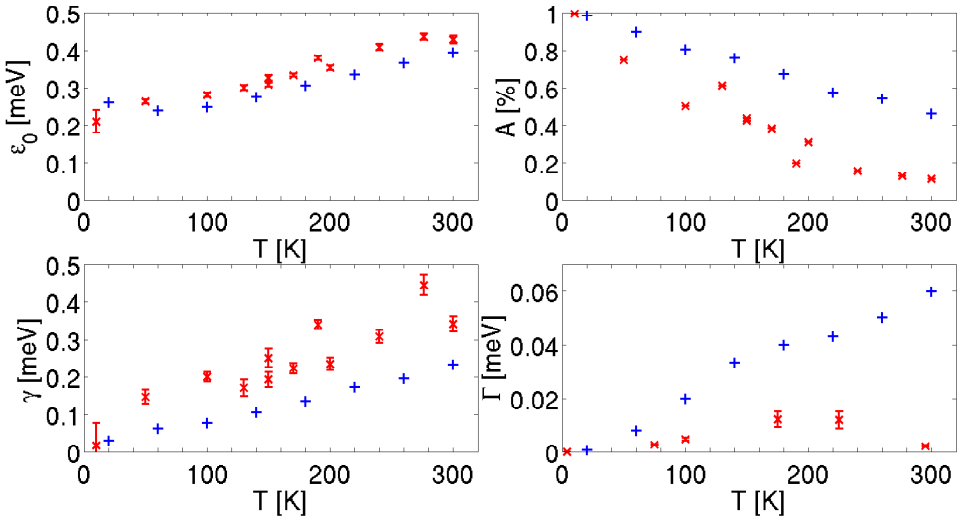

Figure 5.11: *The fitting values from table 5.1 using the naive parameter values from table 2.1 that were estimated in chapter 2.*

The following points are proposed:

– At low temperatures ε_0 corresponds to the low frequency spinwave excitations of energy ε_y. Keep in mind that the low-temperature experimental interpretation of ε_0 is measurement of ε_y.

– γ is due to thermal broadening and should therefore be proportional to λ, which has been shown to parametrize the strength of the thermal contact (see Fig. 4.7 and 4.8).

– Γ is related to random motion and superparamagnetism. A broadening of the Lorentzian is an increase of Γ. The broadening is due to increased superparamagnetic activity mixed with regular thermal broadening.

– The areas A_{Bragg} and A_{CME} measure the absolute intensity of static and dynamical states, respectively. The area faction $A = \frac{A_{\text{Bragg}}}{A_{\text{Bragg}}+A_{\text{CME}}}$ measures the fraction of static compared to dynamical states.

How far these propositions hold is a matter of investigation.

5.2.3 Dynamical fits

In the following I will focus on the parameters ε_0 and γ. The results for 50 K and 100 K are well within the experimentally understood range, and I can use those as reference points.

In chapter 3 the low frequency spinwave excitations were found to depend on the axial anisotropy parameter B_2 and the exchange parameter B_X like this:

$$\hbar\omega_x \sim \sqrt{B_1 B_X} \tag{5.4}$$

$$\hbar\omega_y \sim \sqrt{B_2 B_X} \tag{5.5}$$

If ε_0 is related to ε_y, it should depend on B_2. As can be seen from Fig. 5.12, this expectation is correct.

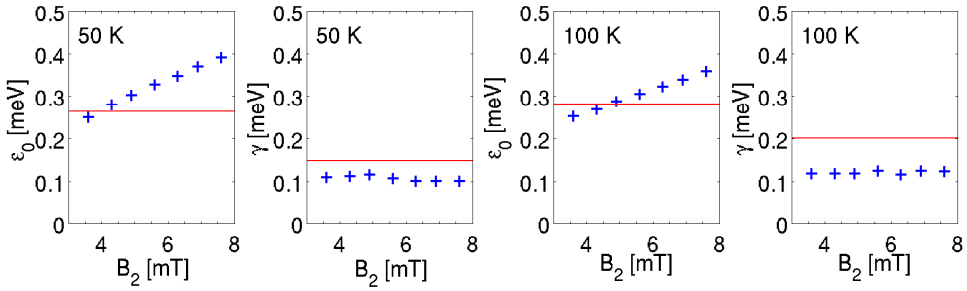

Figure 5.12: *The DHO center position ε_0 is affected by B2, which leaves the DHO width γ unaffected.*

It is likewise expected that the fitting parameter γ increases with λ, and that ε_0 does *not* depend on λ. As can be seen from Fig. 5.13 this is also practically true, but becomes questionable at higher temperatures and higher values of λ, i.e. for increasing fluctuation amplitude.

The content of Figs. 5.12 and 5.13 means that ε_0 increases with B_2 and γ increases with λ. Thus B_2 and λ are practically orthogonal, or independent, at least with respect to ε_0 and γ. This also confirms an interpretation of

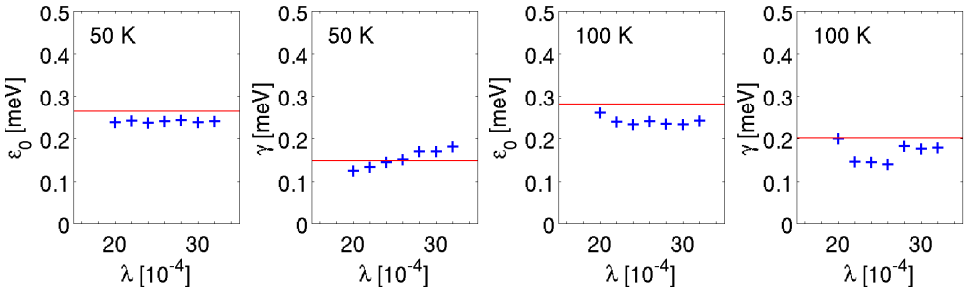

Figure 5.13: *The DHO width fitting parameter γ depends on λ as expected. Furthermore, λ hardly affects ε_0. This confirms the interpretation of λ as a non-intrinsic variable.*

ε_0 as related to the the low axial anisotropy precession mode and of γ as a measure of an non-intrinsic parameter i.e. the thermal contact.

Having established the near-orthogonality of B_2 and λ, one can return to the temperature scans and search for a better fit to experiment than Fig. 5.11. Observe a minimum of ε_0 at about 60 K. The initial decrease of ε_0 with temperature could be due to the anharmonic effect, the equivalent of Fig. 4.4d. The position of such an anharmonic effect minimum must depend on the axial anisotropy barrier height.

The low temperature values of ε_0 were not quite high enough, so the collective mode frequency should be increased. I tried increasing B_2 to obtain better fits to the $T = 50$ K and $T = 100$ K data points. The result of that simulation is shown in Fig. 5.14. Low temperature data is fitted better, but ε_0 now has a minimum at $\sim$100 K such that the development is much more flat, and higher temperature points are fitted very badly. The slope at the low temperature data points is incorrect – the simulated 50 K point is above and the 100 K point is below the corresponding experimental points. This observation strengthens my belief that the initial decrease of ε_0 at low temperatures is due to the anharmonic effect.

Discarding that adjustment to B_2 it turned out more effective to increase

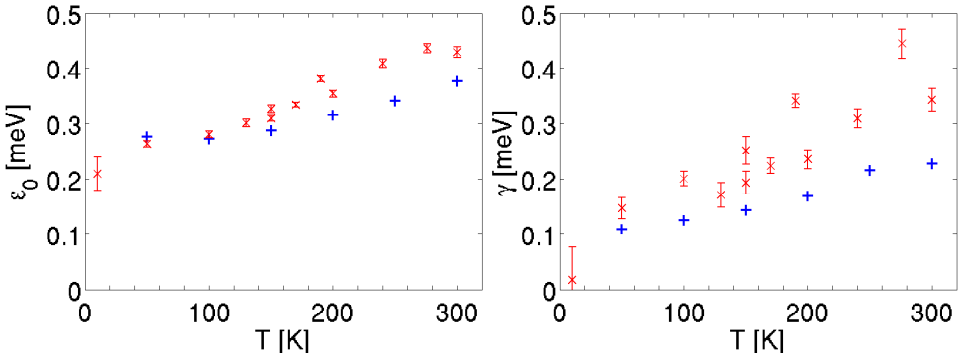

Figure 5.14: *Trial-and-error adjustment of B_2. A higher value of B_2 leads to a better low temperature fit, but the high temperature data fits get worse.*

B_X. The low frequency mode depends as much of B_X as on B_2 (see (5.5)). The position of the anharmonic minimum seems to depend on B_2, while B_X affects ε_0 equally at all temperatures. Indeed ε_0 is fitted much better using this strategy. The best fit to experiment is found in Fig. 5.15.

The simulated ε_0 values do resemble experimental values quite closely, but the simulated γ values are reduced compared to experiment. It is possible to get a better fit to γ, but then that leads to a worse fit of ε_0 (see Fig. 5.16). There is a straightforward explanation for this; inherent broadening of ε_0 due to the size distribution of nanoparticles in the sample. This gives an inherent distribution of anisotropy constants and consequently a distribution of precession frequencies, which is seen as broadening around the average.

Another problem with the best fit is the 20 K point which is far off. However, thermal activation is quite low at this temperature and the experimental data is unreliable. A stronger neutron source with a higher signal-to-noise ratio is required to settle this experimentally. (This data point indeed has a the large error-bar).

The simulation parameter values that led to the best fit in Fig. 5.15 are given in table 5.2. The only parameter that differs from its initial value in

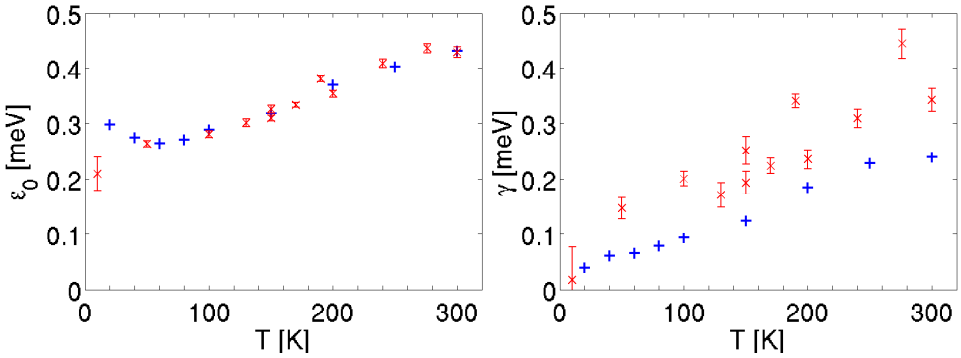

Figure 5.15: *The best fit to ε_0. The fit to γ is less than perfect.*

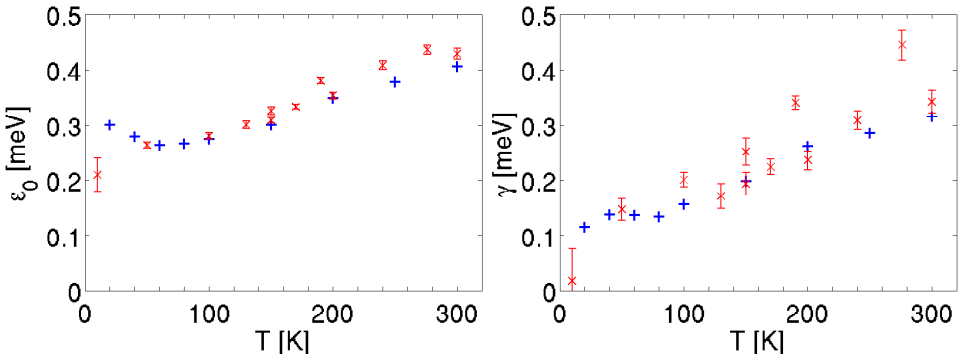

Figure 5.16: *The same values as in Fig. 5.15, but with a larger value of λ. This leads to a better fit to γ, but worse fit of ε_0.*

table 2.1is B_X.

5.2.4 Quasielastic fits

Fitting results for the width of the quasielastic Lorentzian Γ and the area fraction A are shown in this section. As mentioned above, the experimental values of Γ are those from a separate experiment on the backscattering spectrometer BSS at Jüllich.

Fig. 5.17 shows simulated values of Γ and A from the best fit of ε_0, at both the low and high value of λ. Both fits appear to be off target. Simulated values do increase, but too fast and without vanishing above 250

symbol	name	value
B_1	planar anisotropy field	-33 mT
B_2	axial anisotropy field	3.3 mT
B_X	exchange field	592 T
λ	thermal contact	$6 \cdot 10^{-4}$
κ_1	planar anisotropy constant	-15 mK
κ_2	axial anisotropy constant	1.5 mK
ZJ	exchange interaction strength	269 K

Table 5.2: *Table of the simulation parameter values that yield the best fit to experiment. The only parameter that needed adjustment compared to table 2.1 was the exchange interaction strength* $J(0) = ZJ$.

K. Notice the large λ dependency in Γ: the slopes in the two graphs are different. The overall development appears the same, however. Perhaps simulations at different values of λ only differ by a multiplicative factor. In that case the results must follow the same general law.

The parameter Γ is in [10] (and elsewhere) related to the inverse of the average flip-time:

$$\Gamma = \frac{1}{\tau} \tag{5.6}$$

and the average flip-time τ follows the Nëel-Brown law (2.10):

$$\tau = \tau_0 \exp\left(\frac{KV}{k_B T}\right) \tag{5.7}$$

where $KV = s^2 N \kappa_2$ is the axial anisotropy barrier and τ_0 depends on the system and the environment.

By varying τ_0 as a free parameter it can be seen that Γ indeed follows the Nëel-Brown law, as shown in Fig. 5.18a and 5.18c. Renormalizing to experimental data gives the result shown in Fig. 5.18b. Simulation and experiment agree nicely apart from the high-temperature point. However, this point may be an error: At 273 K ice in the sample melts and the incoherent scattering signal increases drastically. A strong incoherent peak

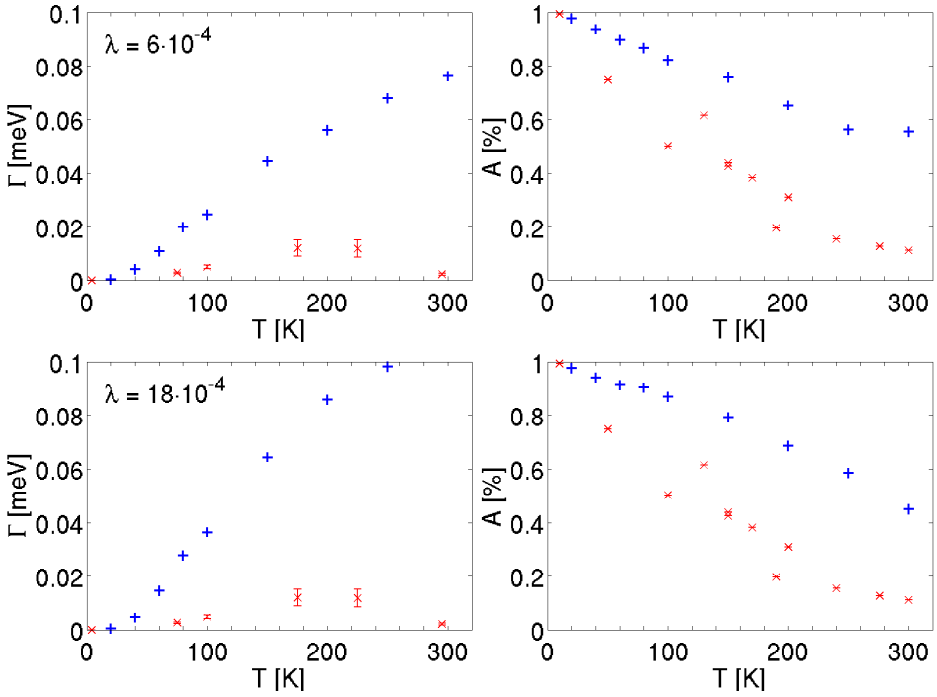

Figure 5.17: *The tendencies are correct but the fits are far from good. The same parameter values as in Fig. 5.15.*

is thus mixed with the signal and this makes the fitting process difficult and at best unreliable.

Before moving on to a discussion of the unexplained results of this chapter, a few coments on the area fraction A are in order. The pre-factor τ_0 in the Nëel-Brown law only depends on λ. Thinking of λ as the coupling strength, this means that a certain part of the quasielastic Lorentzian is due to thermal broadening and independent of the superparamagnetic activity. Likewise, the DHO width γ was connected to λ. This means that part of the area parameters A_{Bragg} and A_{CME} is due to thermal broadening and only depends on λ. Uncovering the exact dependencies might lead to a fit to A. However I have not persued this line of thought any further.

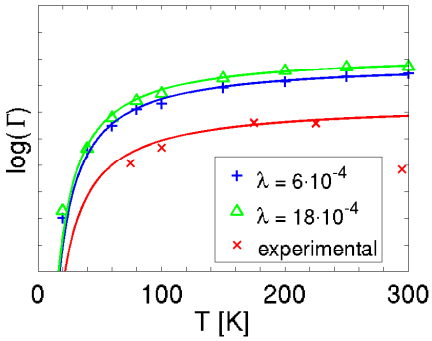

(a) log-*plot of* Γ *vs.* T*. The graphs differ only by a multiplicative factor*

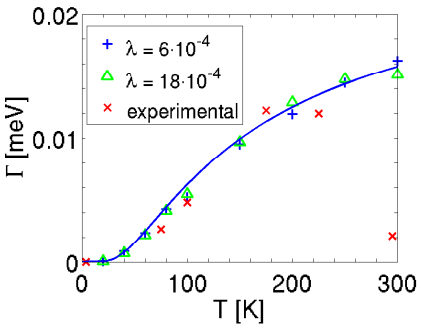

(b) *Renormalizing to experimental fits.*

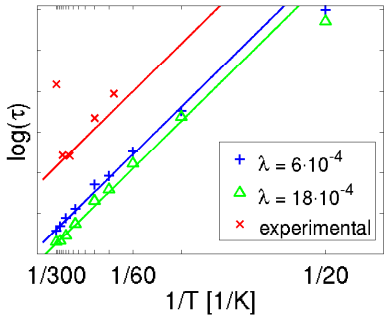

(c) *Arrhenius plot of* $\log(\tau)$ *vs.* $\frac{1}{T}$.

Figure 5.18: *Simulated values of* $\tau = \frac{1}{\Gamma}$ *follow the Nëel-Brown law (5.7), as do experimental values below 270 K. Simulation results for different* λ *differ by a multiplicative factor.*

Chapter 6

Discussion

This discussion concerns the unexplained results of chapter 5, in particular the dynamics behind the increase of ε_0 at higher temperature.

6.1 The increase of ε_0

It is important to keep in mind that the power spectrum measures resonance frequencies of the classical submagnetization system. A peak in the power spectrum corresponds to a characteristic frequency ω of the system. The stronger the intensity at ω the more often the system precesses with the frequency ω. Therefore the increase of ε_0 represents an increased probability of higher frequency precessions. These must be found somewhere in the submagnetization time evolution graphs. The reader is encouraged to look for clues in the additional time evolution examples in appendix C, and check manual observations I will make in the following.

First it will be made clear that the increase of ε_0 is not a ghost effect, but has a real physical cause.

6.1.1 Peak reflection

The motion of each submagnetization has two degrees of freedom; the spherical coordinates. However the moment is represented with 3 variables; the cartesian coordinates. This leads to a correlation between the latter. The fast, regular ripples seen in m_z (most easily seen in Fig. 5.2) are due to this correlation effect. Due to the geometry of the system, periodic motion of m_y at a frequency f gives rise to periodic ripples in m_z of frequency $2f$. The amplitude A of the ripples reflected into m_z is small: $A = |1 - \cos(\alpha)|$ where α is the amplitude of m_y. Therefore the intensity addition to the power spectrum of ripples is expected to be small.

The same type of correlation effect between m_x and m_z leads to superfast ripples in m_z. This x-z correlation is suppressed at lower temperatures because then the amplitude of m_x is quite small. Close inspection reveals that the effect is present at higher temperatures (Fig. 5.4 and 5.6), but it is barely recognizable in the figures due to it's high frequency.

The existence of reflected ripples is more easily seen by observing the low temperature power spectrum in Fig. 5.7. A very weak peak is seen in P_z at about 2.2 meV. This is two times $\hbar\omega_x$, the planar mode frequency. The 2.2 meV peak can only be a reflection peak of the planar precession mode into P_z. Similarly, the correlation of m_y and m_z accounts for the shoulders of P_z. The shoulders are most clearly seen in the 40 K plot and located around 0.5 or 0.6 meV – twice the value of $\hbar\omega_y \cong 0.3$meV. The reflection seen in P_z at 150 K appears to be located slightly below $2\varepsilon_0$, but this is expected: The most strongly reflected oscillations are those of large amplitude and these have a lower precession frequency due to the anharmonic effect.

This reflection effect could potentially account for the intensity increase at higher frequencies at temperatures above $\sim$ 150 K. However it is hard to get an idea of how weak the reflection effect really is by looking at a log plot. Therefore Fig. 5.7 has been replotted in linear scale in Fig. 6.1. It

can be seen that most of the high-frequency intensity addition to $P_y + P_z$ comes from P_y and not P_z. Since the reflection is contained in P_z it must be quite small.

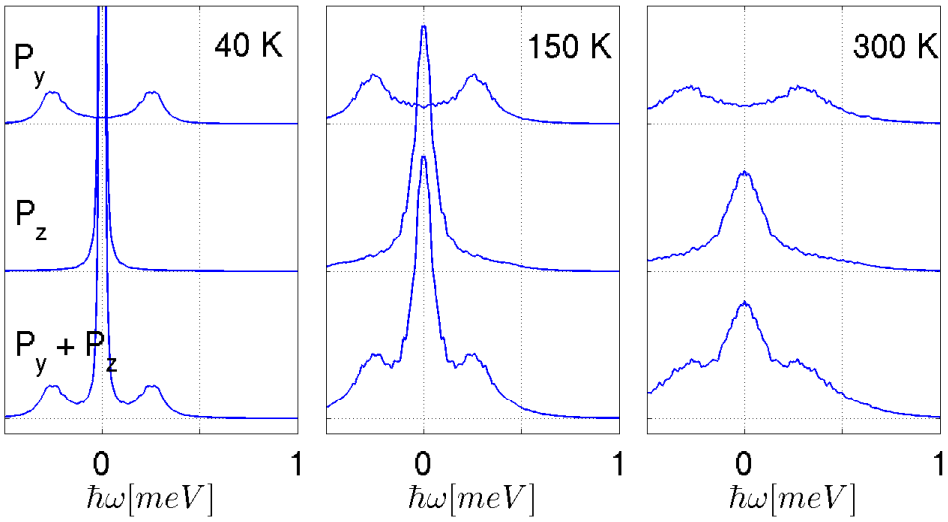

Figure 6.1: *Replot of Fig. 5.7 in linear scale. The reflection peak (the shoulders of P_z) contributes very little to the sidepeaks of $P_y + P_z$ at all temperatures. Therefore the increase of ε_0 has a primary physical cause.*

The conclusion is that the peak reflection effect can add a bit of high-frequency intensity at higher temperatures, but certainly not all. I can now with a clear counscience put the unexplained physical features in the time evolution graphs to closer inspection.

6.1.2 Double-flips

A double-flip is a superparamagnetic flip followed by an immediate return over the axial anisotropy barrier, i.e. a rapid full circle motion. Double-flips were observed in chapter 5 at temperatures as low as 60 - 80 K. A few examples are indicated by the dashed red circles in the time evolution figures at 60 K and 100 K.

Such double-flips are often accompanied by an increased submagnetiza-

tion deviation angle θ. An angle can arise due to random walk caused by the random field. In chapter 4 the connection betwee θ and exchange precessions was uncovered. According to equation (4.29) a deviation angle of $\theta = 0.5$ degrees leads to a precession frequency of $\hbar\omega = 0.46$ meV. In the present context this means that even a small angling exposes the submagnetizations to a considerable torque from the exchange field. Until the angling decays the submagnetizations may be subjected to significant transport – sometimes across the anisotropy barrier and back. However this can only happen if the angling is strong enough to breach the barrier, and therefore this effect is expected primarilly to add to frequencies above $\hbar\omega_y$.

Double flip must be a consequence of submagnetization angling because they are not present in ferromagnets. In ferromagnetic particles, superparamagnetic flips are due to random walk across the barrier (see for example [27] Fig. 1). Ferromagnetic flip events are uncorrelated which makes it highly unlikely that a flip is followed by an immediate re-flip, and this will only happen at rare occasions. On the contrary, immediate reflips are very frequent in the simulated antiferromagnetic system.

The natural conclusion of the discussion is that the motion contains two different types of superparamagnetic flips. The following two types are illustrated in Fig. 6.2:

1) Ferromagnetic flips driven by direct random walk. Submagnetizations are very close to antiparallel throughout the motion. (An example is the flips in Fig. 5.2 at 60 K from $t = 0.7$ to 0.8 ns).

2) Antiferromagnetic precession-flips driven by the exchange interaction. A submagnetization angling created by random walk is the source of the driving force in the motion. (Two of numerous examples are indicated by the dashed circles at 60 K and 100 K).

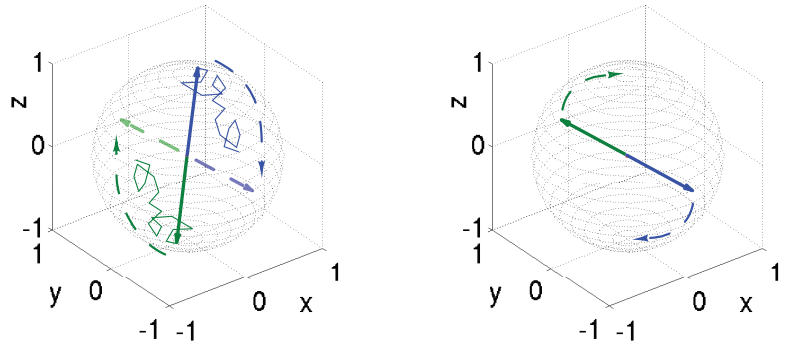

(a) *Submagnetizations simultaneously cross the anisotropy barrier due to random walk, and then relax into the potential well.*

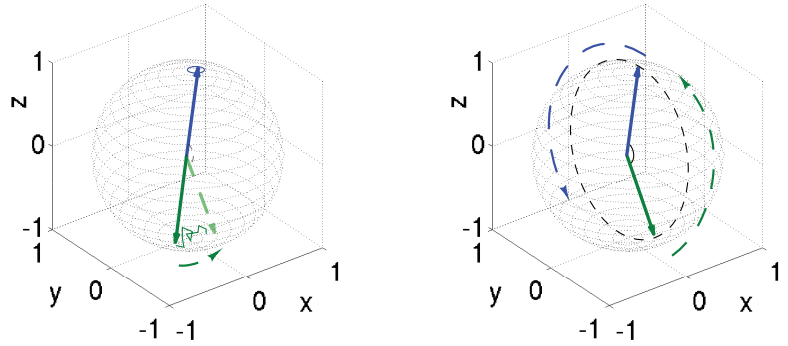

(b) *Random walk is out of sync and gives rise to an angling. Submagnetizations enter a planar precession due to the resulting torque.*

Figure 6.2: *Superparamagnetic flips can happen in two ways.*

6.1.3 2D Isotropic relaxation

Looking to higher temperatures, an additional feature appears in the time evolution graphs. This is the mentioned y-z precessions encircled by red in Fig. 5.6. Notice that in most cases θ is abnormally high – about half a degree. Once again, such an angling leads to a strong torque due to the exchange field. States that are characterized by a submagnetization angling and precessions within the basal plane will be called 2D isotropic relaxation states. The difference between double flips and isotropic relaxation is that the angling doesn't decay after one or two precessions, but leads to a

continued precession.

There are examples of a significant angle but no y-z precession. However in such cases there is often a large x amplitude. This can account for the lack of precession: at significant amplitudes out of the basal plane the planar anisotropy energy grows significantly because $B_1 \cong 10B_2$. The exchange angling would have to be exceptionally high to breach the *planar* barrier – about 5 degrees – and such a high angling was never observed.

6.2 Correlation between θ and higher frequency precessions

In order to quantitatively investigate the ideas explained above, a correlation between higher frequency precessions and θ must be shown to exist. Define the θ-correlation function as

$$P_{\theta i} = |m_i(\hat{t})\theta(t)|^2. \tag{6.1}$$

P_θ can be thought of as an trajectory frequency average weighted by θ. Consider the correlation spectrum $P_\theta = P_{\theta y} + P_{\theta z}$ compared to $P = P_y + P_z$. If θ is indeed largest at those times when the higher frequency contributions to P above ω_y are created, then those bits of motion are weighted more strongly by θ than other bits. Likewise, trajectories with θ close to zero are repressed. If such tendencies are reflected in the correlation power spectrum P_θ it should peak around higher frequencies and show a repression of intensity at lower frequencies.

It is clear from Fig. 6.3 that there is a bias for high frequency precessions at non-zero θ. The low temperature spectra may be complicated to interpret, but the information contained in P_θ is most interesting at higher temperatures. Here the bulk of the intensity area of P_θ is found beyond $\hbar\omega_y \cong 0.3$meV. Therefore the general point of view presented in this discussion must be correct. Further detailed analysis was not conducted.

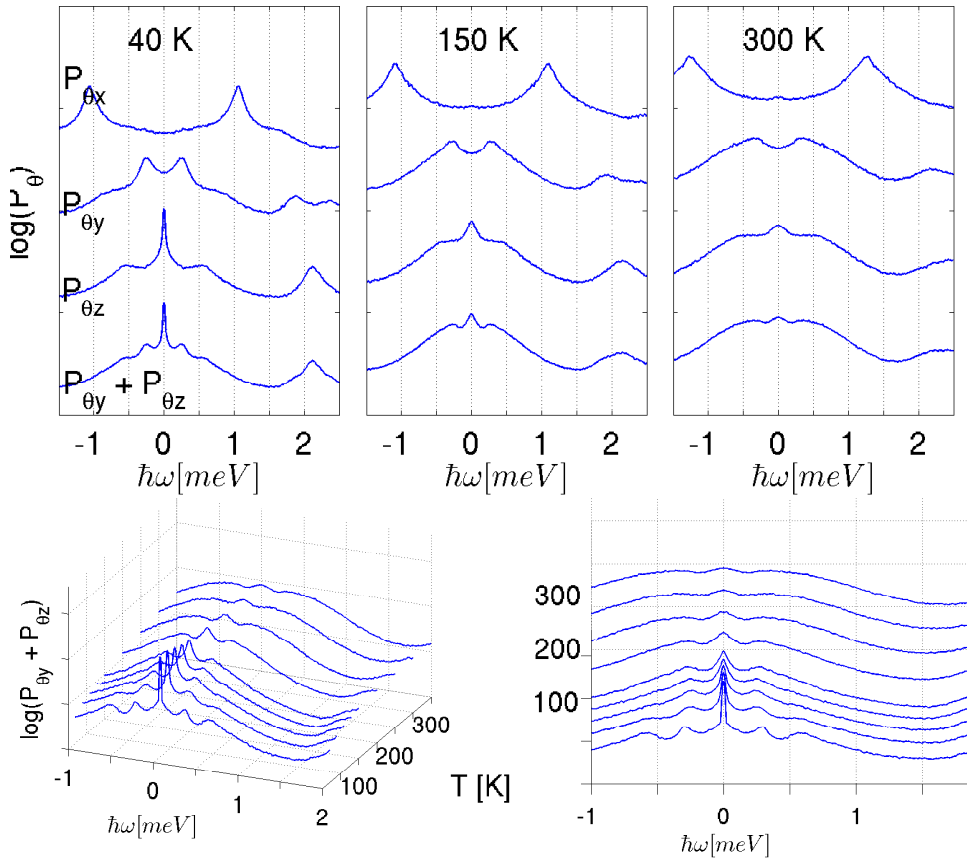

Figure 6.3: *Correlation between the deviation angling θ and the simulated power spectrum. At temperatures above ∼150 K, P_θ peaks at values beyond $\hbar\omega_y$. Compare to Fig. 5.7 and 5.8.*

Chapter 7

Summary and conclusion

Studies of fine particles of magnetic materials have been conducted for over half a century. Very often the magnetic dynamics of such particles differ significantly from that of bulk crystals, due to finite-size effects and surface effects. Among these we find the important effect of size-quantization of spinwaves in magnetic nanoparticles. The spinwave spectrum is quantized and the collective motion of aligned ionic spins is isolated from the higher spin dynamics. This means that the dominating collective dynamics behaves, and can be studied, independently.

In ferromagnetic materials the collective moment has one or more preferred directions due to anisotropy energies. The collective dynamics typically includes precession modes about the anisotropy energy minima, and thermally excited superparamagnetic flips across the anisotropy energy barrier of size KV.

Recently nanoparticles of hematite (the iron-oxide α-Fe_2O_3) below 50 nm have been a subject of investigation. Hematite is an antiferromagnet with two sublattices that give rise to magnetic moments of the total combined spins of each sublattice. Since the submagnetizations align antiparallel, they cause almost no external field. Hematite is complex but the dynamics is known to be dominated by the effect of the inter-sublattice coupling, and

the planar and axial crystal anisotropies.

Inelastic neutron scattering experiments of 15 nm hematite nanoparticles revealed that the moments were indeed confined to the basal plane by a strong planar anisotropy. Withing the basal plane the submagnetizations performed collective precessions in the axial anisotropy. The precession frequency was measured to decrease slightly with temperature and this was explained by an anharmonic effect – as the temperature rises the precession amplitude increases into the anharmonic range of the anisotropy field. A high-frequency planar anisotropy precession was also observed. These observations satisfied the condition $k_BT < KV$ of the Nëel-Brown law (2.10) in the low temperature limit, and this law did describe the observed superparamagnetism.

Further experiments on 7-11 nm hematite particles went beyond the low-temperature limit, as the anisotropy barrier in an 8 nm particle is about 140 K. Instead of a weak decline of the axial precession mode, a significant increase of the corresponding peak in the scattering spectrum was observed. This increase was as high as 50% at 300 K. Although the crystal anisotropies of hematite are highly dependent on size and temperature, and the values are unknown for 8 nm hematite, such an increase of the planar anisotropy with temperature is unprecedented and thus unlikely. A high frequency mode was not observed, so the strength of the planar anisotropy is unknown.

All this was explained in chapter 2. Below 150 K the 8 nm hematite data has been explained and published using the 15 nm model. However it was an open question weather the unexplained higher temperature results could be understood from the viewpoint of the classical model of two submagnetizations coupled by exchange and exposed to planar and axial anisotropies. The task of the present thesis has been to answer this question by applying the method of Langevin dynamics and using numerical methods to simulate a representation of the nanoparticle system. The norm square of the

Fourier transform of the trajectories of the basal plane components of either of the submagnetization, could be compared to scattering data. This was valid for long simulation times such that the resulting set of trajectories was statistically representative.

Using the spinwave description of the low temperature collective dynamics as a starting point and for reference, a classical equation of motion for the submagnetizations was found. This equation of motion had the well-known form that describes precession of a magnetic moment in a field, and was thus readilly generalized into a Langevin equation. The Langevin equation models dissipation by means of a damping term and fluctuation by means of a random variable. The statistical properties of this random variable was determined such that the resulting fluctuation and dissipation corresponded to that of a generic heat bath.

By the end of the theory chapter it was reallized that the difference in collective dynamics of nanoparticles of different sizes was simple: Particles differ in values (and temperature dependencies) of the exchange- and anisotropy constants, and in the temperatures scale.

A numerical method was introduced and validated in chapter 4. The equation of motion was seen to yield the correct analytical precession frequencies at low amplitudes, and the anharmonic effect was observed under controlled circumstances by increasing the amplitude. Most important was the temperature implementation and the illustration of convergence of the power spectra of trajectories.

The simulations have two aspects: First the visualization of physically realistic trajectories or histories for the submagnetization motion. Second, the averaged power spectra obtained by simulating a statistically representative set of trajectories.

The application of model and numerical method to the 8 nm nanoparticle system was presented in chapter 5. Direct observations were made:

Time evolutions of the cartesian coordinates of one submagnetization, along with the deviation angle from antiparallel between submagnetizations was observed. At low temperatures the results were straightforward to interpret: Although an antiferromagnet, the system behaved like a classical ferromagnetic superparamagnet which lives in a world of anisotropy precessions and superparamagnetic flips. However, at slightly higher temperatures, around 80 K, the system started performing double-flips. These were flips from $m_z \cong 1$ to $m_z \cong -1$ followed by an *immediate* reflip. Statistically such flips happen very rarely in ferromagnetic superparamagnets. At higher temperatures (from 150 K and up) the double flips became much more frequent, and even extended to regular precessions within the basal plane. I claimed that such precessions were often accompanied by an abnormally high angling, sometimes up to 1 degree. Usually the angling fluctuates at some value below 0.5 degrees.

Regardless of these observations, the simulations were quantified by taking the averaged simulated scattering spectrum. Simulation results were not fitted directly to experiment, but rather the same fitting method was applied to simulations as had previously been used to fit experimental data. The fitting function was a "quasielastic" Lorentzian added to a damped harmonic oscillator which gives a sidepeak. This gives a strong central peak and distinct sidepeaks parametrized by the position ε_0, and width γ.

After a trial-and-error adjustment of simulation parameter values the simulations were found to agree with experiment (see Fig. 5.15). The initial choice of parameter values were those of the 15 nm sample, but with a value $\kappa_2 = \frac{1}{10}|\kappa_1|$ for the axial anisotropy, turned out to fit experiment. The bulk value for the exchange field turned out to be too low and an enhanced value was determined. This means that the nanoparticles are fit by the "strongly planar case" model, in which the surface effect of uncompensated moments has been shown to influency dynamics weakly weakly. The simulated side-

peak position ε_0 showed an initial decrease contrary to experiment, followed by an increase from ∼100 K that fits the experiment. The decrease was theoretically accounted for by the mentioned anharmonic effect. The 5 K data point that was in disagreement, was discredited due to experimental difficulties at this temperature. Furthermore, the simulated initial decrease of ε_0 was in agreement with 15 nm nanoparticle data which showed a slight decrease up to 300 K. As mentioned above, the large difference in the number of sites of the two nanoparticle sizes can account for this difference in temperature scale.

The width of the fitting Lorentzian is inversely proportional to the superparamagnetic flip expectation time τ. In spite of the fact that $k_BT \sim KV$ rather than $k_BT < KV$, values for τ were shown to follow the Nëel-Brown law (2.10). The pre-factor τ_0 depended on λ, but an exact dependency was not determined. The experimental data also followed this law, as long as one disregards the high temperature point close to 300 K. The fits of this point may have been disturbed by strong incoherent scattering of water in the sample which melts at this temperature.

Conclusion

Since the simulations fit experiment, the increase of ε_0 must be due to high frequency precessions found in the time evolution graphs. A brief discussion in chapter 6 of the ripples seen in the time evolutions decided that the increase was due to a physical effect. The previously observed double-flips and y-z precessions seen at higher temperatures were investigated in more detail. This investigation lead to the introduction of two different types of superparamagnetic flips: Ferromagnetic flips and exchange driven antiferromagnetic flips. All features in the time evolution graphs could now be classified as one of the following: Anisotropy precession modes, reflected ripples, random walk, and exchange driven flips/precessions.

The interpretation of the experimental observations is based on observations of simulated trajectories and contained in Fig. 6.2. Random walk gives rise to a deviation angle that causes the submagnetizations to precess within the basal plane untill the angle decays. Such precessions can be classified as 2-D isotropic relaxaton. If the orientation is such as to precess perpendicular to the basal plane, the planar anisotropy deflects the precession before it arises. The exchange-driven precessions can have a continuum of frequences, depending on the deviation angle θ. At higher temperatures it becomes increasingly probably that these precession modes arise. The occupation of higher frequency precession modes is reflected in the scattering spectra as an increased intensity at these higher frequencies. The validity of this claim was increased by the correlation between the angling θ and higher frequency precessions, seen in Fig. 6.3.

The antiferromagnetic parallel to the Nëel-Brown law has never been derived, because of the complexity of the problem: the antiferromagnetic system contains four degrees of freedom rather than two. The problem is related to random walk in a complicated four dimensional potential of anisotropies and exchange. However complicated, the simulated submagnetization trajectories can visualized, which is something that is not yet technically possible to do experimentally. Hopefully the results and visualizations of this thesis can be used to shed some light on antiferromagnetic superparamagnetism in general.

Outlook

Disregarding the two datapoints that do not fit the general picture, simulations are in agreement with experiment and the model presented in this thesis can be used to investigate similar nanoparticle systems.

It was suggested in [13] that the planar and axial anisotropies should be of the same order of magnitude, in which case the surface effect of uncom-

pensated moments gives a significant reduction to the precession frequencies. Therefore this situation is of particular interest and could be simulated.

Othewise, one could simulate the effect of the heat bath coupling on the pre-factor τ_0 in the Nëel-Brown law. Such numerical information could hint at an analytic dependency sought by Steen Mørup. Moreover, one could simulate a sample with a size distribution of particles, or further investigate correlation functions such as P_θ.

Appendix A

Wiener-Khintzhine proof

Suppose the simulated or real-life experiment starts at time 0 and continues till time T, which is large compared to all characteristic times of the system.

Let

$$S_{\alpha\alpha} = \int_0^T dt\ e^{i\omega t} < S_\alpha(0) S_\alpha(t) > \tag{A.1}$$

be the spin correlation function where S_α is the superspin of either sublattice. Define the Fourier transform on the interval $[0, T]$ as

$$\hat{S_\alpha}(\omega) = \frac{1}{\sqrt{T}} \int_0^T dt\ e^{i\omega t} S_\alpha(t) \tag{A.2}$$

where ω are the finite frequencies of the discrete Fourier transform. The power spectrum is the norm square of the Fourier transform:

$$P_\alpha(\omega) = |\hat{S_\alpha}(\omega)|^2. \tag{A.3}$$

Then the Wiener-Khintzhine theorem states that the averaged power spectrum only differs from the spin correlation function by a constant factor:

$$< P_\alpha > \sim S_{\alpha\alpha}. \tag{A.4}$$

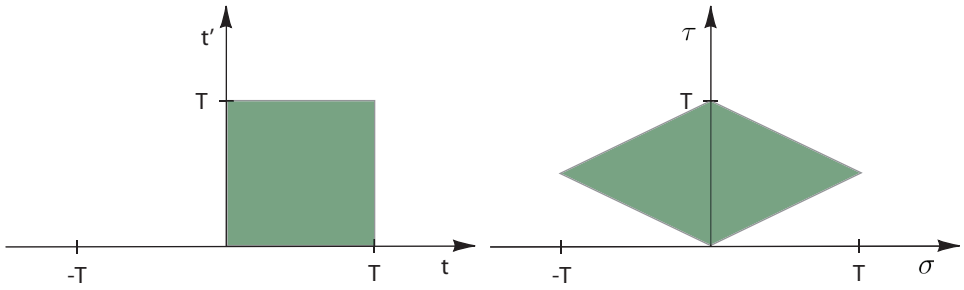

Figure A.1: Integration area $A = T^2$ drawn in the (t, t') plane, and the new variables (σ, τ).

The proof follows by calculating the left-hand side of A.4:

$$< P_\alpha > = < \frac{1}{\sqrt{T}} \int_0^T dt\ e^{i\omega t} S_\alpha(t) \frac{1}{\sqrt{T}} \int_0^T dt' e^{-i\omega t} S_\alpha(t') > \quad \text{(A.5)}$$

$$= \frac{1}{T} \int_0^T \int_0^T dt dt'\ e^{i\omega(t-t')} < S_\alpha(t) S_\alpha(t') > \quad \text{(A.6)}$$

$$\quad \text{(A.7)}$$

Introduce the relative and center-of-mass coordinates,

$$\sigma = t - t' \qquad \tau = \frac{t + t'}{2} \quad \text{(A.8)}$$

such that

$$t = \sigma + 2\tau \qquad t' = \sigma - 2\tau. \quad \text{(A.9)}$$

The new integration area is the subset of the σ, τ plane shown in Fig. A.1.

Substitution gives

$$< P_\alpha > = \frac{1}{T} \int \int_A d\sigma d\tau\ e^{i\omega\sigma} < S_\alpha(\sigma + 2\tau) S_\alpha(\sigma - 2\tau) > \quad \text{(A.10)}$$

$$= \frac{1}{T} \left(\frac{1}{2} \int_{-T}^{T} d\sigma \int_0^T d\tau \right)\ e^{i\omega\sigma} < S_\alpha(2\tau) S_\alpha(-2\tau) > \quad \text{(A.11)}$$

$$= \frac{1}{2} \frac{2T}{T} \int_0^T d\tau\ e^{i\omega\sigma} < S_\alpha(2\tau) S_\alpha(-2\tau) > \quad \text{(A.12)}$$

$$= \frac{1}{4} \int_0^T d\tau'\ e^{i\omega\sigma} < S_\alpha(0) S_\alpha(\tau') > \quad \text{(A.13)}$$

$$\quad \text{(A.14)}$$

which is the right hand side of A.4.

It was nesseccary to use

$$< S_\alpha(\sigma + 2\tau)S_\alpha(\sigma - 2\tau) > \quad = \quad < S_\alpha(2\tau)S_\alpha(-2\tau) > \qquad \text{(A.15)}$$

and

$$< S_\alpha(2\tau)S_\alpha(-2\tau) > \quad \rightarrow \quad 0 \quad \text{for } \tau \text{ large} \qquad \text{(A.16)}$$

Appendix B

MATLAB code

The most relevant MATLAB code is found in this appendix. Figure scripts and subroutines are not included. Please email jakob.garde@gmail.com for further details.

B.1 Scan setup

```
%%%%%%%%%%%%%%%%%%%%%%%%%%%%%%%%%%%%
```

—— physical constants —- %%

```
%%%%%%%%%%%%%%%%%%%%%%%%%%%%%%%%%%%%

k_B = 1.38065e-23;
hbar = 1.05459e-34;
meV = 1.602e-22;
g = 2.002;
mu_B = 9.274e-24;

gamma = - g*mu_B/hbar;


%%%%%%%%%%%%%%%%%%%%%%%%%%%%%%%%%%%%
```

—— model parameters —— %%

```
%%%%%%%%%%%%%%%%%%%%%%%%%%%%%%%%%%%%
```

```
N_total = 10595;
xi = 1;
N_A = N_total/(1 + xi);
N_B = N_total/(1 + 1/xi);

T_unit = 1;
lambda_unit = 0.0001;

kappa1_unit = - 15e-3*k_B;
kappa2_unit = 15e-4*k_B;
ZJ_unit = 207*k_B;

S = sqrt((5/2)*(5/2+1));
M_A = N_A*g*mu_B*S;
M_B = N_B*g*mu_B*S;

B_X_unit = 1 * (ZJ_unit*S)/(g*mu_B);          % exchange
B_1_unit = 1 * (kappa1_unit*S)/(g*mu_B);      % planar anisotropy
B_2_unit = 1 * (kappa2_unit*S)/(g*mu_B);      % axial anisotropy
B_ext = 0 * [0 0 1]';                         % external field

% display field values and start time:
display(['B_X = ' num2str(B_X_unit) ' T, B_1 = ' num2str(B_1_unit) ...
    ' T, B_2 = ' num2str(B_2_unit) ' T, B_ext_z = ' ...
    num2str(B_ext(3)) ' T'])
c = clock;
display([num2str(c(4)) ':' num2str(c(5))])
display(sprintf('\n')) % display new line

%%%%%%%%%%%%%%%%%%%%%%%%%%%%%%%%%%%
```

```
B_X = 455.3306 T, B_1 = -0.032995 T, B_2 = 0.0032995 T, B_ext_z = 0 T
11:59
```

– simulation controls ——- %%

```
%%%%%%%%%%%%%%%%%%%%%%%%%%%%%%%%%%%

N = 1e6;                % integration length
dt = 1e-14;             % stepsize [s]
```

```
save_boolean = 1;       % save the scan for later use, if save == 1

RunCopies = 6;          % number of repetitions of each run.
% Convergence typically achieved after about 60ns, sooner at strong damping
location = 2;           % 1: local, 2:/scratch/garde/MATLAB_scans
scheme_nb = 2;          % algorithm incarnation

scanNB = 1;
scanType = 1;           % scan types are: 1-T; 2-lambda; 3-kappa2;
% 4-"other"(dont use)
B1_Tdep_boolean = 1;    % if set to 1, the value of B1 is adjusted
% according to the T-dep of 15 nm part. in Klausen '04.

FFT_res = 0;            % fft resolution. Set = 0 for no auto fft
fft_boolean = 0;        % used for validation scans (auto fft)(outdated).
if fft_boolean==0, FFT_res = 0;end;

plot_boolean = 0;       % plot_quick.m plots trajectory
% (and fft if it exists) (outdated)
dataspacing = 100;      % plot only every [dataspacing] points (outdated)
```

scan limits: %%%%

```
%%%% XXX_array = (start_point:step_size:end_point)*[value].
% Only scan a single variable!

T_array = (50:50:300) * T_unit;
lambda_array = (18:2:18) * lambda_unit;
B_2_array = (1.3:0.2:1.3) * B_2_unit;

%%%% initial rotations [degrees].
% phi rotates around z, teta around the new x axis.

phiA = 90;
tetaA_array = 10*(1:5:1);
tetaA = tetaA_array(1);
phiB = 90;
tetaB = -10;

teta_sync = 1;       % if == 1, tetaB := tetaA before each scan iteration

initial_angles = [...
                  phiA tetaA
                  phiB tetaB];
```

```
%%%%
%%%%

B_X_array = (1:1:1) * B_X_unit;
B_1_array = (1:1:1) * B_1_unit;

kappa1_array = (1:1:1) * kappa1_unit;
kappa2_array = (1:1:1) * kappa2_unit;

%%%%
```

set fluctuating field variance and std. dev. :

```
D_A_array =  2 .* lambda_array * k_B .* T_array * dt / (-gamma * M_A);
D_B_array =  2 .* lambda_array * k_B .* T_array * dt / (-gamma * M_B);
sigma_A_array = sqrt(D_A_array);
sigma_B_array = sqrt(D_B_array);


%%%%%%%%%%%%%%%%%%%%%%%%%%%%%%%%%%%%
```

scan initialize

```
it0 = size(B_X_array);                                  % J scan
it1 = size(B_1_array);                                  % kappa1 scan
it2 = size(B_2_array);                                  % kappa2 scan
it3 = size(T_array);                                    % temp scan
it4 = size(lambda_array);                               % lambda scan
it5 = size(tetaA_array);                                % tetaA scan

iterations_m = it0(1,2);                                    % kappa1 scan
iterations_i = it1(1,2);                                    % kappa1 scan
iterations_j = it2(1,2);                                    % kappa2 scan
iterations_k = it3(1,2);                                    % temp scan
iterations_l = it4(1,2);                                    % lambda scan
iterations_h = it5(1,2);                                    % tetaA scan

E_array = zeros(2,iterations_m,iterations_i,iterations_j, ...
    iterations_k,iterations_l,iterations_h);

figs_array = ones(iterations_i,iterations_j,iterations_k,iterations_l);
```

```
%%%%%%%%%%%%%%%%%%%%%%%%%%%%%%%%%%

———— scan ————- %%

%%%%%%%%%%%%%%%%%%%%%%%%%%%%%%%%%%


% name the current scan and save the scan globals

% make scan ID string:
if save_boolean == 1
[filename scanStrOld] = makeRunFileName(scanNB,4,0,0);


    switch location
        case 1
            dirname = ['/home/garde/MATLAB_scans/' scanStrOld];
        case 2
            dirname = ['/scratch/garde/MATLAB_scans/' scanStrOld];
        otherwise
            display('location case error')
    end;

    mkdir(dirname);                                % create scan directory
    save([dirname '/' scanStrOld '_sim_globals'], ... % save scan globals
        'B_X_array', 'B_1_array', 'B_2_array', 'B_ext', ...
        'T_array', 'lambda_array', ...
        'D_A_array', 'D_B_array', 'initial_angles', 'tetaA_array',...
        'N_total', 'xi', 'M_A', 'M_B',...
        'dt', 'N', 'FFT_res');
end

% Scan iteration loop:

for m = 1:iterations_m
   for i = 1:iterations_i
       for j = 1:iterations_j
           for k = 1:iterations_k
               for l = 1:iterations_l
                   for h = 1:iterations_h

sigma_A = sigma_A_array(k*l);
sigma_B = sigma_B_array(k*l);
lambda = lambda_array(l);
```

```
T = T_array(k);

B_1 = B_1_array(i);
B_2 = B_2_array(j);
B_X = B_X_array(m);

if B1_Tdep_boolean == 1
    B1_TdepMult = ((-8.9e-8)*T^2 - 15e-3)*k_B*S/(g*mu_B)/B_1;
        % kappa_1 temperature dependency
    B_1 = B_1*B1_TdepMult;
end

switch scanType
    case 1, runValue = T;
    case 2, runValue = lambda;
    case 3, runValue = B_2;
    otherwise, runValue = 0;
end

tetaA = tetaA_array(h);
if teta_sync, tetaB = tetaA; end;
initial_angles = [...
    phiA tetaA
    phiB tetaB];

% display values of current iteration to workspace.

display(['T = ' num2str(T) ', lambda = ' num2str(lambda) ...
    ', B1 = ' num2str(B_1) ', B2 =' num2str(B_2)])

% do the integration and return time evolution, and save
% the results to disk. Repeat the sim repeat_nb times

for partNB = 1: RunCopies

    switch scheme_nb
        case 1
            display(['i = ' num2str(i*j*k*l*h) ', T = ' num2str(T)])
            [m_A m_B t] = integrate(initial_angles,B_1,B_2,B_X,B_ext, ...
                sigma_A,sigma_B,lambda,T,N,dt);
            c = clock;
            display([num2str(c(4)) 'h' num2str(c(5)) 'min'])
        case 2
            display(['i = ' num2str(i*j*k*l*h) ', T = ' num2str(T)])
```

```
            [m_A m_B t] = integrate_2(initial_angles,B_1,B_2,B_X, ...
                B_ext,sigma_A,sigma_B,lambda,T,N,dt);
            c = clock;
            display([num2str(c(4)) 'h' num2str(c(5)) 'min'])

        case 3
            display(['lambda = ' num2str(lambda) ':'])
            [m_A m_B t] = integrate_3(initial_angles,B_1,B_2,B_X, ...
                B_ext,sigma_A,sigma_B,lambda,T,N,dt);
            analysis_langevin(M_A,B_ext(3),T,m_A)
        otherwise
            display('algorithm case error')
    end

    % save the simulation:
    if save_boolean == 1


        [filename scanStr runStr partStr] = makeRunFileName(scanNB, ...
            scanType,runValue,partNB);
        filename = [scanStrOld '_' runStr '_' partStr];
        save([dirname '/' filename], 'm_A', 'm_B', ...
            'B_X', 'B_1', 'B_2', 'B_ext', ...
            'N', 'dt', 'T', 'lambda');
    end

end

% do a shallow fft and plots

if fft_boolean == 1
    [t E_vector X Y Z E_t E_x E_y NFFT] = analysis_quick(FFT_res, ...
        dataspacing,m_A,m_B,lambda,T,N,dt,B_1,B_2,B_X);
    E_array(1,m,i,j,k,l,h) = E_x;
    E_array(2,m,i,j,k,l,h) = E_y;

    % save the results
    if save_boolean == 1
        save([dirname '/' simID], ...
            't', 'E_vector', 'E_x','E_y', ...
            'X', 'Y', 'Z', 'E_t', ...
            'NFFT', ...
            '-append');
    end
```

```
end

if plot_boolean == 1
    plot_quick(FFT_res,dataspacing,m_A,m_B,lambda,T,N,dt,B_1,B_2,B_X);
end

                    end;
                end;
            end;
        end;
    end;
end;

% save fft's

if save_boolean == 1
    save([dirname '/' scanStrOld '_sim_globals'], 'E_array', '-append');
end

display(sprintf('\n')) % new line
```

B.2 Integration

```
%%%%%%%%%%%%%%%%%%%%%%%%%%%%%%%%%%%%
```

—— function declaration %%%%%%%%%

```
%%%%%%%%%%%%%%%%%%%%%%%%%%%%%%%%%%%%
```

```
function [m_A m_B t] = integrate_2(angles,B_1,B_2,B_X,B_ext, ...
    sigma_A,sigma_B,lambda,T,N,dt)



%%%%%%%%%%%%%%%%%%%%%%%%%%%%%%%%%%%%
```

—— physical constants ———%%

```
%%%%%%%%%%%%%%%%%%%%%%%%%%%%%%%%%%%%

k_B = 1.38066e-23;
hbar = 1.05459e-34;
meV = 1.602e-22;
g = 2.002;
```

```
mu_B = 9.274e-24;

gamma = - g*mu_B/hbar;



%%%%%%%%%%%%%%%%%%%%%%%%%%%%%%%%%%%%%%%%
```

——— initial conditions ——— %%

```
%%%%%%%%%%%%%%%%%%%%%%%%%%%%%%%%%%%%%%%%

% in terms of  Euler rotations:
% rotate phiS / phiT degrees about the z axis,
% then tetaS / tetaT degrees about the (new) x axis
% S and T refer to the macro-spins of each sublattice.
%%%%%%%%%%%%%%%%%%%%%%%%%%%%%%%%%%%%%%%%
% m_A and m_B are 3 x N arrays. Each row is a time point

phiA = angles(1,1)*2*pi/360;
tetaA = angles(1,2)*2*pi/360;

phiB = angles(2,1)*2*pi/360;
tetaB = angles(2,2)*2*pi/360;

DA = [ ...
    cos(phiA) sin(phiA) 0
    -sin(phiA) cos(phiA) 0
    0 0 1];

DB = [ ...
    cos(phiB) sin(phiB) 0
    -sin(phiB) cos(phiB) 0
    0 0 1];

CA = [ ...
    1 0 0
    0 cos(tetaA) sin(tetaA)
    0 -sin(tetaA) cos(tetaA)];

CB = [ ...
    1 0 0
    0 cos(tetaB) sin(tetaB)
    0 -sin(tetaB) cos(tetaB)];
```

```
m_A = zeros(3,N);
m_A(:,1) = DA*CA*[0,0,1]';

m_B = zeros(3,N);
m_B(:,1) = DB*CB*[0,0,-1]';

% make the time vector (for plotting):

t = (1:N)*dt;

%%%%%%%%%%%%%%%%%%%%%%%%%%%%%%%%%%%%
```

————————- Integration ——— %%

```
%%%%%%%%%%%%%%%%%%%%%%%%%%%%%%%%%%%%

if T == 0                           % deterministic integration:

    for j = 1:N/100

        for i = (j-1)*100+1 : j*100;

            B_eff_A = - B_X * m_B(:,i) + 2 * [B_1,0,B_2]'.* m_A(:,i) ...
                + B_ext;
            B_eff_B = - B_X * m_A(:,i) + 2 * [B_1,0,B_2]'.* m_B(:,i) ...
                + B_ext;

            k1_m_A = gamma * cross(m_A(:,i),B_eff_A)* dt + lambda ...
                * gamma * cross(m_A(:,i),cross(m_A(:,i),B_eff_A))* dt;
            k1_m_B = gamma * cross(m_B(:,i),B_eff_B)* dt + lambda ...
                * gamma * cross(m_B(:,i),cross(m_B(:,i),B_eff_B))* dt;

            B_eff_A_2 = - B_X * (m_B(:,i) + k1_m_B) + 2 * [B_1,0,B_2]' ...
                .*(m_A(:,i) + k1_m_A) + B_ext;
            B_eff_B_2 = - B_X * (m_A(:,i) + k1_m_A) + 2 * [B_1,0,B_2]' ...
                .*(m_B(:,i) + k1_m_B) + B_ext;

            k2_m_A = gamma * cross(m_A(:,i) + k1_m_A,B_eff_A_2)* dt ...
                + lambda * gamma * cross(m_A(:,i) + k1_m_A, ...
                cross(m_A(:,i) + k1_m_A,B_eff_A_2)) * dt;
            k2_m_B = gamma * cross(m_B(:,i) + k1_m_B,B_eff_B_2)* dt ...
                + lambda * gamma * cross(m_B(:,i) + k1_m_B, ...
                cross(m_B(:,i) + k1_m_A,B_eff_B_2)) * dt;
```

```
            m_A(:,i+1) = m_A(:,i) + 1/2*k1_m_A + 1/2*k2_m_A;
            m_B(:,i+1) = m_B(:,i) + 1/2*k1_m_B + 1/2*k2_m_B;

        end;

    end;

else                                    % including random term:


    for j = 1:N/100

        for i = (j-1)*100+1 : j*100-1;

            B_eff_A = - B_X * m_B(:,i) + 2 * [B_1,0,B_2]'.* m_A(:,i) ...
                + B_ext;
            B_eff_B = - B_X * m_A(:,i) + 2 * [B_1,0,B_2]'.* m_B(:,i) ...
                + B_ext;

            k1_m_A = gamma * cross(m_A(:,i),B_eff_A)* dt + lambda ...
                * gamma * cross(m_A(:,i),cross(m_A(:,i),B_eff_A))* dt;
            k1_m_B = gamma * cross(m_B(:,i),B_eff_B)* dt + lambda ...
                * gamma * cross(m_B(:,i),cross(m_B(:,i),B_eff_B))* dt;

            B_eff_A_2 = - B_X * (m_B(:,i) + k1_m_B) + 2 ...
                * [B_1,0,B_2]'.*(m_A(:,i) + k1_m_A) + B_ext;
            B_eff_B_2 = - B_X * (m_A(:,i) + k1_m_A) + 2 ...
                * [B_1,0,B_2]'.*(m_B(:,i) + k1_m_B) + B_ext;

            k2_m_A = gamma * cross(m_A(:,i) + k1_m_A,B_eff_A_2)* ...
                dt + lambda * gamma * cross(m_A(:,i) ...
                + k1_m_A,cross(m_A(:,i) + k1_m_A,B_eff_A_2)) * dt;
            k2_m_B = gamma * cross(m_B(:,i) + k1_m_B,B_eff_B_2)* ...
                dt + lambda * gamma * cross(m_B(:,i) ...
                + k1_m_B,cross(m_B(:,i) + k1_m_A,B_eff_B_2)) * dt;

            m_A(:,i+1) = m_A(:,i) + 1/2*k1_m_A + 1/2*k2_m_A;
            m_B(:,i+1) = m_B(:,i) + 1/2*k1_m_B + 1/2*k2_m_B;

        end;

        k = j*100;
```

```
        B_eff_A = - B_X * m_B(:,k) + 2 * [B_1,0,B_2]'.* m_A(:,k) + B_ext;
        B_eff_B = - B_X * m_A(:,k) + 2 * [B_1,0,B_2]'.* m_B(:,k) + B_ext;

        k1_m_A = gamma * cross(m_A(:,k),B_eff_A)* dt + lambda * gamma ...
            * cross(m_A(:,k),cross(m_A(:,k),B_eff_A))* dt;
        k1_m_B = gamma * cross(m_B(:,k),B_eff_B)* dt + lambda * gamma ...
            * cross(m_B(:,k),cross(m_B(:,k),B_eff_B))* dt;

        B_eff_A_2 = - B_X * (m_B(:,k) + k1_m_B) + 2 ...
            * [B_1,0,B_2]'.*(m_A(:,k) + k1_m_A) + B_ext;
        B_eff_B_2 = - B_X * (m_A(:,k) + k1_m_A) + 2 ...
            * [B_1,0,B_2]'.*(m_B(:,k) + k1_m_B) + B_ext;

        k2_m_A = gamma * cross(m_A(:,k) + k1_m_A,B_eff_A_2)* dt ...
            + lambda * gamma * cross(m_A(:,k) + k1_m_A,cross(m_A(:,k) ...
            + k1_m_A,B_eff_A_2)) * dt;
        k2_m_B = gamma * cross(m_B(:,k) + k1_m_B,B_eff_B_2)* dt ...
            + lambda * gamma * cross(m_B(:,k) + k1_m_B,cross(m_B(:,k) ...
            + k1_m_A,B_eff_B_2)) * dt;

        b_fl_A = [normrnd(0,sigma_A*10),normrnd(0,sigma_A*10) ...
            ,normrnd(0,sigma_A*10)]';
        b_fl_B = [normrnd(0,sigma_B*10),normrnd(0,sigma_B*10) ...
            ,normrnd(0,sigma_B*10)]';

        m_A(:,k+1) = m_A(:,k) + 1/2*k1_m_A + 1/2*k2_m_A ...
            + gamma * cross(m_A(:,k),b_fl_A);
        m_B(:,k+1) = m_B(:,k) + 1/2*k1_m_B + 1/2*k2_m_B ...
            + gamma * cross(m_B(:,k),b_fl_B);

        % renormalize m_vectors

        m_A(:,k+1) = m_A(:,k+1)/sqrt(dot(m_A(:,k+1),m_A(:,k+1)));
        m_B(:,k+1) = m_B(:,k+1)/sqrt(dot(m_B(:,k+1),m_B(:,k+1)));
    end;

end

end
```

B.3 fft analysis

analysis.m and analysis_corr.m creates power spectra and saves these to data files

```
g = 2.002;
mu_B = 9.274e-24;
k_B = 1.38065e-23;
S = sqrt((5/2)*(5/2+1));
kappa2_unit = 15e-4*k_B;
B_2_unit = 1 * (kappa2_unit*S)/(g*mu_B);
```

sim files:

```
load_boolean = 1;               % analyze the data in memory if set to 0
dirname = ['/scratch/garde/MATLAB_scans/'];       % looking for data
% files in this directory

%dirname = ['/home/garde/MATLAB_scans/' d '/' scanID];
% looking for data files in this directory (alternative)

scanStrOld = '012808-03';       % specify scan ID string (date + number)
scanNB = 3;

scanType = 1;                   % scanType: 1 - T, 2 - lambda, 3 - kappa2,
% 4 - "other" (dont use)

T_array = (20:20:100);          % scan range in K,
% (startpoint:stepsize:endpoint). Must be contained in folder dirname

lambda_array = (6:2:6)*1e-4;
B2_array = (1:0.2:1)*B_2_unit;

parts_array = (1:1:6);          % if each sim consists of fragments,
% fft each and sum. set = 0 if no frac index in filename
```

fft output specs:

```
save_boolean = 1;               % create fft data file
% (suitable for fitting)

FFT_res = 8;                    % set FFT_res to some power of 2 for
% higher resolution
```

```
power_range = 5;                % +- meV range of data to be considered
E_res = 0.01;                   % energy resolution in fitting datafile

% convolution (instrument resolution function, or minimal smoothing if
% conv_sigma = 0.006):

conv_sigma = 0.051;             % std. dev. of the instrument
% resolution function (a normalized gaussian).
conv_boolean = 0;           if conv_boolean == 0, conv_sigma = 0.006; end;
% if conv_sigma = 0, this value performs minimal required smoothing

% smoothing (a tiny bit of naiive smoothing appears nesseccary)

smooth_boolean = 1;             % I dont think we need this - rather not.
smooth_range_E = 0.0001;        % energy range to be smoothed around.
% To get rid of the fft artifact (high freq spectrum oscillations)
smooth_times = 1;
```

plotting specs (outdated)

```
plot_boolean = 0;               % plot if == 1
plot_fitdata_boolean = 0;
fignum = 0;                     % what figure to plot to.
% Create a new fig if fignum == 0
E_min = -1;
E_max = 3;
plotrange_2D = [E_min E_max 8 24];     % plot axis.
% [x_min x_max y_min y_max]. x = energy, y = T.
plotrange_3D = [E_min E_max 0 500];    % plot axis.
% [x_min x_max y_min y_max]. x = energy, y = T, z = I is automatic.

%%%%%%%%%%%%%%%%%%%%%%%%%%%%%
```

fft and analysis section %%

```
%%%%%%%%%%%%%%%%%%%%%%%%%%%%%

k_B = 1.38065e-23;
hbar = 1.05459e-34;
meV = 1.602e-22;
g = 2.002;
mu_B = 9.274e-24;
gamma = - g*mu_B/hbar;
```

```
switch scanType
    case 1, runValue_array = T_array;
    case 2, runValue_array = lambda_array;
    case 3, runValue_array = B2_array;
    otherwise, runValue_array = 0;
end

scanSize = size(runValue_array);
scanSize = scanSize(1,2);

for i = 1:scanSize;

    X_acc = 0;
    Y_acc = 0;
    Z_acc = 0;
    YZ_centered = 0;
    partTot = size(parts_array);
    partTot = partTot(1,2);

    for partNB = 1: partTot         % sum fft of each of the partNB runs

        % load trajectory data:

        if load_boolean == 1
            [filename scanStr runStr partStr] = makeRunFileName(scanNB, ...
                scanType,runValue_array(i),partNB);
            filename = [scanStrOld '_' runStr '_' partStr];
            load([dirname scanStrOld '/' filename]);
        end

        % create fft

        NFFT = 2^nextpow2(N)*FFT_res;          % FFT precision
        f = 2*pi/dt;                           % Sampling frequency [Hz]
        freq = f*(1:NFFT/2)/NFFT;              % frequency vector
        dE = f*hbar/meV/NFFT;
        E_vector = freq*hbar/meV;

        X = abs(fft(m_A(1,:),NFFT)).^2;
% analysis_corr uses X = abs(fft(m_A(1,:).*theta,NFFT)).^2;
        Y = abs(fft(m_A(2,:),NFFT)).^2;
        Z = abs(fft(m_A(3,:),NFFT)).^2;
```

```
        % rearrange power spectrum for easy comparrison with data,
        % i.e. E = 0 in the middle. Include only from -power_range to
        % power_range [meV]. Create energy scale vector.

        P_i = round(power_range/(f*hbar/meV/NFFT));
        % index corresponding to power_range meV

        clear temp;
        temp(1:P_i) = X(NFFT+1-P_i:NFFT);
        X_centered = [temp(1:P_i),X(1),X(1:P_i)];
        temp(1:P_i) = Y(NFFT+1-P_i:NFFT);
        Y_centered = [temp(1:P_i),Y(1),Y(1:P_i)];
        temp(1:P_i) = Z(NFFT+1-P_i:NFFT);
        Z_centered = [temp(1:P_i),Z(1),Z(1:P_i)];
        temp(1:P_i) = -fliplr(E_vector(1:P_i));
        E_vector_centered = [temp,0,E_vector(1:P_i)];


        % add power spectra of individual parts. These are additive just as
        % weighed average of scattering data. Each part represents an equal
        % amount of simulation time, therefore hold equal amounts of
        % information, thus no weights are nesseccary

        X_acc = X_acc + X_centered;
        Y_acc = Y_acc + Y_centered;
        Z_acc = Z_acc + Z_centered;
        YZ_centered = YZ_centered + Y_centered + Z_centered;

    end

    % save this raw fft result of the combined parts. This will be handy
    if save_boolean == 1;
        [filename, scanStr, runStr, fftStr] = makeFFTFileName(scanNB, ...
            scanType,runValue_array(i),1,conv_sigma);
        saveStr = [dirname scanStrOld '/' scanStrOld '_' ...
            runStr '_' fftStr '.mat'];
        save(saveStr,'E_vector_centered','X_acc','Y_acc','Z_acc', ...
            'YZ_centered','FFT_res','NFFT');
        % save raw fft data, for future use
        clear saveStr
    end

%%%%%%%%%%%%%%%%%%%%%%%%%%%%%%%%%%%%%%%%%%%%%%%%
```

data minipulation. smooth, convolution %%

```
%%%%%%%%%%%%%%%%%%%%%%%%%%%%%%%%%%%%%%%%%%%%%%%%

if smooth_boolean == 1
    smooth_range = ceil(smooth_range_E/(f*hbar/meV/NFFT));
    for k = 1:smooth_times
        YZ_centered = smooth(YZ_centered,smooth_range);
% effectively 1 point of smoothing
        %    Y_centered = smooth(Y_centered,smooth_range);
        %    Z_centered = smooth(Z_centered,smooth_range);
    end
end


    E_min_index = round((5+E_min)/(f*hbar/meV/NFFT));
    E_max_index = round((5+E_max)/(f*hbar/meV/NFFT));
    runValue_vector = runValue_array(i)*ones(1, ...
        2*round(5/(f*hbar/meV/NFFT))+1);


    if conv_sigma ~= 0
        gauss_range = 2*round((3*conv_sigma)/(f*hbar/meV/NFFT));
        res = gaussmf(E_vector_centered(round((power_range-3*conv_sigma) ...
            /(f*hbar/meV/NFFT)):round((power_range+3*conv_sigma) ...
            /(f*hbar/meV/NFFT))), [conv_sigma 0]);
        resolution = res/sum(res);
        temp = conv(YZ_centered,resolution);
        YZ_centered = temp(gauss_range/2:size(temp) - gauss_range/2-2);
    end


%%%%%%%%%%%%%%%%%%%%%%
```

save fft data %%

```
%%%%%%%%%%%%%%%%%%%%%%


if save_boolean == 1;
% create the data subset to be used for fitting
        E_res_index = round(E_res/(f*hbar/meV/NFFT));
        L = size(YZ_centered);
        L = L(1,1);
```

```
        subset_displacement = mod(floor((L-gauss_range*2)/2),E_res_index);
        range_adjustment = gauss_range;
        data_points = floor((L-gauss_range*2)/E_res_index);
        data_array = [E_vector_centered(1,subset_displacement ...
            +range_adjustment:E_res_index:data_points*E_res_index ...
            +range_adjustment)',...
            YZ_centered(subset_displacement ...
            +range_adjustment:E_res_index:data_points*E_res_index ...
            +range_adjustment),ones(data_points,1)];

% create appropriate filenames and save
        [filename, scanStr, runStr, fftStr] = makeFFTFileName(scanNB, ...
            scanType,runValue_array(i),2,conv_sigma);
        saveStr = [dirname scanStrOld '/' scanStrOld '_' ...
            runStr '_' fftStr '.dat'];
        save(saveStr,'data_array','-ASCII'); % save fitting data
        display(['saved data to file ' saveStr]);
% plot the resulting points
        if plot_fitdata_boolean == 1
            figure
            plot(data_array(:,1),log(data_array(:,2)),'LineWidth', ...
                1,'Linestyle','none',...
                'MarkerSize',3,'Marker','x')
            title(['_T' num2str(runValue_array(i))]);
        end
end

%%%%%%%%%%%%%%%%%%%%%%%
```

add to the figure %%

```
%%%%%%%%%%%%%%%%%%%%%%%


    % log plot:

    YZ_centered = log(YZ_centered);

    % plot:


    if plot_boolean == 1;
        if i == 1, if fignum, figure(fignum), else figure, end, end
```

```
        if scanSize == 1
            plot(E_vector_centered(E_min_index:E_max_index), ...
                YZ_centered(E_min_index:E_max_index))

            axis(plotrange_2D)
            title([dirname ', iterations: ' num2str(N*sim_copies) ...
                ', T = ' num2str(T) ', lambda = ' num2str(lambda)])
            xlabel('energy [meV]')
            ylabel('log(Y + Z)')

            hold on
        else
            % plot3(E_vector_centered(NFFT/2-0.5*E_range:NFFT ...
            % /2+1.5*E_range),runValue_array,YZ_centered(NFFT ...
            % /2-0.5*E_range:NFFT/2+1.5*E_range))
            plot3(E_vector_centered(E_min_index:E_max_index), ...
                runValue_vector(E_min_index:E_max_index), ...
                YZ_centered(E_min_index:E_max_index))

            axis(plotrange_3D)
            title([dirname ', lambda = ' num2str(lambda)])
            xlabel('energy [meV]')
            ylabel('T [K]')
            zlabel('log(Y + Z)')
            hold on
        end
    end

end

  ]
```

Appendix C

Additional time evolution plots

Additional time evolution figures are found in this appendix.

I have included 6 ns of continous time evolution at 40, 150 and 300 K. Notice how the dynamics changes with temperature. At low temperatures it is the image of a classical superparamagnet and as discussed in chapter 5 and 6 this changes at higher temperatures. Notice how precessions in the y-z plane are consistently coupled with an angling θ of about half a degree.

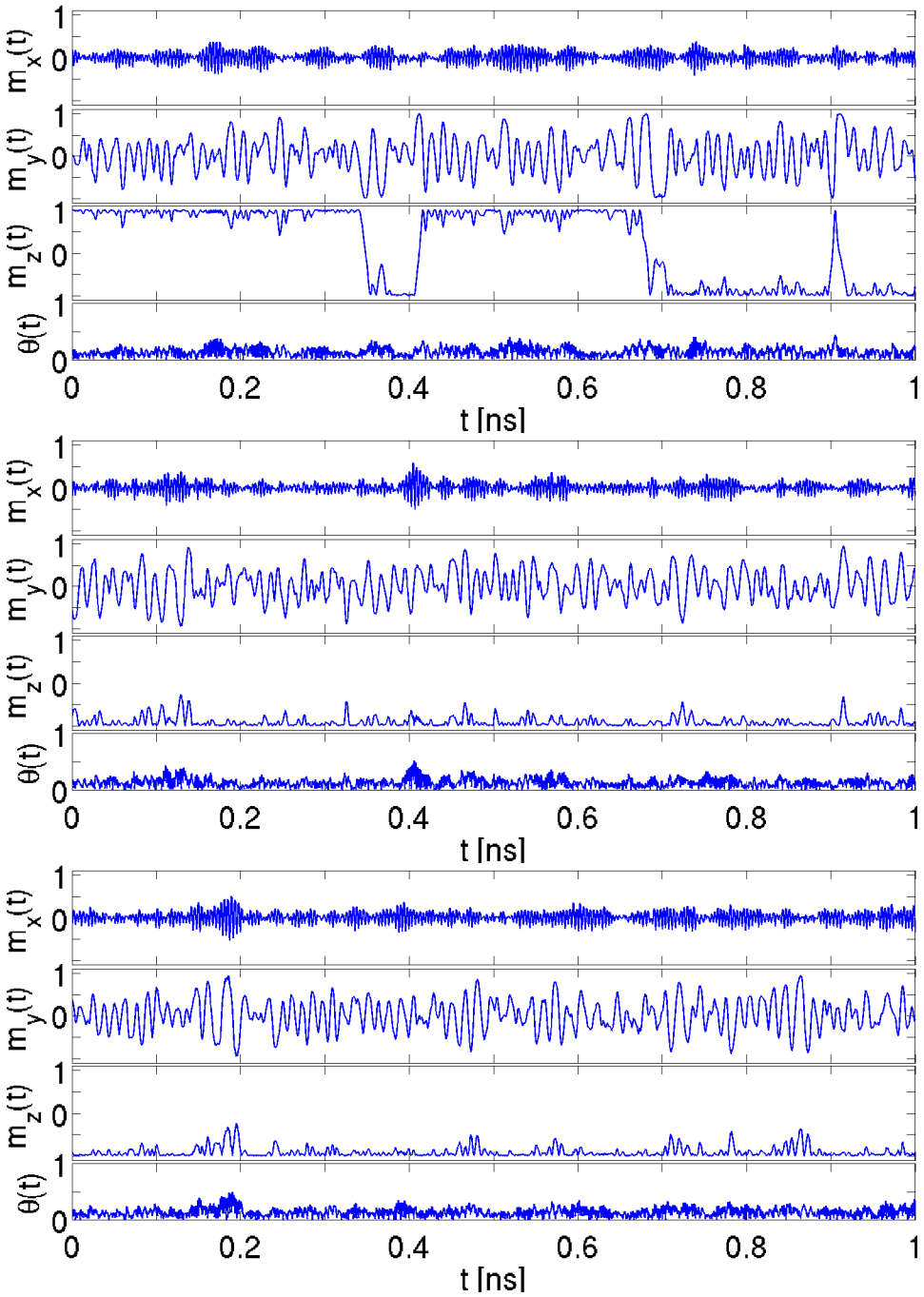

Figure C.1: *Continued time evolution of* $\mathbf{m}^A$ *through 3 ns at* 150 *K.*

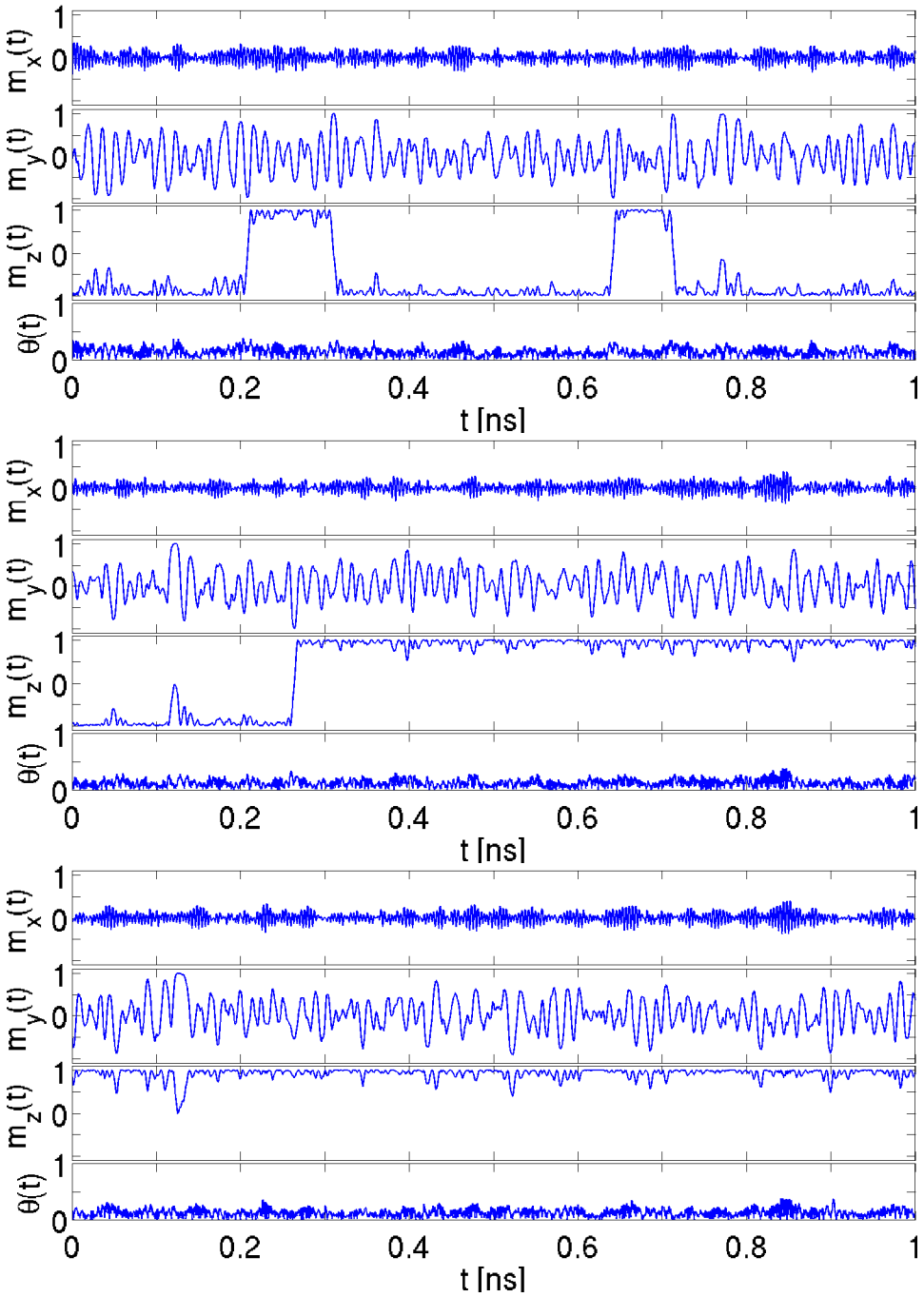

Figure C.2: *Continuation of Fig. C.1.*

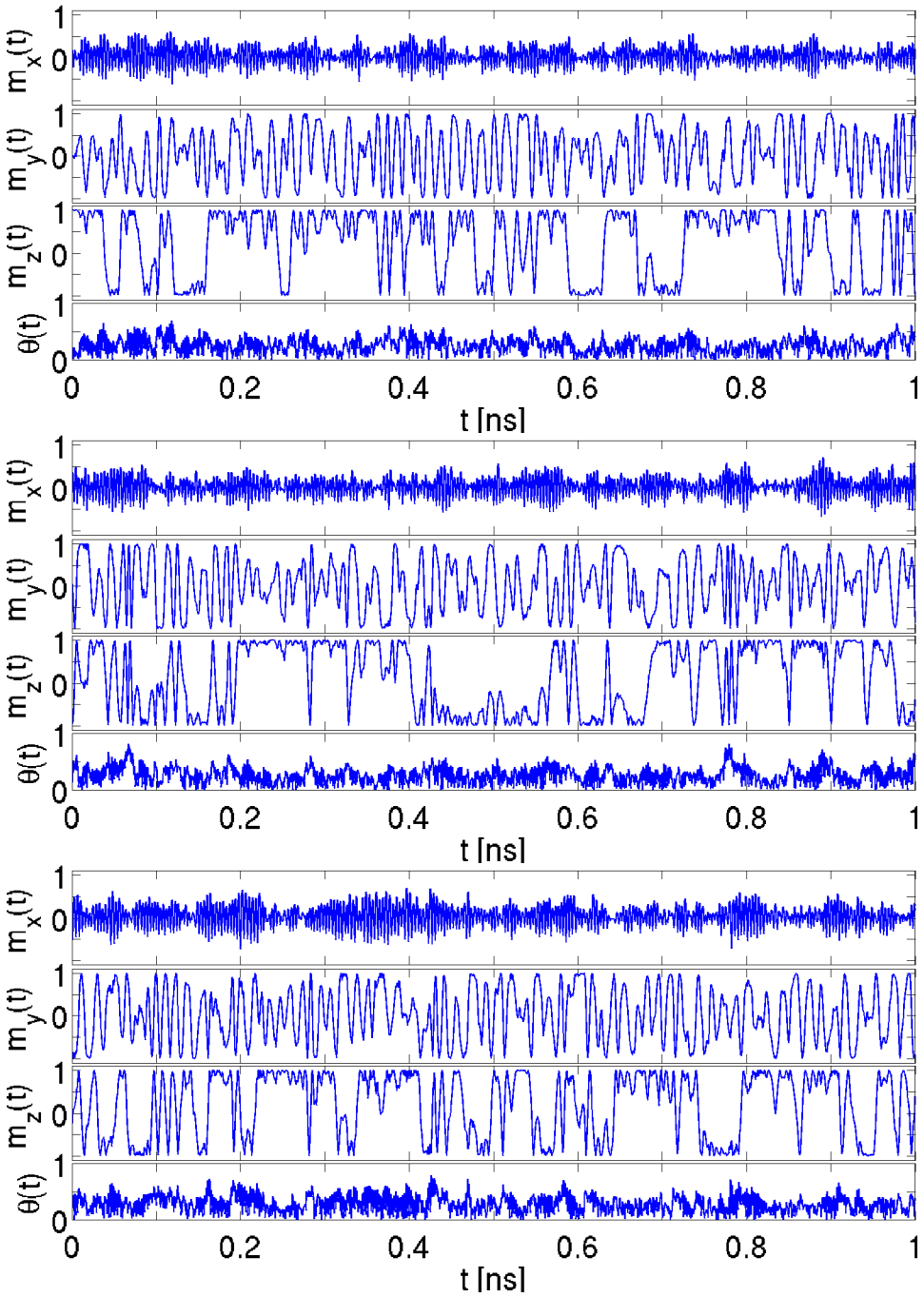

Figure C.3: *Continued time evolution of* $\mathbf{m}^A$ *through 3 ns at* 150 *K.*

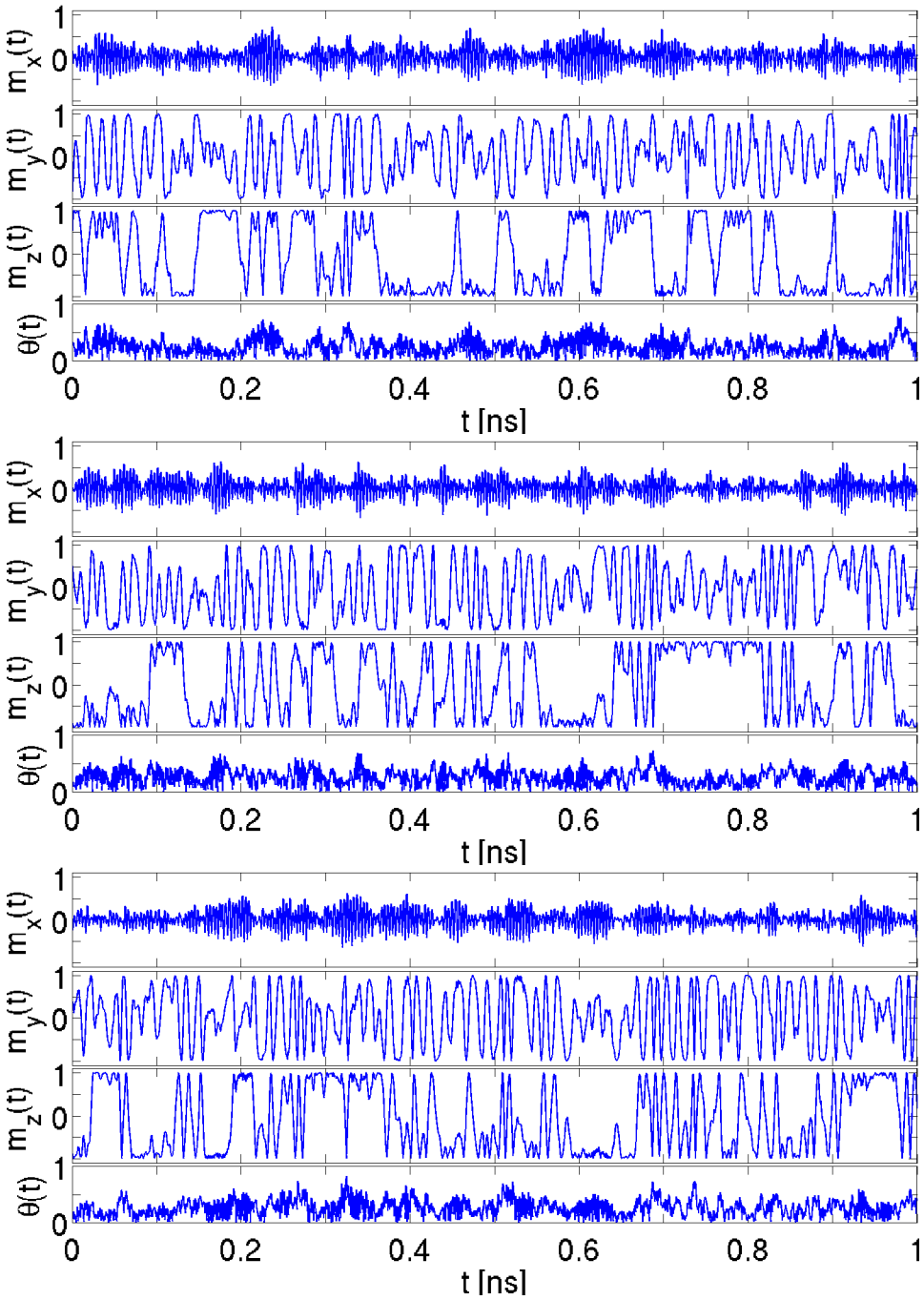

Figure C.4: *Continuation of Fig. C.3.*

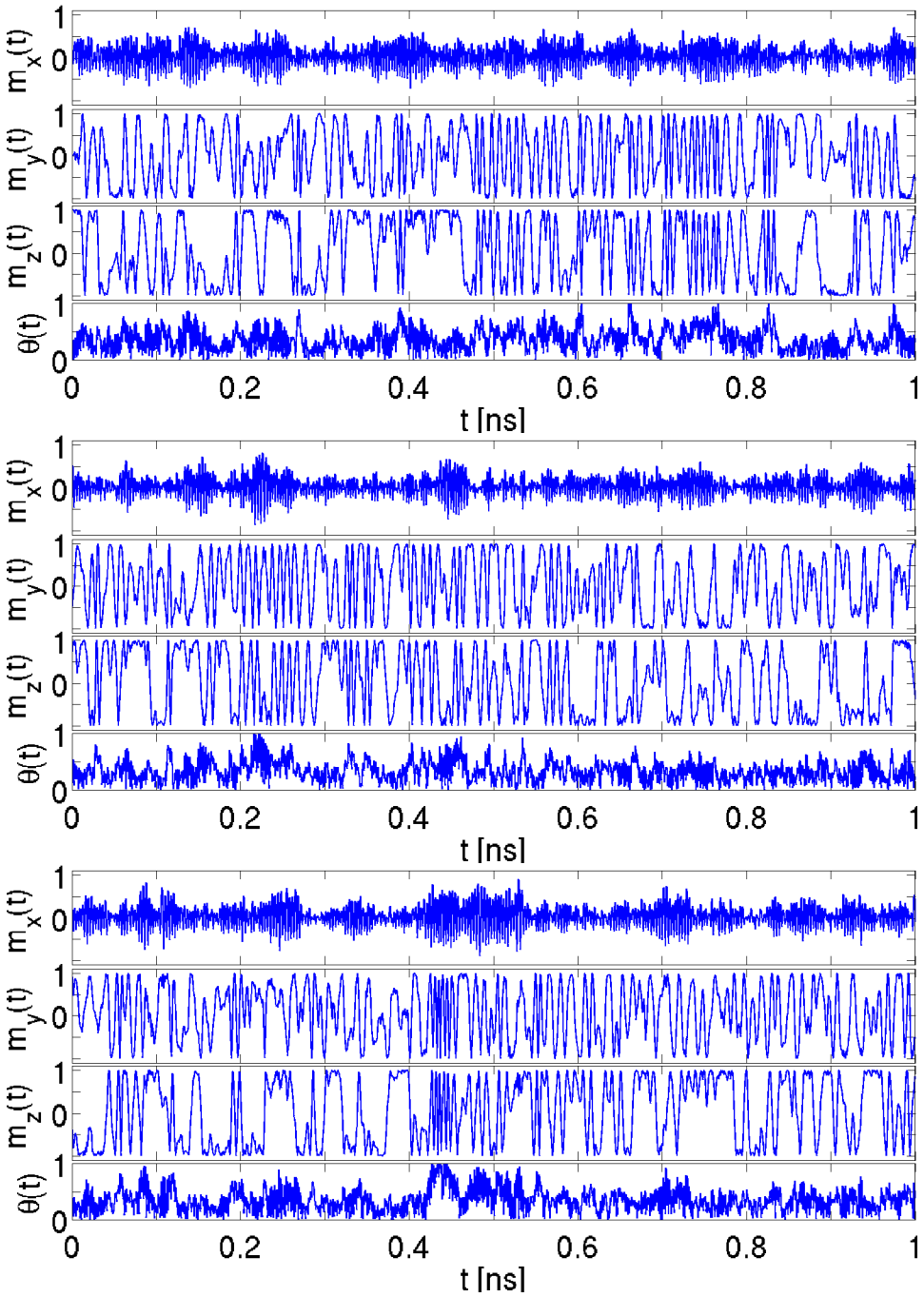

Figure C.5: *Continued time evolution of* $\mathbf{m}^A$ *through 3 ns at* 300 *K.*

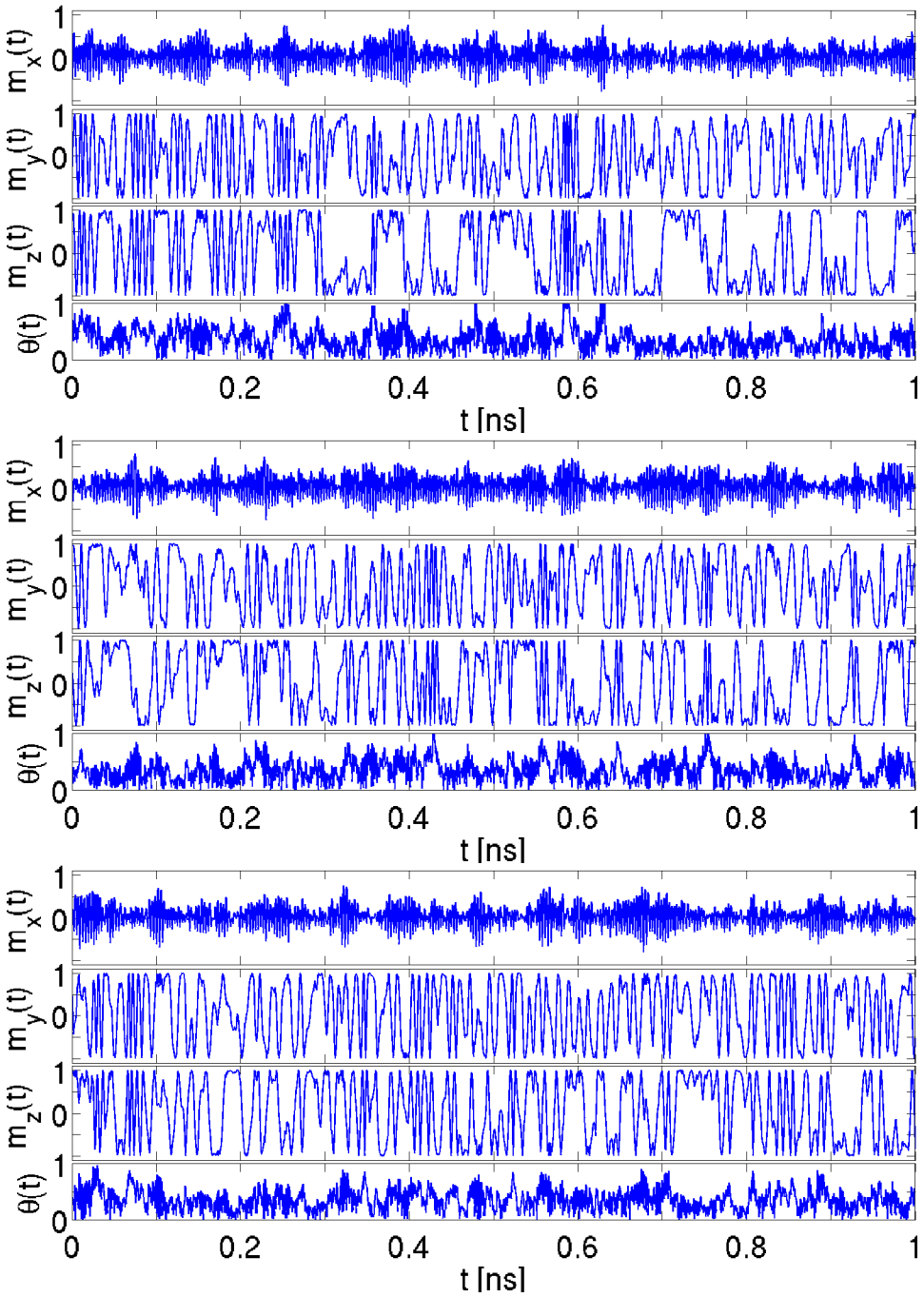

Figure C.6: *Continuation of Fig. C.5.*

Appendix D

Spinwave paper

This paper contains detailed calculations of the spinwave energies of a magnetic nanoparticle with planar and axial anisotropies, in the presence of uncompensated moments.

I have written section 2.0 and gone through all calculations and plots in detail.

Bibliography

[1] A. H. Morrish, *Canted Antiferromagnetism: Hematite* (World Scientific, 1994).

[2] C. Kittel, *Introduction to Solid State Physics* (Wiley, 2005).

[3] S. Blundell, *Magnetism in Condensed Matter* (Oxford Master Series in Condensed Matter Physics, 2001).

[4] K. Yosida, *Theory of Magnetism* (Springer series in Solid-State Sciences 122, 1991).

[5] F. Bodker, M. F. Hansen, C. B. Koch, K. Lefmann, and S. Morup, Physical Review B **61**, 6826 (2000).

[6] K. Lefmann, F. Bodker, M. F. Hansen, H. Vazquez, N. B. Christensen, P. A. Lindgard, K. N. Clausen, and S. Morup, European Physical Journal D **9**, 491 (1999).

[7] M. F. Hansen, F. Bodker, S. Morup, K. Lefmann, K. N. Clausen, and P. A. Lindgard, Physical Review Letters **79**, 4910 (1997).

[8] P. J. Besser, A. H. Morrish, and C. W. Searkt, Physical Review **153**, 632 (1967).

[9] S. N. Klausen *et al.*, Physical Review B **70**, 214411 (2004).

[10] L. T. Kuhn, K. Lefmann, C. R. H. Bahl, S. N. Ancona, P. A. Lindgård, C. Frandsen, D. E. Madsen, and S. Mórup, Physical Review B **74**, 184406 (2006).

[11] F. Bodker and S. Morup, Europhysics Letters **52**, 217 (2000).

[12] M. Z. Dang, D. G. Rancourt, J. E. Dutrizac, G. Lamarche, and R. Provencher, Hyperfine Interactions **117**, 271 (1998).

[13] C. R. H. Bahl, J. Garde, K. Lefmann, T. B. S. Jensen, P.-A. Lindgård, D. E. Madsen, and S. Mørup, accepted to the European Physical Journal B (2008).

[14] P. V. Hendriksen, S. Linderoth, and P. A. Lindgård, Journal Of Physics-Condensed Matter **5**, 5675 (1993).

[15] Samuelsen and Shirane, Physica Status Solidi **42**, 241 (1970).

[16] S. Mørup and H. Topsøe, Appl. Phys. **11**, 63 (1976).

[17] C. Kittel, Physical Review **82**, 565 (1951).

[18] L. Néel, Comptes Rendus Hebdomadaires Des Seances De L Academie Des Sciences **228**, 664 (1949).

[19] W. F. Brown, Physical Review **1**, 1677 (1963).

[20] W. Wernsdorfer, E. B. Orozco, K. Hasselbach, A. Benoit, B. Barbara, N. Demoncy, A. Loiseau, H. Pascard, and D. Mailly, Physical Review Letters **78**, 1791 (1997).

[21] J. D. Lee, Physical Review B **70**, 174450 (2004).

[22] G. L. Squires, *Introduction to the Theory of Thermal Neutron Scattering* (Dover, 1996).

[23] spectroscopy.web.psi.ch/rita2/.

[24] www.fz-juelich.de/iff/wns_bss.

[25] A. Wurger, Europhysics Letters **44**, 103 (1998).

[26] M. F. Hansen, C. B. Koch, and S. Morup, Physical Review B **62**, 1124 (2000).

[27] J. L. Garcia-Palacios and F. J. Lazaro, Physical Review B **58**, 14937 (1998).

[28] D. H. Martin, *Magnetism in solids* (M.I.T. Press, 1967).

[29] R. J. Elliott, J. Krumhans, and P. L. Leath, Reviews Of Modern Physics **46**, 465 (1974).

[30] R. M. Mazo, *Brownian Motion* (Oxford Science Publications, 2002).

[31] A. Einstein, Annalen Der Physik **17**, 549 (1905).

[32] H. Goldstein, *Classical Mechanics* (Addison Wesley, 2002).